Determination of Stellar Spin Orientation

Spectro-astrometry with DeSSpOt

Dissertation

zur Erlangung des Doktorgrades

des Department Physik
der Universität Hamburg

vorgelegt von

Anna-Lea Lesage
aus Kempten

Hamburg

2012

Gutachter der Dissertation :   Prof. Günter Wiedemann
                                                Dr. Eike Günther

Gutachter der Disputation :   Prof. Robi Banerjee
                                                Prof. Artie Hatzes

Datum der Disputation   10.12.2012

Vorsitzender des Prüfungsausschusses   Robert Baade

Vorsitzender des Promotionsauschusses   Prof. Peter Hauschildt

Dekan der Physik Falkult"at   Prof. Heinrich Graener

Abstract

I present a new technique, and its dedicated instrumentation named DeSSpOt (Differential imagE rotator for Stellar SPin OrienTation), for the determination of the orientation of the stellar rotation axis for late type stars. The method was successfully applied on the Capella system and on Aldebaran.

The technique relies on the acquisition of high resolution long slit spectra with a single telescope. It is dedicated for the observation of slow rotating giants with deep absorption lines.

I developed a two dimensional Doppler rotation model to describe the spatial effects of stellar rotation. On a high resolution long slit spectrum, the stellar rotation causes a tilt in the stellar lines in the spatial direction, whose inclination is dependent of $\sin \psi$, where ψ is the angle formed between the stellar spin and the spatial slit axis. The signature of the line tilt is retrieved using a spectro-astrometric reduction of the spectrum, a reduction technique which consists to track the wavelength dependency of the photocenter of the spectral order. The absolute position angle is recovered by monitoring the variations of the signal's amplitude with ψ. This requires to observe the star under an even number of slit orientations. Anti-parallel orientations are then subtracted from each other to remove instrumental effects.

Due to the very small scales involved here — the line tilt is expected to cause a shift of the photocentre of a few percent of a pixel — the atmospheric perturbations are a source of deterioration of the signal. These compromise the direct comparison of the anti-parallel orientation spectra. Therefore, I designed and constructed an instrument, the Differential imagE rotator for Stellar SPin OrienTation, in short DeSSpOt , to enable the simultaneous observation of two anti-parallel orientations of the star.

DeSSpOt was designed as a small and compact instrument to be inserted on existing high resolution long slit spectrographs. The image rotation in the instrument relies on two Dove prisms, which are rotated along the optical axis by $90°$ to each other. These prisms rotate the image by twice their own rotation angle. DeSSpOt projects two images of the star on the slit.

With the purpose of testing the functionality of the instrument in real observing conditions, and of validating the method as a whole, I observed Capella and Aldebaran with the high resolution Coudé spectrograph of the Thüringer Landessternwarte Tautenburg. Capella was chosen as verification target for the method due to its binarity. The signal from a binary system is not only similar to that of a single star, it has also an higher amplitude which makes it easier to detect during the verification phase. Aldebaran is one of the very few giants whose position angle is already known. Using the natural field rotation of the Coudé output, the targets were observed under 4 different orientations. The signal of each target was extracted using a cross-correlation analysis. I compared the signal generated only by the telluric lines to the signal from the stellar lines, and could distinguish clear orientation dependent trends. After correcting the stellar cross-correlation profiles from the telluric profiles, I retrieved an orbital position angle for Capella of $50.31° \pm 1.75°$, which is about $10°$ bigger than the reference value. An extensive search for systematic errors showed that the analysis method tend to overestimate the observed position angle by around $4.8° \pm 2.3°$. The same cross-correlation analysis was also performed on the spectra from Aldebaran. The retrieved position angle is of $114.8° \pm 3.4°$, compared to the reference value of $110° \pm 5°$. The results prove that the method is applicable for both binary systems and single giant stars.

Zusammenfassung

Eine neue Methode zur Bestimmung der Orientierung von Sternachsen für Riesensterne wird hier vorgestellt. Die Methode, und das dazu gehörige Instrument, Namens DeSSpOt, wurden erfolgreich auf das Capella-System und auf Aldebaran angewandt.

Die entwickelte Methode basiert auf die Analyse von hochauflösende Spektren, von einem Teleskop mit Spalt-spektrographen aufgenommen, von langsam rotierender Riesensterne mit tieffen Absorptionslinien.

Ich habe ein zweidimensionales Modell der Doppler Rotationsfunktion entwickelt, um die räumlichen Effekte der Sternrotation zu berücksichtigen. Die Sternrotation führt entlang der räumlichen Richtung einer, mit Spalt, Spektrenaufnahme zu einer Verkippung der Linien, deren Stärke von $\sin \psi$ abhängig ist. Hierbei bezeichnet ψ den Winkel zwischen der Rotationsachse des Sterns und der Spaltachse des Spektrographen. Die Signatur der Linienverkippung wird durch Spektroastrometische Reduktion der Spektren gemessen und entspricht einer Verschiebung des photometrischen Zentrums um die Linie herum. Der absolute Positionswinkel des Sterns wird dann durch die Überwachung der Abhängigkeit der Amplitude des Signals von $\sin \psi$ bestimmt. Dafür muss der Stern unter mehreren Spaltorientierungen beobachtet werden. Antiparallele Orientierungen werden danach voneinander abgezogen.

Wegen der kleinen Skalen dieses Signals, die sich im Bereich weniger Prozente eines Pixel bewegen, können atmosphärische Perturbationen das Signal unkenntlich machen. Dies verhindert einen direkten Vergleich der unter antiparallele Spaltorientierungen aufgenommenen Spektren. Deshalb habe ich den Differentiellen Bildrotator, DeSSpOt (Differential imagE rotator for Stellar SPin OrienTation) entwickelt, der die gleichzeitige Aufnahme von zwei antiparallelen Sternorientierungen ermöglicht.

DeSSpOt wurde als möglichst kompaktes Instrument konzipiert, um an existierenden hochauflösende Spalt Spektrographen einsetzbar zu sein. Die Bildrotation wird durch zwei Doveprismen erzeugt, die um $90°$ entlang der Optische Achse gegeneinander gedreht sind. DeSSpOt projiziert zwei Sternbilder auf den Spalt. DeSSpOt absolvierte am hochauflösenden Coudé-Spektrographen der Thüringer Landessternwarte Tautenburg eine Testkampagne, um die Funktionalität des Instruments unter realen Beobachtungsbedingungen zu testen und die Methode experimentell zu bestätigen.

Capella ist ein Doppelsternsystem, daß als Verifikationsobjekt gewählt wurde. Das Rotationssignal, das von einem Doppelsternsystem erzeugt wird, zeigt eine deutlich größere Amplitude und ist daher einfacher nachzuweisen. Aldebaran gehört zu den wenigen Sternen, deren Rotationsachsen bekannt sind. Die natürliche Feldrotation des Coudé-Ausgangs wurde ausgenutzt, um die Objekte unter vier verschiedenen Orientierungen zu beobachten. Das Signal wurde mit einer Crosscorrelationsanalyse extrahiert. Ich verglich das Signal, das von tellurischen Linien erzeugt wurde, mit dem Signal der Sternlinien und konnte verschiedene Orientierungsabhängige Trends festellen. Nach einer Seeingkorrektur der Crosscorrelationsprofile, konnte der Bahnpositionswinkel von Capella auf $50.31° \pm 1.75°$ bestimmt werden, was ca $10°$ größer ist als der Referenzwert. Eine intensive Suche nach systematischen Fehlern konnte zeigen, dass die Analysemethode den Positionswinkel um $4.8° \pm 2.3°$ überschätzt. Dieselbe Crosscorrelationsanalyse wurde auf Spektren von Aldebaran angewandt. Der Positionswinkel wurde auf $114.8° \pm 3.4°$ bestimmt bei einem Referenzwert von $110° \pm 5°$. Diese Ergebnisse zeigen, dass die Methode sowohl auf Doppelsternsysteme als auch auf Riesensterne anwendbar ist.

Résumé

Ce travail présente une nouvelle méthode d'observation pour la détermination de l'orientation de l'axe de rotation d'étoiles géantes de type G à M. La méthode, et l'instrument DeSSpOt qui lui est dédiée, ont été utilisés avec succès sur le système Capella et sur Aldébaran.

La méthode repose l'acquisition en fente étroite de spectres à haute résolution par un unique télescope. Elle est dédiée en particulier à l'observation de géantes en rotation lente et aux raies peu elargies.

J'ai développé un modèle à deux dimensions de la fonction d'élargissement Doppler des raies d'absorption afin de prendre en compte les effets de la rotation stellaire. En effet, sur un spectre à haute résolution, cette dernière cause un basculement des raies stellaires spatialement, dont l'inclinaison dépend de $\sin \psi$ où ψ est l'angle défini entre l'axe de rotation de l'étoile et l'axe aligné spatialement avec la fente du spectrographe. La signature du basculement de la raie est obtenue via une réduction astrométrique des spectres, méthode qui consiste à suivre la position du photocentre de l'ordre spectral en fonction de la longueur d'onde. L'angle de position absolu de l'étoile est déterminé à partir de l'évolution de l'amplitude du signal avec ψ. Pour cela il est nécessaire d'observer la source sous différentes orientations. En raison de la faible amplitude des signaux recherchés — le basculement de la raie génère un déplacement du photo-centre de quelques pourcents de pixel —, les perturbations atmosphériques sont une importante source de détérioration du signal. C'est pourquoi j'ai conçu un instrument, DeSSpOt pour Differential imagE rotator for Stellar Spin OrienTation, afin d'observer simultanément l'étoile sous deux orientations anti-parallèles.

DeSSpOt est un instrument petit et compact, destiné à être facilement insérable sur des spectrographes existants. La rotation de l'image est faite avec deux prismes de Dove, tournés par rapport à l'axe optique à 90° et 180°. Ces prismes ont la particularité de tourner l'image par deux fois leur propre angle de rotation.

Dans le but de tester la fonctionnalité de l'instrument dans des conditions d'observations réelles, et afin de valider la méthode dans son ensemble, j'ai observé Capella et Aldébaran avec le spectrographe Coudé de l'observatoire de Tautenburg (Thüringer Landessternwarte Tautenburg). Capella a été choisi du fait de sa binarité : le signal généré par un système binaire, en plus d'être semblable à celui d'une étoile seule, est d'amplitude plus importante, ce qui le rend plus facilement détectable. Aldébaran est l'une des rares géantes dont l'angle de position a déjà été déterminé. Du fait du mode Coudé du spectrographe, la rotation naturelle du champ a permis d'observer les étoiles sous 4 orientations différentes. Le signal de chaque source a été extrait avec une analyse en corrélation croisée. J'ai comparé le signal issu uniquement des raies telluriques au signal des raies stellaires afin de mettre en évidence la contribution du seeing dans l'inclination des raies, et j'ai constaté des tendances nettes : en fonction de l'orientation, les signaux se recoupent — absence de signal stellaire — ou divergent clairement.

Après correction du signal atmosphérique, j'ai déterminé un angle de position orbital pour Capella de $50.31° \pm 1.75°$, qui est environ 10° au-dessus de la valeur de référence. Une étude poussée des sources d'erreurs systémiques a permis de montrer que la méthode d'analyse tend à surestimer l'angle de position observé de $4.8° \pm 2.3°$. La même analyse a été faite sur les spectres d'Aldébaran : l'angle de position mesuré est de $114.8° \pm 3.4°$, à comparer avec la valeur de référence qui est de $110° \pm 5°$. Ces résultats montrent que la méthode est applicable aussi bien sur des binaires que sur des étoiles géantes.

Contents

Chapter 1

Introduction

The basic stellar formation model states that the stellar system formed out of the original cloud conserves its spin axis, the spin axis of the central star being oriented perpendicularly to the orbit plane of the planets. However, observations of the spin-orbit alignment using the Rossiter-McLaughlin effect showed that the value of the angle between stellar spin axis and planetary orbit plane presents an random distribution [1]. In addition, recent simulations by Bate et al. (2010) showed that several factors could influence the formation process, in particular the inclination of the orbital plane [2]. Finally, observation on the binary system DI Herculi by Albrecht et al. (2009) found their spin axes strongly tilted to each other. Yet these measurements hold no information on the absolute orientation of the stellar axis.

The determination of the orientation of the stellar spin axis has been historically coupled with the advances in observation methods. In this work I present the development of a new observation method and dedicated instrumentation for the determination of stellar spin orientation. The method itself, spectro-astrometry, is described in the Chapter 2, while the theory and theoretical demonstration are developped in the Chapter 3. The instrument is examined in the Chapter 4. At last, the observational results are presented in the Chapter 5.

1.1   History

In the beginning of astronomy, men observed the sky with the naked eye. They noted the position of the stars and the changes in their brightness. In 2000 BC, the Egyptians were already familiar with the retrograde orbit of Mars. The ancient Greeks defined the term of planet (*planēton*) to describe the celestial bodies which moved with respect to the background stars. Their definition included Mars, Venus, Jupiter, Saturn, Mercury, the Moon and the Sun. Back then, the world was believed to be geocentric, and the Sun was imagined as a big fireball planet, a vision which lasted till the end of the 19th century. Except for the Moon, all the planets, in our modern definition, are too small to be resolved with the eye alone and were seen only as bright spots in the night sky. Hence, the Renaissance astronomers started to rely on the help of instruments to magnify the size of the observed objects. Galileo Galilei was the first to use a refracting telescope for his observations. In 1610, only two years after the construction of the first working telescope, he observed Jupiter and could distinguish four of its satellites. Later on he observed the phases of Venus, Saturn and its rings, whereas he didn't recognise them as such, and sunspots.

The first star whose rotation axis was determined is our Sun. With an apparent diameter of 30 arcmin ($0.5°$) in the sky, it was easily resolved with the early instruments of the 17th century. Galileo

---

1. R. Heller made a table referencing the angles and the publications of the systems which were tested. The resulting spin-orbit angle histogram has a slight peak around $0°$ but almost half of the angles diverges by more than $20°$ from this value. Up-to-date, only 56 systems have been measured. See the Holt-Rossiter-McLaughlin Encyclopaedia at www.aip.de/People/RHeller.

2. In the work of Bate, the spin-orbit misalignment is caused by a passing star, or a strong perturber.

was one of the first Europeans to observe sunspots. In 1612, during the summer months, he made a series of sunspot observations which were published shortly after in 1613. A few years later, in 1615, a pair of German astronomers, David Fabricius and his son, observed for several months the evolution of sollar spots to verify Kepler's theory about the Sun's rotation. They determined out of their observations a rotation period of about 27 days and 12 hours. Slightly later, the French-Italian astronomer Cassini repeated the experiment but also took into account the rotation of the Earth and derived a true rotation period for the Sun of 25 days and 14 hours, which is still quite accurate. In addition, he remarked that the Solar equator is inclined with respect to the Earth equator. Hence he made a first estimation of the orientation of the Sun's rotation axis.

Then, for over two centuries, the other stars remained out of reach, unresolved. The development of spectroscopy allowed the determination of many rotational velocities, showing that all stars do rotate (in case some astronomers still doubted it). But the stars remaining unresolved for imaging, it was impossible to follow up their spots. Hence astronomers were forced to devise alternative methods to determine the stellar spin axis.

This chapter introduces some fundamental notions in observation techniques, but also to follow the history of the determination of stellar spin orientations. The first section concentrates on direct imaging, therefore I introduce the notions of angular resolution and diffraction limit in order to explain the challenges set by stellar spin determination. The second section deals with interferometry. Since the first stellar orientation axis determined outside our Solar system were based on interferometric observation, I firstly describe the basic theory behind it. Then I present the current two methods, Differential Speckle Interferometry and Long Baseline Interferometry, which achieved this goal.

1.2   Angular Resolution

Observed with the naked eye, all stars look like point sources in the night sky. Therefore, one would expect that on images taken with telescope and detector, the stars are restricted to one pixel. However, they spread over several pixel on the detector. In the absence of atmosphere, and using the same pixel size, one would notice that the spreading decreases for increasing telescope size. This is the phenomenon of diffraction. The angular resolution of an optical system is its capability to separate different features on the target. Historically, it was introduced as the ability to separate two binary stars.

A fundamental lower limit to the angular resolution for an optical system can be derived from the Heisenberg's uncertainty relation [3] . But I'll concentrate on the origin of the Rayleigh criterion, since it's the most commomly used in astronomy. The shape of the spreading is defined by the diffraction equations. For astronomical instruments, where the light source is a distant star, we can apply the Fraunhofer diffraction relation. The primary mirror of the telescope acts as a round aperture, causing a specific diffraction pattern whose intensity distribution is given by:

$$I(x) = I_o \left| \frac{2J_1(x)}{x} \right|^2 \tag{1.1}$$

with $x = \pi D \sin \theta / \lambda$, I_o the peak irradiance and where J_1 is the first order Bessel function. The diffraction image resulting from an uniformly illuminated round aperture consists of a central bright region, known as the Airy disc, surrounded by fainter rings. The rings are separated by regions of zero intensity. The diameter of the Airy disc, defined at the first zero intensity ring, is $2.44\lambda/D$. The most famous criterion for defining the angular resolution of an optical system is derived from this relation. The Rayleigh criterion stipulates that two point sources are resolvable is their intensity maxima are separated by at least half of the diameter of their Airy disc as seen in Figure 1.1. This translates into

---

3. $\Delta\theta \geq \lambda/(4\pi D)$. The demonstration of this relation is done in the article of Whelan & Garcia (2008). It is not relevant here and was consequently not reproduced.
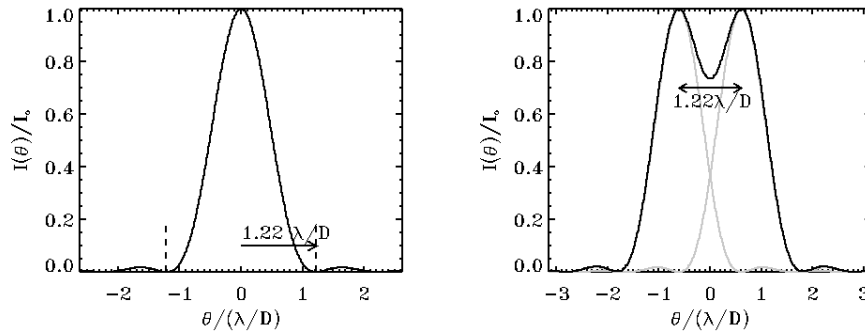
Figure 1.1: *Left:*A cut through the center of the Airy disk. The first extinction is reached for $\theta = 1.22\lambda/D$. *Right:* The Rayleigh resolution criterion.

the expression:

$$\Delta\theta = 1.22\frac{\lambda}{D} \tag{1.2}$$

Resolution criteria, like the Rayleigh or the Sparrow criterion[4], are not really limits but indicators of the systems resolving performances. For the VLT-telescopes (8.2 m diameter) the diffraction limited angular resolution, according to the Rayleigh criterion, would be of 16 milliarcseconds (mas) in the visible at 550 nm.

1.2.1 Seeing

However, ground-based telescopes almost never reach the diffraction limited resolution. Fluctuations in the refractive index of the Earth's atmosphere above the observing site lessen the angular resolution. This phenomenon is called *seeing*. The atmospheric fluctuations causing the seeing vary on a very short timescale known as the *atmospheric coherence time*. Depending on the observing site and the meteorological conditions, it ranges from 1 to $15ms$. In addition, stars captured with exposure times lower than the atmospheric coherence time present a Speckle pattern as illustrated in the Figure 1.2. Instead of concentrating on one bright spot, the light is spread over the detector with irregular intensity. Furthermore, images captured with integration times considerably longer than the atmospheric coherence time show a seeing disc much bigger than the Airy disc of a diffraction-limited image. This leads to a loss in accuracy for the determination of stellar position as in astrometry. Although there are multiple processes in the atmosphere influencing the seeing conditions, low humidity and high altitude tend to guarantee small seeing disc. For instance, the average seeing at the Paranal site (Chile) where the VLT telescopes are operated is around $0.8''$. On the contrary, the average seeing at Hamburg-Bergedorf is around $2.5''$.

1.2.2 Adaptive Optics

As the atmospheric seeing degrades dramatically the resolution performance of the telescope, additional instrumentation has been devised to restore the resolution at diffraction limit. Adaptive optic is one successful method to achieve this requirement. The advances in speed for wavefront sensing and in the deformable mirror have allowed a true boom in adaptive optic over the last two decades.

The basic principle of Adaptive Optic is simple: seeing causes the incoming wavefront to be distorted. If the wavefront could be corrected from these distortions, then one would obtain the stellar image as it was before passing through the atmosphere. The realization itself is done in three steps.

---

4. The Sparrow criterion set the resolution limit at $\delta \geq 0.95\frac{\lambda}{D}$, which corresponds to the value at which the bridge between the two sources disapears

(a) Vega integrated over 2 ms. The speckle pattern causes the star to be blurred over several pixels,

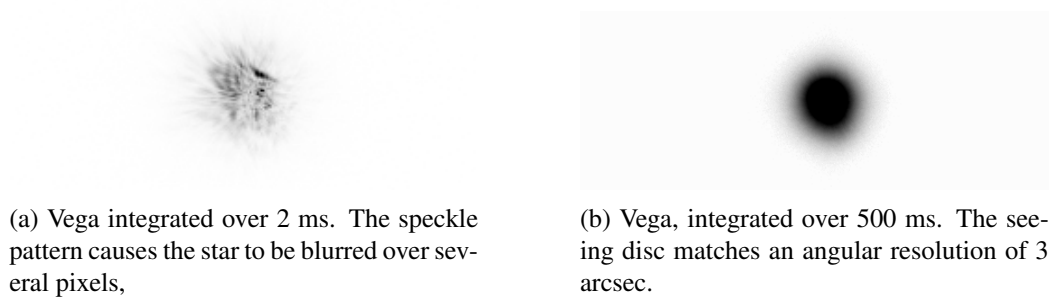(b) Vega, integrated over 500 ms. The seeing disc matches an angular resolution of 3 arcsec.

Figure 1.2: Two images of Vega, observed with the Oskar Lühning Telescope (1.2 m), to illustrate the influence of the atmosphere of the imaging quality. *Left:* The Speckle image of Vega. *Right:* The seeing limited image of Vega.
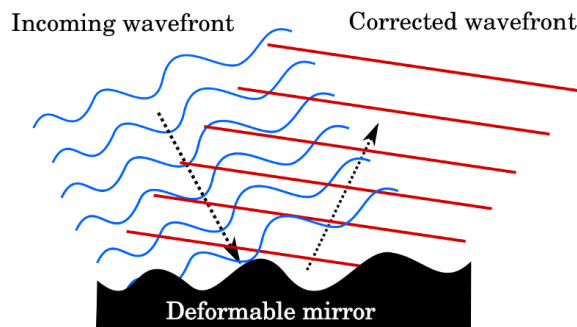

Figure 1.3: The incoming wavefront, deformed by the Earth's atmosphere is mirrored by the deformable mirror. After reflection, the wavefront is planar.

Firstly, after reflection on the primary mirror, a small fraction of the light is deviated towards a wavefront sensor. Then the measurements are analysed by an ultra fast computer, which reconstructs the shape of the incoming wavefront from the images obtained by the wavefront sensor. A negative of the wavefront is transmitted to the deformable mirror. As a result, after reflection the corrected wavefront is almost free of aberrations as illustrated in the Figure 1.3. The stellar light is reconcentrated back to one point, generating images close to the diffraction limit.

The Shack-Hartmann is one of the most common models of wavefront sensors used in astronomy. It consists of a CCD coupled with a lenslet array. Each lens focuses the rays on the CCD. Consequently the resulting image is an array of points, each marking the position of the focused rays through one lenslet. By monitoring the position variation of each point, it is possible to reconstruct the wavefront of the incoming stellar beam. If there is sufficient light, this detector measures the aberrations in the wavefront at a timescale close to the atmospheric coherence time.

The deformable mirror has a large number of actuators below the surface which enables an important deformation of the reflecting surface. Each actuator can move over a few micrometers at high frequency. The surface of the mirror is transformed correspondingly to the incoming wavefront.

However, adaptive optics are currently used mostly used in the infra-red, because of the region of interest and because it is easier to reach diffraction limited images at these wavelengths. In addition, the AO system requires a large amount of light during the very short exposures in order to enable a real-time correction. As a result it could firstly only be applied on very bright stars. However, the use of laser guide stars, fake stars resulting from the excitation of the Sodium layer of our atmosphere with a laser, have provided similarly good results and allows the observations of fainter stars.

Even with the aid of Adaptive Optic, the stars remain unresolved. Let us have a look an the order of magnitude reached so far. The average apparent diameter for our closest neighbours is around 5 to

10 milliarcseconds (hereafter noted mas). The apparent biggest star is Betelgeuse with an apparent diameters of $\sim$ 50 mas [5], closely folllowed by Antares ($\sim$ 40 mas), Arcturus and Aldebaran ($\sim$ 20 mas), Mirach ($\sim$ 14 mas) and Kochab ($\sim$ 13 mas). Those are all red giants or super red giants, stars in the late billion years of their life.

In order to resolve these stars with adaptive optics, one would still need a telescope with a mirror of at least 15 m diameter. Only the future extremely larges telescopes (E-ELT, TMT or GMT telescopes [6]) would satisfy this requirement. Astronomers have been aware of this issue for a long time, and determined to find alternative solutions. This lead to the development of interferometry.

1.3 Interferometry

Stellar interferometry was first suggested by Fizeau in 1868, but could only applied on observations by Michelson in 1924 with a single aperture. Observations with two apertures were successful starting in the seventies by Labeyrie. This illustrates that despite the theory being well understood its application and the development of appropriate instruments were challenging. In the following, I develop briefly the two main dimensions used in interferometry: visibility and phase.

1.3.1 Visibility and Phase

Interference occurs in two cases: when two, or more, different waves arrive at the same point, or when the waves from the same source take different paths. However in astronomy the latter is true in most cases, since the observation target is a star.

The interference pattern is an altenance of bright and dark stripes, equally separated. The *Visibility* defines the contrast between the fringes in terms of maximum and minimum fringe intensity:

$$|V| = \frac{I_{max} - I_{min}}{I_{max} + I_{min}} \tag{1.3}$$

In practice, the observation of fringes is depending on the spatial and temporal coherence of the source. It is communly assumed that the light beams are temporally coherent at least during the observation period. However there is a quantitative relationship between the spatial coherence and the structure of the source. Van Cittert (1934) and Zernike (1937) have defined the coherence function which holds the information on the angular structure of the stellar source as:

$$V = |V|exp(i\omega\Delta) \tag{1.4}$$

where Δ is the coherence or visibility phase. The visibility is related to the Fourier transform of the object brightness distribution, while the phase contains the spatial information, by storing the deviations from the centre-symmetry. Therefore the astrometric signal is located in the visibility phase Δ and not in the visibility amplitude $|V|$. Yet the value of Δ remains elusive due to phase fluctuations, and true imaging cannot be carried out.

1.3.2 Speckle Interferometry

The first application of interferometry in astronomy used the Speckle method. It relies on a single aperture telescope and therefore is limited to diffraction limit. In Speckle Interferometry, the target is observed a short exposure, in order to obtain Speckle patterns in the images. The interference is caused by the different cells in the atmospheres causing the Speckle pattern. These are analysed in

---

5. These measurements are selected from the Catalogue of stellar diameters (CADARS) from Lafrasse et al. (2010)

6. The E-ELT (European Extremely Large Telescope) is scheduled with a 39.5 m mirror, the TMT (Thirty meter telescope) and GMT (Giant Magellan Telescope), 24.5 m, are its North American equivalent. All projects have been approved and some are already in early construction phase

the Fourier domain with an auto-correlation function or a power spectrum in order to retrieve spatial information. For instance, it was applied in the seventies for the determination of binary orbits.

In the early eighties, Beckers (1982) suggested a method for the determination of stellar spin position angles by taking into account the Doppler shift caused by the star's rotation. A side of the star would be bluer and the opposite side redder. The idea was implemented in Differential Speckle Interferometry observations. This method combines the high spatial resolution of speckle interferometry with spectral resolution, i.e. the object is observed simultaneously at different wavelengths thanks to filters or a spectrograph. By monitoring the variations in the position of the photocenter of the speckle along with the wavelength, and for different stellar orientation, it is possible to retrieve the position angle of the stellar spin axis. The method was used successfully on Aldebaran by Lagarde et al. (1995), who found a value of $110° \pm 5°$ for the position angle.

The analysis is only limited by the photon and speckle noise. However the method itself is restricted for stars brighter than 3 - 4 apparent magnitude and with simple structures. Finally since it is a single aperture observation method, the best resolution attainable is given by the diffraction limit of the telescope. In the end, the method is no longer used for this application, but is still used for the study of the solar photosphere, or the determination of binary orbits.

1.3.3 Long Baseline Interferometry

In Long Baseline Interferometry, the light is collected by at least two telescopes. The path difference between the telescopes is $\Delta p = B \sin \theta$, where B is the distance between the two telescopes. Therefore, the corresponding angular resolution is:

$$\Delta \theta \sim \frac{\lambda}{B} \ \text{in rad} \tag{1.5}$$

Since the baseline between two telescope can span from a few meters to hundred meters, the angular resolutions reached here go down to the milli-arcsecond scale. The potential of Long Baseline Interferometry lies in its imaging capability. Indeed, it relies on aperture synthesis. Each telescope pair defines a baseline which corresponds to one point in the (u,v) plane in the Fourier frequency domain. Since the visibility $|V|$ describes the Fourier transform of the source brightness distribution, one baseline gives information along the direction of the baseline. Hence, if one were to change the baseline's direction and make another measurement, and so on, one would slowly fill the (u,v) plane. Then theoretically, the Fourier transform can be calculated to give the actual stellar image. In practice, the (u,v) coverage is sampled on a finite number of points, resulting in an approximative image, which is consequently compared to models.

The phase information, which we saw contains the astrometric signal, is accurately determined when at least three telescopes are used together, by cancelling out the phase fluctuations with the *phase cloture* method.

With the newest generation of instruments (AMBER, VINCI and CHARA), combining the light of up to six telescopes, the phase closure requirements are satisfied. Hence astronomers made use of the imaging possibilities offered by these instruments to determine the shape of far rotating stars. These stars have a rotational velocity in the hundred of kilometers per second. They are deformed by the centrifugal force. As a result, by measuring the oblateness of the star, one can determine the orientation of its rotation axis. Altaïr, an AIV type star, was the first star for which the oblatness was directly observed by van Belle et al. (2001). The breakthrough came with the verification of gravitational darkening in fast rotators caused by the von Zeipel effect. It predicts that the equator of the star should be darker than the more slowly rotating poles. With this theory, the spin rotation of stars seen nearly pole on can be retrieved from the observation, e.g Vega by Peterson et al. (2006b). The reconstructed images used for some of these stars are reproduced in the Figure 1.5. At this date less than 10 stars have determined position angles through this method.

Since the determination strategy relies on the measurement of the stellar oblateness, the sample includes mainly A and B type stars as stable fast rotators, as noted in the Table 1.1. β Cas, being of
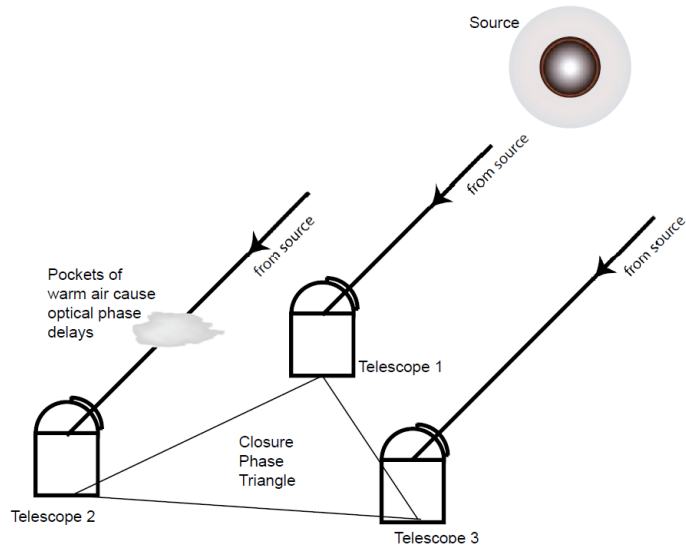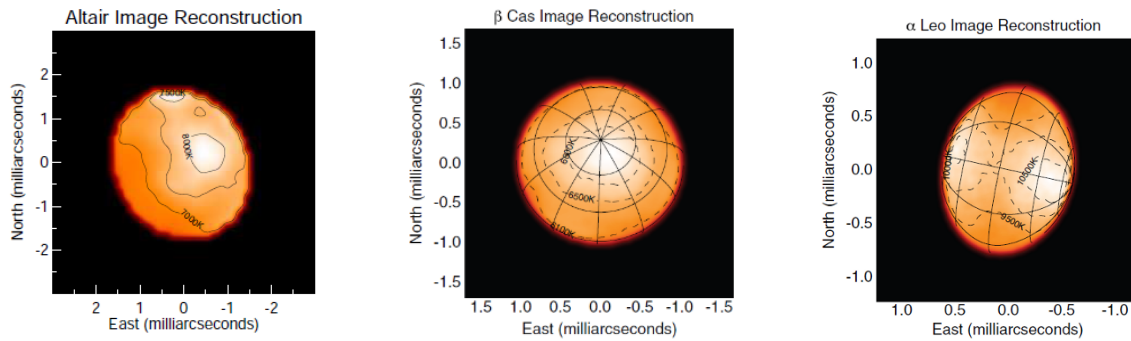
Figure 1.4: Atmospheric turbulences introduce additional path lengths causing fluctuations in the phase. With the three telescope set-up and using phase closure, the true phase information is retrieved. The figure is reproduces from Monnier & Allen (2012).

(a) Reconstructed image of Altaïr by Monnier et al. (2007) and with CHARA.

(b) Reconstructed image of β Cas by Che et al. (2011) with CHARA.

(c) Reconstructed image of α Leo by Che et al. (2011) with CHARA

Figure 1.5: Resolved giants with long baseline interferometry.

F2III-IV type, is believed to be a "retired" A star, which has evolved from the main sequence. Hence the rotation velocity has decreasing during its evolution. However this observational method cannot be applied to cooler stars with lower rotational velocity. Their oblateness would not be measurable with sufficient precision to retrieve the spin axis. In addition, cooler stars do not present the gravitation darkening effect.

To sum this up, the strategy described above, which relies on oblateness measurements and gravitational darkening, is devised exclusively for stars which present these features, mainly A and B type giant stars. This work deals with the development of an alternative technique which would be optimsed for the observation of cool stars, like giants, with low rotational velocities.

Star	Spectral Type	Velocity km/s	Position angle deg	References
Achernar (α Eri)	B3Vpe	225	39 ± 1	Domiciano de Souza et al. (2003)
Regulus (α Leo)	B8IVa	~ 320	85.5 ± 5 250^{+2}_{-1}	McAlister et al. (2005) Che et al. (2011)
Vega (α Lyr)	A0V	270	8.6 ± 2.7	Peterson et al. (2006b)
Rasalhague (α Oph)	A5IV	237	-53.88 ± 1.23	Zhao et al. (2009)
Altaïr (α Aql)	A7IV-V	~ 280	-68.4 ± 6.2 123.2 ± 2.8 -61.8 ± 0.8	van Belle et al. (2001) Peterson et al. (2006a) Monnier et al. (2007)
Alderamin (α Cep)	A7IV-V	~ 250	3 ± 10 -178.84 ± 4.28	van Belle et al. (2006) Zhao et al. (2009)
Caph (β Cas)	F2III-IV	72.4	$-7.09^{+2.24}_{-0.034}$	Che et al. (2011)

Table 1.1: Stars with known position angle determined with long baseline interferometry.

Chapter 2

Spectro-Astrometry

Spectro-astrometry is an observational technique which emerged in the late eighties. It's first evocation was under the name of *cross-spectral dispersion imaging*, in 1989 as *" a new observational technique which can achieve super-Rayleigh angular measurements for binary stars"*[1]. The term spectro-astrometry itself was coined by Bailey (1998*b*) as a tool for finding pre-main sequence binaries. He applied the astrometric reduction method to his spectra and separated the otherwise unresolved components of the binary along with their individual spectral type. His work pioneered the method to the astronomical community.

Since its début, spectro-astrometry was continuously applied for finding and studying binary stars. In their recent work on Herbig binaries Wheelwright et al. (2010) could disentangle the spectra of both components, and determine their respective masses. Moreover it was also successfully applied to the study of stellar outflows by Whelan & Garcia (2008), in order to characterize the spatial and kinematic properties of forbidden lines emission regions. Finally Voigt & Wiedemann (2009) probed the surface of the cool giants TW Oph and RS Vir with CRIRES. Using a spectro-astrometric analysis they identified and located stellar spots leading to the mapping of stellar surface. To conclude, spectro-astrometry provides a means to study astronomical structure on scales almost comparable with those achievable with interferometry.

These milliarcsecond scales are reached thanks to the advance in the astrometric analysis caused by the arrival of digital images. The first section deals with a brief history of astrometry and involves a short explanation of the astrometric reduction. Since spectro-astrometry also relies on spectroscopy, the section 2.2 explains in detail the set-up of a spectrograph and the notions of spectral dispersion and spectral resolution. Finally, the section 2.3 explains the working principle of spectro-astrometry with some understanding examples, and is followed by a discussion about the available extraction methods.

2.1   Astrometry

Astrometry deals with the determination of the precise position of an unresolved source, in most cases a star. This positional problem has been studied since the early days of astronomy and is still contemporary in modern astronomy. Before the arrival of recording devices, the stellar positions were determined visually and lacked in precision. One of the initial applications of astrometry is the measurement of stellar parallaxes, from which the distance of the stars to the Sun is calculated. Before the use of photographic plates in observations, corresponding approximatively to the beginning of the 20th century, only 60 parallaxes were known. The field experienced a huge expansion with the arrival of CCD (Charged Coupled Devices) in the mid seventies which lead to the developments of space missions[2]. The HIPPARCOS satellite provided during its 3.5 years of operations (from the launch

---

1. The work was led by Endal et al. (1989) and presented at the 175th AAS meeting in Washington.

2. Sending a observation satellite using photographic films had already been done by the NASA during the Lunar Orbiter missions from 1966 to 1968. On the Lunar Orbiters, the film was developpend on board, scanned and transmitted

in August 1989 to March 1993) the positions of over 100,000 stars with precisions down to 1 mas. The latest generation of astrometric missions includes GAIA (launch date mid 2013, for a minimum 5 year mission), or the ground based LSST survey (estimated date for first operation in 2022).

Astrometric reduction means extracting only a few measurements out of the total images: the position of the star and eventually its intensity and its width. The extraction of these measurement is not limited by the resolution of the image, hence there is no need to proceed to a deconvolution of the total image. On the contrary, several methods have been devised to extract only the required dimensions: weighted arithmetic mean of the star and its neighbourhood, Gaussian fitting over the star, or median centring over several images. As a result, the precision of the measurement is not set by the angular resolution of the telescope, but by the detector itself. With precisions in the subpixel scale (current accuracies are in the order of 1% of a pixel), higher precision and better accuracy are limited by the sensor's inhomogeneities. Hence, despite a seeing-limited angular resolution in the images, an astrometric measurement delivers positions with a precision close to the diffraction limit.

2.2 Spectroscopy

2.2.1 Instrument Nomenclature

As an abuse of language, the instruments used for spectroscopy are often called *spectrometer*, *spectroscopes* or *spectrograph* without distinction. However the three terms described slightly different instruments. A *spectrometer* is an instrument which allows to analyse any property of light as a function of its wavelength. The property being measured is usually the intensity, but other variables like polarization can also be measured.A *spectroscope* measures the spectrum of light. It has a slit, a dispersing element and a screen with marking. The analysis is done in real time and with the naked eye. Finally, a *spectrograph* is an instrument which separates the incoming light according to wavelength and records the resulting spectrum on a detector. In other words, a spectrograph is the modern version of the spectroscope. In astronomy, spectroscopy is done with spectrographs coupled to a telescope.

2.2.2 Dispersion

The purpose of a spectrograph is to separate the stellar light into a large number of distinct wavelength elements. On modern spectrographs, this is realized with a dispersion grating. It consists of a collection of reflecting, or transmitting, elements separated from each other by a distance comparable with the wavelength of light. A grating can be approximated as a succession of parallel orientated narrow slits with a spacing d. Considering two adjacent grooves as two slits, the path difference between two beams incoming at an incident angle α from the grating normal is expressed by $\Delta p = d \sin \alpha$. The light coming through the two slits produces a series of stripes, known as fringes, as interference pattern. The distance between the maxima of two bright fringes coincides to an integer wavelength path difference:

$$\Delta p = d \sin \alpha = m\lambda \tag{2.1}$$

where m, an integer, is the *diffraction order*, and d is the *grating constant*. From this relation, it is possible to derive the grating equation :

$$\boxed{m\lambda = d(\sin \alpha \pm \sin \beta)} \tag{2.2}$$

where α and β are respectively the incident and diffracted angle from the grating normal. If $\alpha = \beta$, then the grating is being used in Littrow configuration. If the incident and the diffracted beams lie on the same side of the grating, it is a reflection grating, and the sign in the equation 2.2 is "+". If the

---

to the Earth. However the resulting images were of poor quality, the films were affected by the high radiations in space, and the number of images were limited.
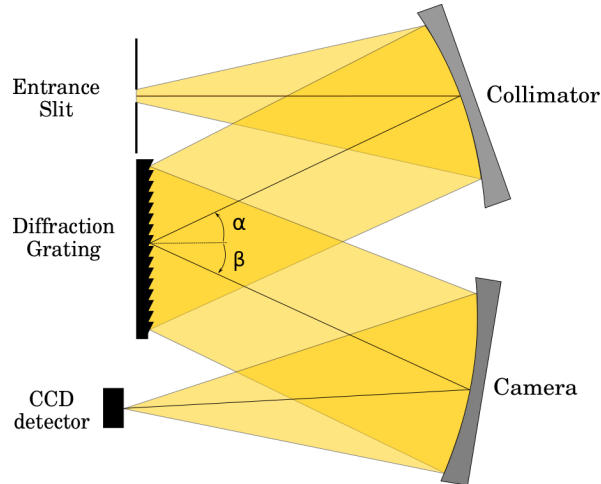
Figure 2.1: Basic set-up of a spectrograph under Czerny-Turner design. The light from the telescope is focused on an entrance slit which blocks all rays except those from the star. The beam is collimated and projected toward the Échelle grating at an angle close to the blaze angle of the grating. The diffracted light is then imaged on a detector.

diffracted beam lies on the opposite side of the grating from the incident beam, it is a transmission grating, and the sign is "-". Hereafter we'll work only with reflecting grating. A basic set-up for a spectrograph is illustrated in Figure 2.1.

Since the purpose of a grating is to disperse the light as a function of wavelength, the gratings are quantified by their dispersion power. The angular dispersion is given by differentiating the grating equation for a constant incident angle α:

$$\frac{\delta\beta}{\delta\lambda} = \frac{m}{d\cos\beta} \qquad (2.3)$$

The larger the angular dispersion, the better two wavelengths are separated. As hinted in the equation 2.3, the angular dispersion can be increased either by lowering the grating constant, causing a shift of the observed wavelength range [3], or by increasing the diffraction order. This is achieved with the *Échelle* gratings. Their grooves are individually tilted from the grating plane by an angle called the *blaze angle*, θ_B, and illuminated close to the normal of the groove surface. The maximal efficiency of the grating is reached at the *blaze wavelength*: $\lambda_B = 2\sin\theta_B/m$ in Littrow configuration. As a result, the diffracted light is concentrated mainly in the high diffraction orders, at the cost of an order overlap. Therefore, *Échelle* gratings are mostly used in combination with a cross-disperser, i.e another dispersing element like a grating or a prism, to separate the diffracted orders on the detector. Consequently, the orders are distributed over the detector like stairs [4], the intensity of each order given by the blaze function. This function describes the intensity distribution along the dispersion direction. The wavelength dependent variations in intensity of the order are of neglectable influence in our work, since it concentrates on the spatial properties of the order.

---

3. For understanding let us take two existing ruled gratings, the first has 5880 lines/mm, and an blaze angle of 24°. The nominal blaze wavelength, which is the wavelength where the grating has its highest efficiency, is 138 nm. Another grating has similar blaze angle, but only 1700 lines/mm, its blaze wavelength is 530 nm. So increasing the number of lines per millimetre at similar blaze angle equates to shift the observed wavelength range.

4. Here comes the name Échelle, stairs in French.

2.2.3 Resolving Power

The spectrograph is also characterized by its resolving power, which is its ability to separate adjacent spectral lines. It is defined as a dimensionless quantity, R, called the spectral resolution:

$$R = \frac{\lambda}{\Delta\lambda} \tag{2.4}$$

where $\Delta\lambda$ is the smallest wavelength difference measurable at the wavelength λ. By inserting the grating equation and the dispersion relation respectively, the spectral resolution is expressed by:

$$R = \frac{\sin\alpha + \sin\beta}{\cos\beta\Delta\beta} \tag{2.5}$$

If the spectrograph is attached to a telescope with a main mirror size of D, the quantity of light reaching the spectrograph is limited because of the *Étendue conservation*. This optical law stipulates that the product $A\Omega$, where A is a surface and Ω the solid angle seen from this surface, is constant. This is translated here by

$$D\phi = W_\alpha\Delta\alpha = W_\beta\Delta\beta \tag{2.6}$$

where W_α and W_β are respectively the diameters of the incident and dispersed beams, and ϕ the angular size of the observed star. After insertion in the equation 2.5, the resolution of the spectrograph is:

$$R = \frac{L(\sin\alpha + \sin\beta)}{D\phi} = \frac{\Delta p}{\lambda}\frac{\lambda}{D\phi} \tag{2.7}$$

where, L is the effective grating length, or the used grating length, calculated from $W_\beta = L\cos\beta$ and Δp is the path difference of the incoming and outgoing beam. The term $\lambda/(D\phi)$ is at most equal to one. Most spectrographs use an entrance slit which is smaller than the projected size of the star due to seeing. Consequently, ϕ tends to describe the projected slit angle on the sky rather than the actual stellar angular size. This is not of influence in this work, since I focus on the information comprised in the slit height, rather than in the slit width. As expressed by the equation 2.7, in order to keep a constant resolution with increasing telescope size, one can either increase the size of the grating, or reduce the size of the slit. The former has become a challenge for the very large and the upcoming extremely large telescopes, because ruled grating can be produced only up to a limited size with the actual equipment. Hence, the future generation of spectrograph may be coupled to adaptive optic systems to compensate the light losses caused by extremely narrow slits.

2.3 Spectro-Astrometry

Spectro-astrometry is best suited for sources with a structured spectral energy distribution. Structured is meant both in a spectral sense, the source should feature emission or absorption lines in addition to the black body emission called the continuum, and in a spatial sense, the overall spectral emission changes over the source. Thus, while the seeing or diffraction limited image of the source present a homogeneous bright spot, the measurement of the position of the photocenter of the spectrum reveals out of the spectral energy distribution the hidden structure in the source.

Every object in the sky has an structured spectral energy distribution, either due to a asymmetries in the shape, as in binaries, accretion disk or even galaxies, or due to spectral asymmetries caused by stellar spots, or Doppler effect. Hence, every object could be observed with this technique provided it presents sufficient spectral features.

2.3.1 Principle

By definition, spectro-astrometry is the measurement of the wavelength dependence of the position of an object. The method relies on the conservation of the spatial information through the
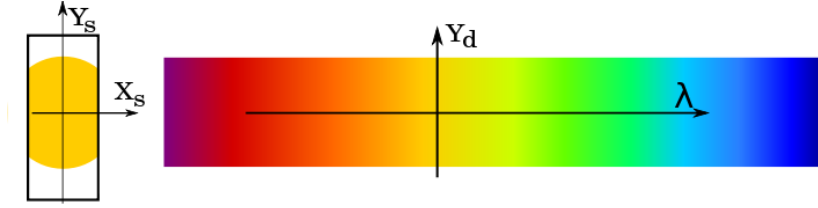
Figure 2.2: Notation used for spectro-astrometry

spectrograph. Let us denote X_s and Y_s the slit coordinates in dispersion and spatial direction respectively. The object, projected on the slit at the entrance of the spectrograph, is imaged as a spectrum on the detector. So let λ and Y_d be the detector coordinates along the spectral and in spatial direction respectively. Each point (X_s, Y_s) of the slit is transformed by the spectrograph into another pair (λ, Y_d) on the detector. The conversion of Y_s into Y_d is a homothetic transformation, by definition reversible: $Y_d = K\, Y_s$ where K is the magnification factor fixed by the spectrograph's optics. They are chosen to fulfil Nyquist's law of sampling, meaning that the image of the slit is sampled by 2 pixels on the detector [5]. Consequently the magnification factor is derived from the focal length ratio of the camera optics to the collimator optics. As a result the homothetic transformation of the spatial coordinates is:

$$Y_d = \frac{f_{camera}}{f_{collimator}}\, Y_s \qquad (2.8)$$

The *plate scale* is a dimension introduced to reformulate this relation in detector units. It expresses in arcsec/pixel and is directly dependent of the magnification factor K and the pixel size.

The transformation of X_s into λ is not reversible. The position of the source on the dispersion axis of the slit leads to small changes in the incident angle of the grating. Once the spectrograph's optics are known, the conversion is easily done and is reversible: $\delta X_s \Leftrightarrow \delta\alpha$. According to the grating equation, for a wavelength λ the dispersion angle is given by:

$$\delta\beta = \frac{\cos\alpha}{\cos\beta}\delta\alpha \qquad (2.9)$$

which means that small variations in the incident angle cause variations in the dispersion angle $\alpha + \delta\alpha \Rightarrow \beta + \delta\beta$. This means that the wavelength λ is dispersed at another angle as before, and is located on the detector at another position. Therefore, a shift of the star's position on the slit results in a shift of this constant wavelength on the detector. The position itself on the detector being dependent of the optics of the spectrograph. As a result, there is a constant K', defined from the optics of the spectrograph, which satisfies the relation: $\delta X_s \Rightarrow K'\, \delta\lambda$.

Since only the information along the slit's spatial direction is conserved, spectro-astrometry probes only a single direction. Hence to retrieve the global features of the source, it is necessary to turn the spectrograph's slit. In order to remove possible instrumental artefacts, observations are taken in anti-parallel orientation, i.e once at 0° and once at 180°. In his work, Bailey (1998*a*) recommanded to take spectra under the following orientations 0, 90, 180, and 270 in order to cover the anti-parallel orientation and to probe at least 4 directions.

Let us illustrate the working principles of spectro-astrometry on a very basic example. In the following paragraph, I assume that we observe two stars, which have respectively only one absorption line, and one emission line. The separation between the two stars is very small, and we observe under standard seeing condition. Hence the projected image of our two stars present only a uniform disc on the slit, as illustrated in Figure 2.3. However by measuring the position of the photocenter for each wavelength, i.e. the position of the barycenter of the order, and with the knowledge of the spectral profile, the two imaginary stars can be separated.

---

5. The Nyquist's law predicts that continuous features can be retrieved out of a discrete measurements if the sampling is done at 2.2 discrete elements. If the number of samples is bigger, one speaks of oversampling. In astronomy, and especially in spectroscopy, the images are often slightly undersampled.
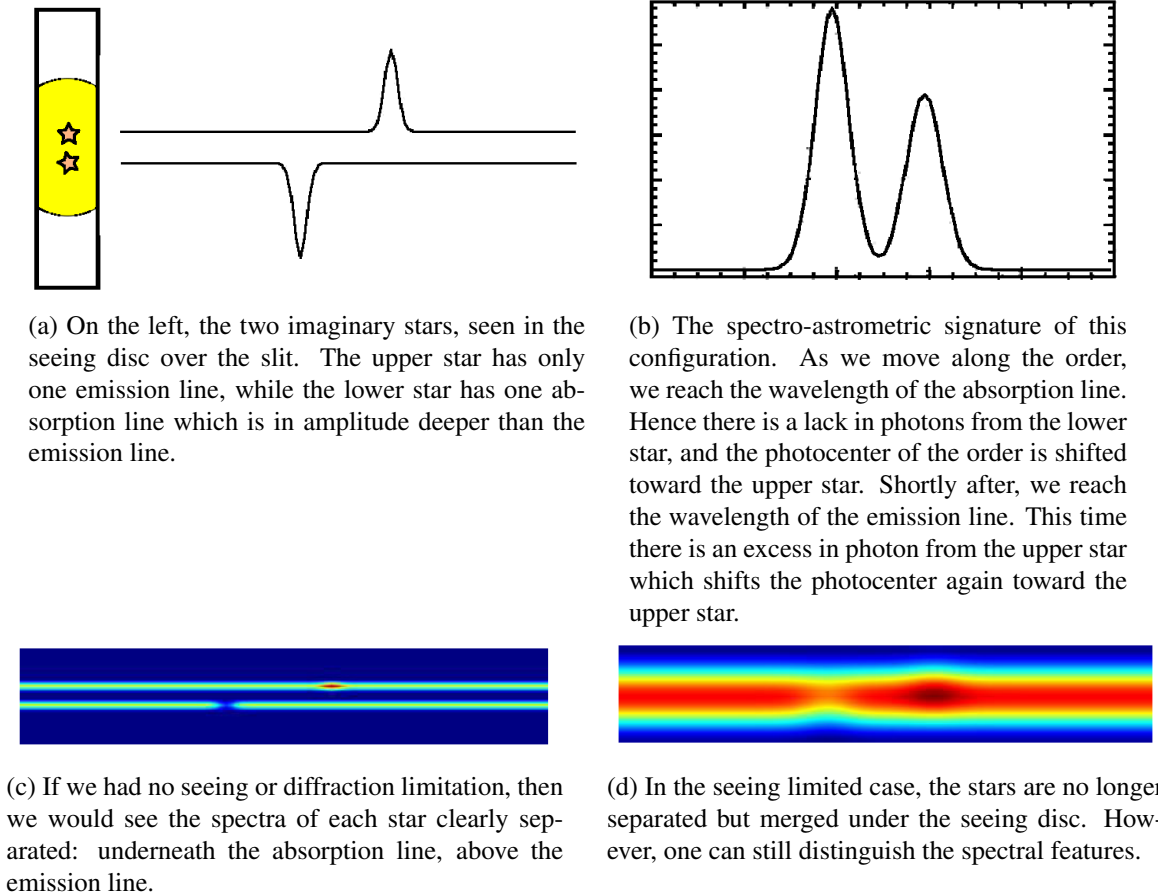
(a) On the left, the two imaginary stars, seen in the seeing disc over the slit. The upper star has only one emission line, while the lower star has one absorption line which is in amplitude deeper than the emission line.

(b) The spectro-astrometric signature of this configuration. As we move along the order, we reach the wavelength of the absorption line. Hence there is a lack in photons from the lower star, and the photocenter of the order is shifted toward the upper star. Shortly after, we reach the wavelength of the emission line. This time there is an excess in photon from the upper star which shifts the photocenter again toward the upper star.

(c) If we had no seeing or diffraction limitation, then we would see the spectra of each star clearly separated: underneath the absorption line, above the emission line.

(d) In the seeing limited case, the stars are no longer separated but merged under the seeing disc. However, one can still distinguish the spectral features.

Figure 2.3: Explanation of the spectro-astrometric working principle based on a simple example.

2.3.2 Extraction of the Position Spectrum

The position spectrum results from the measurement of the photocenter's position for each wavelength, i.e. for each pixel of the detector along the spectral order. Stellar rotation induces a small tilt in the absorption lines [6]. The corresponding displacement of the photocenter on the position spectrum is expected to be around 1 and 5% of a pixel, depending on the spatial resolution of the spectrograph. Hence the extraction method and the evaluation of the errors are decisive for the detection.

For a star which does not fill completely the slit height, the spatial profile along the order follows ideally a Gaussian distribution around the photocenter. Hence its position is determined either by fitting a Gaussian to the spatial profile, or by calculating the weighted arithmetic mean, hereafter the barycentrum or the centroid extraction, of the order at this wavelength.

Considering a pair of measurements (x_i, F_i), of the independent variable x, representing the spatial location in cross order direction, and a dependant variable F, linked to the intensity distribution at that wavelength, then the maximum-likelihood Gaussian fit is the one which minimizes χ^2:

$$\chi^2 = \sum_{i=1}^{N} \frac{(F_i - f(x_i))^2}{\mu_i^2} \tag{2.10}$$

The measured values F_i have a mean value F_o and a standard deviation μ_i. In addition, I suppose that the F_i measurements yield the same standard deviation μ. $f(x)$ is the Gaussian function around the

---

6. The explanation of the origin of the tilt and a discussion of the optimisation parameters is developed in the next Chapter.

position x_o with a width σ and an amplitude A:

$$f(x) = A \, exp\left(\frac{-(x - x_o)^2}{2\sigma^2}\right) \tag{2.11}$$

For each of the parameters p_k, e.g. $p_1 = x_o$, $p_2 = A$ and $p_3 = \sigma$, finding the set that minimizes χ^2 is equivalent to fixing to zero the partial derivatives of χ^2 in respect to each parameter:

$$\frac{\partial \chi^2}{\partial p_k} = 0 = \frac{2}{\mu} \sum_{i=1}^{n} (F_i - f(x_i)) \frac{\partial f(x_i)}{\partial p_k} \tag{2.12}$$

The linearisation of these equations can be approximated through the Taylor-series:

$$(F_i - f(x_i)) \approx \sum_{j=1}^{3} \frac{\partial f(x_i)}{\partial p_j} dp_j \tag{2.13}$$

which leads to the final expression:

$$\frac{\partial \chi^2}{\partial p_k} = 0 = \sum_{i=1}^{n} \sum_{j=1}^{3} \frac{\partial f(x_i)\partial f(x_j)}{\partial p_k \partial p_j} dp_j \quad k = 1 \ldots 3 \tag{2.14}$$

The right term of the equation 2.14 fills an $n \times n$ diagonal matrix $\mathbf{D}$ of linearised equations. Since the measurements are taken for each pixel, I can legitimately assume that the spacing between each point x_i is uniform, constant and equal to h. Moreover, the peak of the Gaussian distribution is well sampled across the order. Hence, the previous sums are similar to Riemann's sums and can be transformed into integrals without important losses of accuracy.

$$\sum_{i=1}^{n} \frac{\partial f(x_i)\partial f(x_j)}{\partial p_k \partial p_j} \approx \frac{1}{h} \int_{-\infty}^{\infty} \frac{\partial f(x)}{\partial p_k} \frac{\partial f(x)}{\partial p_j} dx = D_{kj} \tag{2.15}$$

Let us expand the coefficient of the matrix corresponding to the amplitude parameter:

$$D_{22} = \frac{2}{h} \int_{-\infty}^{\infty} \exp\left(\frac{-(x - x_o)^2}{2\sigma^2}\right) dx$$
$$= \frac{\sigma\sqrt{\pi}}{h}$$

The error distribution of the fitted parameter are deduced from the inverse matrix $\mathbf{D}^{-1}$, called the *error matrix*. The variance of each parameter is denoted $\mu^2(p_k)$ and defined as:

$$\mu^2(x_o) = \mu^2(\sigma) \tag{2.16a}$$

$$\mu^2(A) = \frac{3\,h}{2\,\sigma\sqrt{\pi}}\mu^2 \tag{2.16b}$$

$$\mu^2(\sigma) = \frac{2h\,\sigma}{\sqrt{\pi}\,A}\mu^2 \tag{2.16c}$$

Condon (1997) proposed an elegant simplification of these equations by introducing a parameter representing the signal to noise ratio of the fit: $SNR^2 = A^2\sigma\sqrt{\pi}/\mu^2 h$. Finally the error estimates for the position of the Gaussian fit, and its width are:

$$\mu^2(x_o) = \mu^2(\sigma) = \frac{2\sigma^2}{SNR^2} \tag{2.17}$$

$$\mu^2(A) = \frac{3}{2}\frac{A^2}{SNR^2} \tag{2.18}$$

Since the estimation of the Gaussian width is usually done with the Full Width at Half Maximum (FWHM) instead of the width σ, the conversion is done with $FWHM = \sqrt{8\,ln2}\,\sigma$.

To summarize, the errors from the Gaussian fit are proportional to the ratio of the FWHM of the curve to be fitted and the Signal to Noise ratio of the measurements. The precision can be enhanced either by capturing more photons, i.e. a higher signal to noise, or by increasing the number of lines considered. The latter method is developped in the Section 3.2.2. The FWHM is minimized by observing stars with narrow absorption lines.

$$\boxed{\delta x_o \approx \frac{FWHM}{SNR\sqrt{N_{lines}}}} \tag{2.19}$$

Contrary to the Gaussian fit method, the determination of the barycentre, hereafter called the centroid method does not rely on a fit but exclusively on the data. Indeed the estimation of the centroid is calculated from:

$$B(\lambda) = \frac{\sum_{i=1}^{n} x_i F_i}{\sum_{i=1}^{n} F_i} \tag{2.20}$$

where the x_i are for instance pixels and the F_i the intensity of these pixels. The errors are directly deduced from an error propagation analysis, assuming photon noise in the intensity distribution:

$$\delta B = \sqrt{\frac{\sum_i F_i \left(x_i - B\right)^2}{\left(\sum_i F_i\right)^2}} \approx \frac{1}{SNR} \tag{2.21}$$

Using this formula, I studied the dependency of the centroid errors with the signal to noise ratio of the image. Similarly to the Gaussfit errors, the centroid errors follow a 1/SNR rule, as illustrated on the Figure 2.4. Since the centroid extraction relies directly on the data, it should be more sensitive to deviant pixels than the gaussfit method. Hence, I compared the position spectra obtained from both extraction methods in the specific case where the simulated order displays highly diverging pixels. The result presented on the Figure 2.5 shows that, contrary to expectations, both method are sensitive to the presence of bad pixels. Moreover, the position spectrum obtained with the gaussfit method presents higher divergences than the spectrum obtained with the centroid extraction. The presence of bad pixels is therefore directly visible in the position spectrum. It can be used as a mean to identify them, and to verify the correction of the data to remove them. In a worst case scenario, setting the deviant pixel of the position spectrum to the continuum value would not affect too much the detection of the signal.
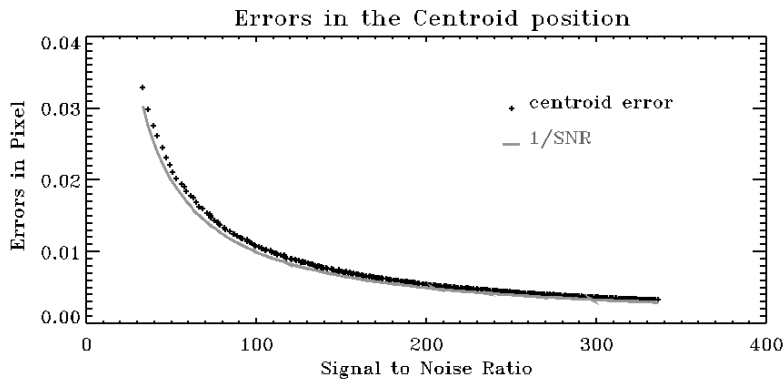

Figure 2.4: The dependency of the centroid errors with the Signal to Noise ratio of the image.

In the ideal case where the spatial profile of the order follows a perfect Gauss curve, then both methods yield similar results. However, in practice the spatial profile diverges from ideality, due for
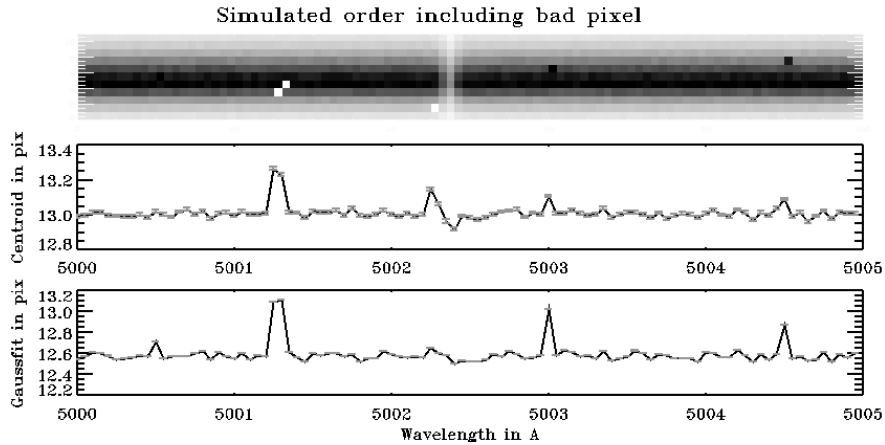
Figure 2.5: Influence of bad pixels in the estimation of the position spectrum. *On top*, the simulated order, with hot and cool pixels dispatched randomly and a line tilt of 0.25 pixel. *In the middle*, the position spectrum after centroid extraction. *On the bottom*, the position spectrum after gaussfit extraction. The bad pixels are clearly identified, and generate a higher signal here than in the centroid extraction.

instance to stray light in the instrument or a partial blocking of the light at the slit if the star is not well centred... Finally I compared the two extraction methods for the specific astrometric signal of stellar rotation [7]. I studied the evolution of the position spectrum for increasing signal to noise ratio, and a decreasing amplitude in the spectro-astrometric signature. In order to test the two methods in conditions close to real, the cross dispersion profile is asymmetric around the position of the peak. The FWHM of the peak is around 5 pixels corresponding to a seeing disk of $1''$ and a plate scale of $0.2''$/pix. I assumed here that the spatial profile is corrected of any deviant pixel, which would influence the results in the centroid extraction.

The spectral profile includes three absorption lines with various depth and identical width. An uniform noise distribution extrapolated from the signal to noise ratio is added to the simulated order in order to reproduce the photon and read out noise. The gaussfit extraction is done with MPFITPEAK a robust non linear least-square fitting procedure of Markwardt (2009) for IDL [8]. The position spectrum is expressed in pixels in order to shed light to the small displacements involved here.

As illustrated in the Figure 2.6, both method yield comparable results for moderate SNR and a large spectro-astrometric signature. The displacement in this simulated situation span from 4% to 1% of a pixel for the deepest and the shortest lines respectively. The Gaussfit method has the lowest errors, but an important scattering in the location of the photocenter. On the opposite, the centroid method present a lower scattering and a better detection of the short line, yet the errors are two orders of magnitude bigger.

I made a Monte-Carlo simulation to estimate the detection rate for each extraction method in dependency of the line depth and line tilt. The spectro-astrometric signature is detected if the amplitude of the signal is above 2σ of the continuum of the position spectrum, and at the correct position. The latter is checked with the dispersion profile in order to avoid false-positive detections. The method takes only one line into account. Therefore it produces a lower estimation of the detection possibilities for each method. However, the centroid extraction method is clearly more sensitive to the small lines, despite the higher errors, see Figure 2.7.

---

7. The discussion about the origin and shape of the signal is developed in the next chapter. I just state here that stellar rotation causes a tilt in the line of a few percent of a pixel.

8. Actually, IDL has its own gaussfit procedure, GAUSSFIT, but it proved to be less robust than MPFITPEAK and happened to have too often diverging points. With this insight, I chose the external MPFITPEAK procedure which diverged notably less often.
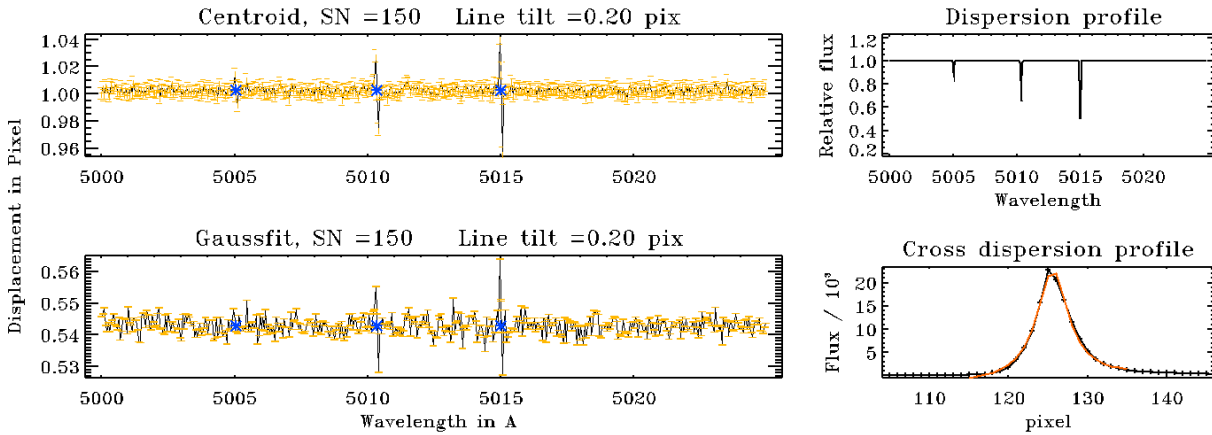
Figure 2.6: Comparison of the extraction methods for a simulated seeing disk or $1''$ and a plate scale of $0.2''$/pix. On the upper right, the dispersion profile presenting three absorption lines of various depth. On the right bottom, the simulated spatial profile, which is asymetric around the peak's position, overlapped with the best gaussian fit in red. On the left, the position spectra of each extraction method. Both method detect the three lines with displacements from 4% to 1% of a pixel. However the signal amplitude is more important in the barycentric than in the Gaussfit method.
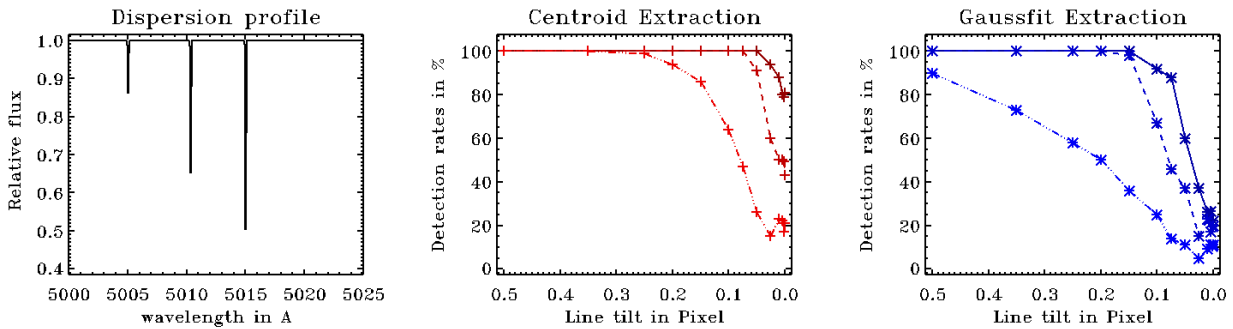
Figure 2.7: Detection rates of each method for decreasing line depth and a constant signal to noise ratio of 150. *Left:* The dispersion profile adopted for the simulation, the lines have increasing depth but constant width. *Middle and Right:* In straight lines, the detection rates for the deepest line, in dashed lines, the rates for the middle lines, and at last in dotted lines the rates for the shortest line.

To conclude, the centroid extraction method has proved to be more efficient in the detection than the gaussfit extraction method. Both methods are equally sensible to bad pixels in the spatial profile. Therefore, I shall use the centroid method for the extraction of the position spectrum.

Chapter 3

Stellar Rotation Signature

In the second part of the 19th century, when astronomers started to classify the stars according to their observed spectra, leading to the stellar classification **O B A F G K M** which is still commonly used, they noticed that some spectral lines, which were present in several stellar types showed variable widths. They linked this line broadening to the radial velocity of the observed star [1]. Empirically the connexion is easily demonstrated. The Doppler effect stipulates that for an source moving toward the observer, the spectrum is shifted toward higher frequencies, hence toward the blue, while a source moving away from the observer has its spectrum shifted to longer frequencies, i.e. the red. On a rotating star, one part is moving to us and one away. Thus, the lines are simultaneously shifted toward the blue and the red: they are broadened.

For the purpose of further analysis, the image of the stellar spectrum is usually reduced to an one-dimensional spectrum, by collapsing the order along the dispersion direction. This enables the exact characterisation of the shape of the absorption lines, known as line profile. Astronomers started to monitor the variations of the profile for stars with increasing rotational velocities. They realised that the faster the star rotates, the more its line profile is dominated by the broadening profile. Therefore, it became clear that the broadening effect is "overlaid" to the intrinsic stellar spectrum. One then speaks of the convolution between the two profiles, intrinsic stellar profile and broadening profile. There have been several attempts to derive an analytic form for the broadening function. Finally, in 1976, Gray (2008) demonstrated that the function describing accurately the line broadening due to the stellar rotation, is analytically very close to a half ellipse. However, the function is one-dimensional, and does not take into account the position angle of the star in the sky.

This chapter concentrates on the effects of stellar rotation on stellar spectra. First, I derive a two dimensional function for the line broadening based on the calculations of Gray. Then in section 3.2, I show how this line tilt signature can be extracted, either by monitoring the width or by spectro-astrometric reduction. At last in section 3.2.2 I present simulations of the spectro-astrometric signal and detection analysis.

3.1 Two Dimensional Rotation Model

The star is no longer assumed to be a point source and it is projected with a random orientation on the slit. It is assumed to rotate as a rigid body. Hereafter I adopt the notation conventions defined in the Figure 3.1: the observer's referential has the same orientation that the slit referential, and I assume that the observer knows under which angle the slit is projected to the sky. The stellar rotation is defined positive counter-clockwise, with an angular velocity vector Ω. The stellar rotation axis

---

1. Rotational broadening is one of the line broadening sources. I insist here only on this one since this work focuses on rotational signal. Yet, macro-turbulences at the surface are also causes to line broadening, or strong magnetic fields. Using spectral observations, it is possible to determine whether a star has strong macro-turbulence or not. Such stars would be discarded for our work.

and the projected slit spatial axis on the sky form an angle ψ, which is defined positive from the slit toward the spin axis; and at last each point of the stellar surface is described by the coordinates X and Y which are linked to the star's diameter by the straightforward relation: $X^2 + Y^2 = R_{star}^2$
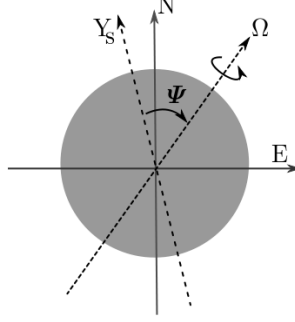

Figure 3.1: Notation conventions adopted in this chapter. The absolute stellar position angle is defined from North to East. The slit is represented by the spatial axis Y_S, which may not be aligned toward North.

Expressed in the slit referential, and taking into account the referential rotation $\vec{R}$ between star and slit, the radial velocity of any point of the star is:

$$\vec{v} = (\vec{\Omega} \times \vec{r}) \times \vec{R}$$
$$\Rightarrow v_z(X, Y, \psi) = \Omega \sin i \ (X \cos \psi - Y \sin \psi) \tag{3.1}$$

This is converted into a wavelength shift using the Doppler relation:

$$\Delta\lambda_{v_z} = \frac{v_z}{c}\lambda \tag{3.2}$$

Thus, the wavelength shift due to stellar rotation, for each point of the star, is:

$$\Delta\lambda_{v_z}(X, Y, \psi) = \frac{\Omega \sin i \ \lambda}{c} (X \cos \psi - Y \sin \psi) \tag{3.3}$$

The star is not a point source, but neither is it resolved on the slit. It has a geometrical extension. We saw in the previous Chapter that $\delta X_s \Rightarrow \delta\lambda$. At constant dispersion angle β, I obtain from the derivation of the grating equation:

$$m\,\delta\lambda = d\cos\alpha\delta\alpha \tag{3.4}$$

With the Étendue relation defined in the Equation 2.6, the right-hand term of the equation can be replaced by: $D\phi_{star} = L\cos\alpha\,\delta\alpha$, (D being the diameter of the primary mirror, and L the effective grating length) which leads to the geometrical wavelength shift:

$$\delta\lambda_{geo}(X) = \frac{dD\phi_{star}(X)}{mL} \tag{3.5}$$

ϕ_{star} is the apparent diameter of the star on the slit, without the seeing disk. It is expressed usually in arcsec, and results from the relation: $\phi_{star}(X = R_{star}) = 2R_{star}/pc$, where pc is the distance of the star in Parsec, and R_{star} is expressed in AU. Hence, the Equation 3.5 reformulated with X (in AU) results on the geometrical shift:

$$\delta\lambda_{geo}(X) = \frac{d\,DX}{m\,L} \times \frac{2}{pc} \leq \frac{d\,\phi_{star}}{m\,R\,\phi_{slit}} \tag{3.6}$$

The final wavelength shift for each point of the star is the sum of the velocity shift from Equation 3.3 and from the geometrical shift:

$$\Delta\lambda(X, Y, \psi) = \delta\lambda_{geo}(X) + \Delta\lambda_{v_z}(X, Y, \psi) \tag{3.7}$$
$$= \frac{dDX}{mL} \times \frac{2}{pc} + \frac{\Omega \sin i \ \lambda}{c} \times (X \cos \psi - Y \sin \psi)$$

The orders of magnitude involved here can be estimated by taking a typical observation case. I considere a star of diameter 5 mas, and a rotational velocity of 5 km/s. It is observed by a high resolution spectrograph (R = 60 000 with a slit width of 0.5″) mounted on a 2m telescope. The grating has 31.6 lines/mm and the observation takes place at the 100th spectral order. The Doppler shift is estimated around 10^{-1}Å, and the maximum geometrical shift, calculated from the Equation 3.6, is around 10^{-3}Å. Hence, the geometrical shift is around two orders of magnitude smaller than the Doppler shift.

Nevertheless, due to the different parameters at work, the value of the geometrical shift can be enhanced without increasing simultaneously the value of the Doppler shift. Equation 3.6 points that, contrary to expectations, $\delta\lambda_{geo}$ can not be increased with higher resolution. Ideally the resolution of the spectrograph should be just high enough to resolve the stellar lines. This implies that changing the grating constant d, the spectral order or the grating length requires a fine balance as to minimize $\delta\lambda_{geo}$ without influencing the resolution of the spectrum.

We also see that $\delta\lambda_{geo}$ is proportional to the ratio ϕ_{star} over ϕ_{slit}. The latter can not be diminished at will because a smaller slit width means a higher resolution and it also causes a rise in the light losses. However, by observing stars with large apparent diameters, i.e. increasing ϕ_{star}, we directly amplify the geometrical shift. Moreover, using a bigger telescope would produce the same results.
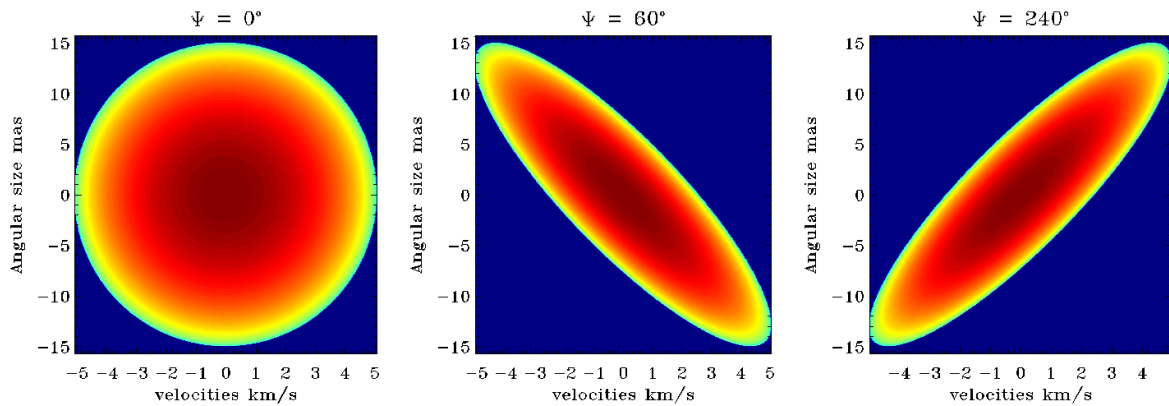

Figure 3.2: Shape of the line broadening function in dependency of ψ. The model assumes a rotational velocity of 5 km/s, an apparent diameter of 15 mas, and a limb-darkening coefficient $\epsilon = 0.6$. The spectrograph parameters, used for the geometrical shift, are a telescope size of 1 m, an incoming angle α of 65°, a standard grating constant, and an observation in the 100th order.

The intensity distribution can be evaluated without excessive errors by the linear limb darkening law:

$$\frac{I_\nu}{I_o} = 1 - \epsilon + \epsilon\cos\theta \qquad (3.8)$$

where I_o is the intensity at the centre of the stellar disk, ϵ the limb-darkening coefficient, and θ is the angular limb distance defined as: $\cos\theta = \sqrt{R^2 - (X^2 + Y^2)/R}$. The Eddington-Barbier relation states that $\cos\theta = \tau_\nu$ with τ_ν the optical depth. Due to the wavelength dependency of the optical depth, the apparrent stellar diameter increases for increasing wavelengths. For instance the apparent diameter of Aldebaran is of 18.8 mas and 20.2 mas in the B and K band[2] respectively. As a result, observing in the IR would assure the largest stellar diameter, but high resolution infrared spectrographs are scarce[3], and instrumental requirements for IR observations are higher than for the optical. Hence I concentrate on optical considerations.

---

2. Values retrieved from the JMMC Stellar diameter Catalogue of Lafrasse et al. (2010)

3. The list of ground-based high resolution (R > 50 000) IR-spectrographs is relatively short: CRIRES in Paranal which is designed from 0.95 to 5.2 μm with a resolution of 100 000; SOPHIA-EXES (Echellon Cross Echelle Spectrograph) working from 4.5 - 28.3 μm, whereas SOPHIA is an airborn observatory

By rewriting the Equation 3.7 in dependency of X and after insertion in the previous expression, the right term of the linear limb darkening law is then:

$$\frac{I_\nu(X,Y,\psi)}{I_o} = 1 - \epsilon + \epsilon \frac{\sqrt{R_{star}^2 - \left(\left(\frac{\Delta\lambda(X,Y,\psi)-KY}{K'}\right)^2 + Y^2\right)}}{R} \tag{3.9}$$

where K and K' are two constant terms resulting from the reformulation of the Equation 3.7. The intensity distribution is the kernel of the two dimensional broadening function. It is a function of wavelength shift and spatial extension, using the spectrograph's characteristics, the stellar velocity and the angle ψ as input parameters. The shape of this distribution is an ellipse, as illustrated in the Figure 3.2, slanted in dependency of ψ. The tilt ξ of the ellipse is easily calculated with a geometrical relation:

$$\tan\xi = \frac{V_{rot}\sin i\ \lambda\ \sin\psi}{c\ R_{star}} \tag{3.10}$$

According to this equation, the tilt of the ellipse is magnified for fast rotating and small stars. This result may seem in contradiction with the conclusions derived from the Equation 3.7. However, our goal is to increase the detectability of the signal, and I will show in the next section that it is not correlated with the tilt magnification.

3.1.1 Influence of Differential Stellar Rotation

During the demonstration of the two dimensional broadening function, I assumed that the star rotates as a rigid body. However, for convective stars, i.e. solar mass stars whose outer layers are dominated by convective transfer, the equator can rotate faster than the poles. This is the phenomenon of differential rotation. It has been observed for our Sun, thanks to the migration of the sunspots, but recently Ammler-von Eiff & Reiners (2012) could also determined it for other stars ranging from A to F type, including fast and slow rotators, while Weber (2007) demonstrated this effect on various K-giants. The differential rotation is expressed in function of the latitude ϕ:

$$\Omega = \Omega_o\ (1 - \alpha\ \sin^2\phi) \tag{3.11}$$

where Ω_o is the rotation rate at the equator, for $\phi = 0°$, and α is the relative differential rotation parameter. In case of our Sun, this parameter is equal to 0.2. I implemented this relation in the Equation 3.3, by replacing $Y = R_{star}\sin\phi$. The resulting two dimensional profiles are affected by the differential rotation: the shape is no longer a perfect ellipse. Yet the tilt of the profile is still present and shows the same inclination than for a rigid body, see Figure 3.3. Consequently differential rotation will not compromise the detection of the signal, since the profile inclination remains identical to that of a rigid body.

3.1.2 Influence of Resolution Limits

The direct detection of the rotational profile requires simultaneously a high spatial and a high spectral resolution. The observed spectrum is the result of the convolution of the intrinsic spectrum and the different additional profiles, e.g. Doppler broadening profile $D(X,Y,\psi,\lambda)$, seeing profile $S(X,Y)$ and instrumental profile IP:

$$I_{obs} = \left\{\left[I_{int}(\lambda) \otimes D(X,Y,\psi,\lambda)\right] \otimes S(X,Y)\right\} \otimes IP \tag{3.12}$$

The four functions vary on different timescales. $D(X,Y,\psi,\lambda)$ is constant on a very long timescale [4]. $I_{int}(\lambda)$ is supposedly constant on long timescales. Even if the star shows some stellar spots, significant changes in the distribution of the stellar disk would only occur after several days. IP, the

---

4. The stellar rotational velocity may decrease over its lifetime. Yet the timescales involved here are in the orders of the million years.
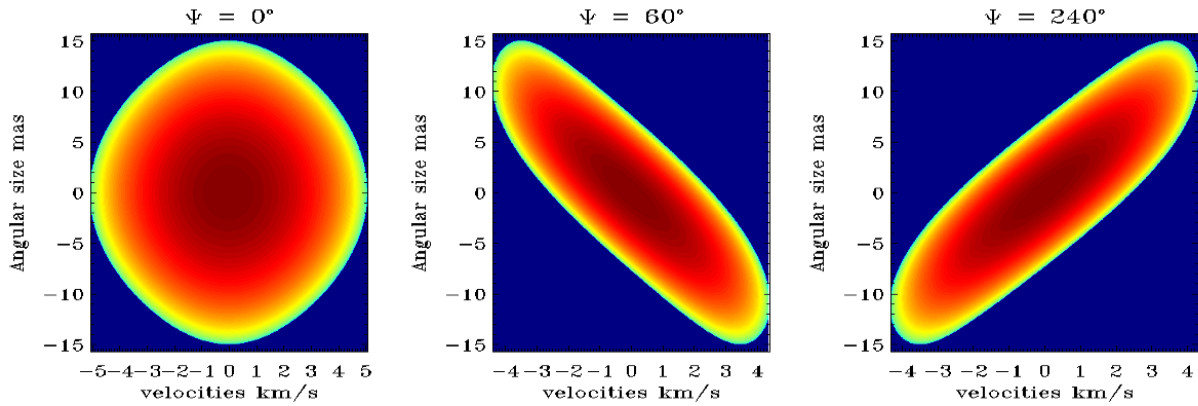
Figure 3.3: Broadening profile for a star presenting differential rotation. The relative differential rotation parameter $\alpha = 0.2$ as for our Sun. The shape of the profile is affected by the variation in the rotation rates and diverges from a perfect ellipse.

instrument profile is considered constant during one observation. The changes in IP are slow and highly dependent on the temperature and the pressure variations. In order to reduce efficiently the influence of these variations on the instrument, the spectrograph can be enclosed by a casing, which is then temperature and pressure controlled [5]. Finally, $S(X, Y)$ is changing at the same timescale as the seeing itself.

The spectral resolution defines how good the observed spectrum shall be resolved on the detector. It should be high enough to resolve the stellar lines. An extremely high resolution, $R > 120000$, would actually deteriorate the signal. Most of the stellar lines for a slow rotating star are already resolved for $R \sim 60000$, meaning that the line is already sampled on 2.2 or more pixels. A higher resolution implies that the stellar line will be sampled by more pixels, which add more pixel noise [6] in the line. Hence, instead of gaining a better knowledge of the line profile, the higher resolution would produce the inverse.

Seeing acts as blurring function over the spectrum: the stellar disk is extended from the few milli-arcseconds of the diffraction limited case to a few arcseconds for a given spectral resolution, which causes a decrease in the profile inclination. Consequently the spatial resolution is seeing limited. It is set through a fine interplay between seeing and plate scale. Since all ground-based spectrographs are faced to seeing, they are designed to sample exactly the seeing disk. For instance, a star, seen through an average seeing of 1″would then be sampled on 2 pixels on the detector. Hence the plate scale of the spectrograph would be 0.5 ″/pix. Here my goal is to detect a signal which scales with the stellar diameter, i.e. a few milli-arcsecond. The smaller the plate scale, the more sub-pixels — one sub-pixel is a small fraction of a pixel — will sample the signal. However reducing the plate scale with constant seeing leads to a spreading of the width of the spectral order, which in turn produces a degradation of the associated errors, see Equation 2.19. Therefore, the detection capability is correlated to the seeing on site or the performance of the adaptive optic system which may be implemented there, and to the plate scale of the spectrograph. Furthermore a lower limit to the detection capability is given by the fact that detecting a signal sampled on less than 1% of a pixel is highly compromised by the inhomogeneities of the detector. Thus, the worst plate scale, and it's corresponding seeing, is estimated by supposing that Betelgeuse (50 mas) is sampled on exactly 0.01 pixel. The resulting value, 5″/pix, would imply an average seeing of nearly 10″, which would

---

5. A whole generation of spectrographs were therefore build in separate rooms, which were pressure and temperature controlled. The light is then fed to the instrument through a fibre. Since our method is incompatible with fibres, I need to keep in mind that instrumental effects may arise during the observations, if the spectrograph is exposed to the variations mentioned before.

6. Pixel noise is: read-out-noise (RON), dark noise for long exposures, background photon noise, stellar photon noise, pixel irregularities, ...

prohibit any kind of observations. Consequently, the ability to detect the signal is not limited directly by seeing, or stellar size.

3.2 Detection of Stellar Spin Orientation Signature

The signature of the orientation of the stellar spin axis is detectable either in the intensity spectrum, obtained by collapsing the spectrum along the spatial direction[7] and resumed below; or in the position spectrum extracted with an spectro-astrometric reduction as described in the section 2.3.2.

3.2.1 One Dimensional Spectrum

Since the intrinsic spectrum of the star is supposedly constant, only the broadening function contains the information of the stellar spin orientation. Its influence on the intensity spectrum is pictured by collapsing the two dimensional broadening function in the dispersion direction to a one-dimensional profile. The result reproduces accurately the broadening function as derived by Gray. In addition, the width of the profile presents a slight dependence with the angle ψ. As illustrated in the Figure 3.4a, the width is maximized for $\psi = 0°$, i.e. when the stellar spin axis is perfectly collinear with the slit spatial axis, and conversely, it is minimized for $\psi = 180°$. In addition, the importance of the geometrical shift, $\delta\lambda_{geo}$, is emphasized on the Figure 3.4b. Indeed, without the geometrical term, the broadening profile barely shows a change in width for any orientation. After convolution of the one-dimensional intrinsic profile with the one-dimensional broadening profile, the stellar lines exhibit a width variation with ψ. Therefore, a standard observation strategy requires to observe the star under several orientations in order to follow these changes in the width of the line profile.
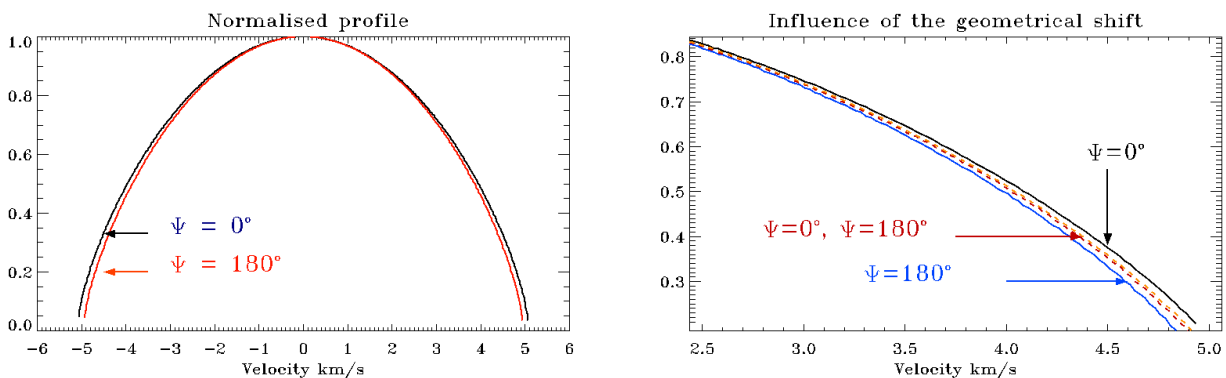
(a) Width variation for the orientations $0°$ and $180°$ for a rotational velocity of 5 km/s. The width difference between the profiles of the anti-parallel orientations is around 100m/s.

(b) In straight lines, the broadening function for the orientation $\psi = 0°$ and $180°$. In dotted lines, the broadening function without the geometrical shift, for the same orientation.

Figure 3.4: One dimensional broadening profiles, for a rotational velocity of 5 km/s, and a limb-darkening coefficient $\epsilon = 0.6$. *Left*: A global broadening profile. *Right*: A portion of the broadening profile, demonstrating the influence of the geometrical shift.

The determination of the orientation of the stellar spin requires to recover the orientation where the lines are the narrowest, and reciprocally the largest. Hence, the method needs an accurate and precise estimation of the line width for each orientation, for comparing them to each other. The precision of the measurement, i.e. how good the width of the line can be measured, is given by the relation:

$$\delta W = \frac{W}{\text{SNR}\sqrt{N_{lines}}} \tag{3.13}$$

---

7. G. Wiedemann, private communication

This relation is obtained with the same reasoning as the Equation 2.19, but instead of considering the position of the order, I focus on the width of an absorption line. This relation demonstrates that stars with narrow lines are better candidates due to their small resulting errors, than stars with shallow lines. Consequently, the errors in the measurements of the width could be reduced to less than a percent of a pixel, assuming high signal to noise in the spectrum and by accumulating several lines. Yet the accuracy of the measure is highly influenced by the seeing during the observations. Due to the fast changes in the seeing profile, the width of the line varies already by a significant amount between two consecutive observations with the same orientation. An accurate measurement therefore requires a correction of the seeing, which usually also takes into account the variations in the instrument profile.

The seeing contribution is evaluated by using lines with known characteristics. The use of stellar lines is compromised, since they also hold the information of the broadening function. In addition, except for a handful of stars, their spectra is not known with a resolution high enough for this application. The telluric lines were, for a time, considered as reference, but they are also fluctuating with the atmospheric conditions and do not permit the required precision in the profile. Hence, the determination of the seeing profile requires the use of an additional absorbing source, a reference gas cell, whose spectrum is well determined [8]. Usually, the reference is made with an iodine gas cell, which provides many additional absorption lines in the visible. The cell itself is closed, and temperature stabilized, to ensure a high stability in the line profile. This profile is then only affected by the instrument and the seeing [9]. Therefore, the seeing profile is retrieved from an iterative process by convolving the intrinsic iodine profile with the unknown seeing function, and comparing the result with the observed iodine profile. Then, the deconvolution takes place. Mathematically it is expressed as:

$$I_{obs} = I_{source} \otimes S \Rightarrow I_{source} = I_{obs} \otimes S^{-1} \tag{3.14}$$

In practice, the exact determination of the seeing profile is fastidious, and compromised by the noise present in the observed data, and line blendings. Yet, this method has been proven successful by the many planet-hunters who use it to detect exo-planets with the radial velocity method. In fact, they can detect position shift down to 1 m/s. However, our gola is to track the evolutions of stellar line widths, instead of following position shifts. The width determination which is highly affected by the deconvolution process, and requires unblended lines.

To summarise, the signal of the orientation of the stellar spin axis is located in the width of the stellar lines. In order to measure them accurately, one would need to deconvolve the spectrum from the seeing profile. Since the widths variations are very small and are easily influenced, the seeing profile needs to be determined as accurately as possible. Finally, the extraction of the one-dimensional spectrum is correlated with an inevitable loss of information, which may make the detection of the signal harder. Therefore, I preferred to concentrate on the two-dimensional spectra, by using the spectro-astrometric method.

3.2.2 Spectro-Astrometric Signature

Contrary to the one-dimensional case, where the rotation signal is dominated by the geometrical shift, the two-dimensional signal is bound to the tilt of the broadening function. Through the convolution of the intrinsic stellar spectrum with the rotational broadening function, the tilt information is transmitted to all the stellar lines of the observed spectrum. Thus, the lines are tilted by an angle ξ related to $\Delta\lambda$ and $\sin\psi$ as demonstrated in the equation 3.10. The absolute position angle of the star is retrieved by monitoring the variations of the line tilt in dependency of $\sin\psi$. The Figure 3.5 illustrates the shape of the two-dimensional spectrum around one line for two anti-parallel orientations. Similarly to the broadening function, the inclination of the line switches direction for $\psi \geq 180°$. The

---

8. The spectrum of the gas cell is measured with a Fourier Transform Spectrometer (FTS), which delivers spectra with a resolution around 500 000.

9. Both iodine and stellar spectrum are recorded simultaneously. As a result, the iodine lines are often blended with stellar lines which complicates the extraction of the one dimensional seeing profile.
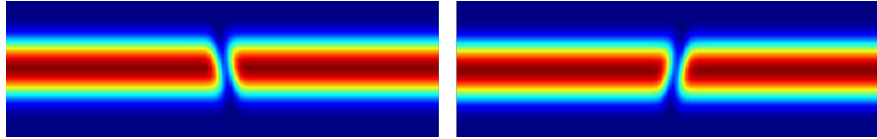
Figure 3.5: Two simulated lines of identical width and depth, as would be seen under two anti-parallel orientations. *Left*: for $\psi = 90°$; *Right*: for $\psi = -90°$. The tilts are exaggerated here for clarity.

signature representing the line tilt is extracted by calculating the centroid of the order for each wavelength pixel. The resulting spectrum, hereafter called position spectrum in opposition to the intensity spectrum, is constant along the continuum, and diverges only in the proximity of an absorption line. Similarly to the line tilt itself, its signature is reversed when $\psi \geq 180°$.
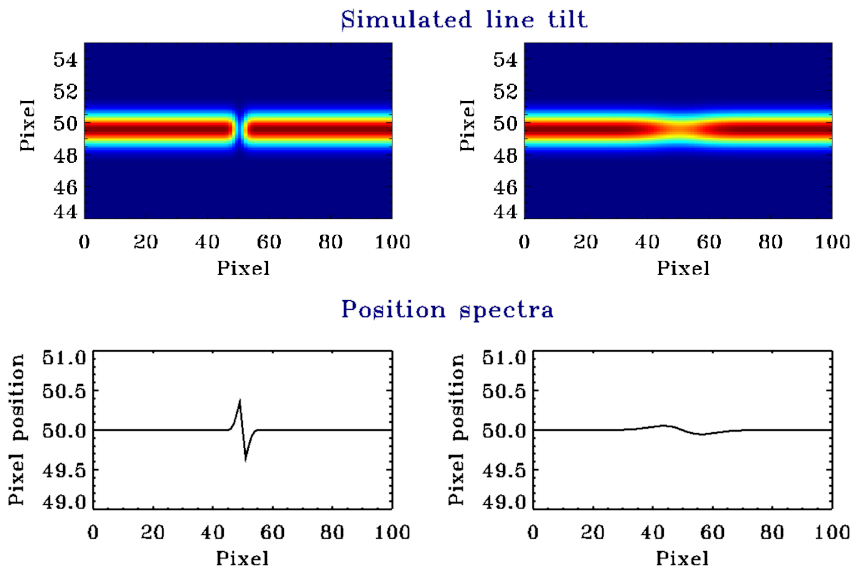
Figure 3.6: Line tilt signatures under the influence of the stellar rotation rates. A simulated absorption line tilted by 2 pixels, *Left*: for a slow rotator. The corresponding line tilt signature is very sharp and easily detectable. *Right*: for a fast rotator. The signal is very shallow which makes it harder to detect. The tilt is exaggerated here for understanding purpose.

It is tempting to associate the tilt angle of the line with the amplitude of the spectro-astrometric signal. Indeed, since the position spectrum translates the inclination of the line in pixel displacement, a higher tilt would generate a higher displacement. However, the tilt is caused by the rotational velocity of the star. Hence an increase of the tilt angle also equates to an increase in the line width. To illustrate this phenomenon, I simulated a two dimensional profile for an absorption line, which is convolved once with the broadening profile of a slow rotating star (V_{rot} = 5 km/s), and once with the profile of a fast rotator ($V_{rot} \geq 25$ km/s). The profiles are reproduced in the Figure 3.6. For the slow rotator, the signal of the line tilt is sharp, while it is shallow and of lower amplitude for the fast rotator. Thus, the detectability of the line tilt is enhanced for deep and narrow lines, which contradict the assumption that fast rotating stars make good observation targets.

Another common misconception is that the presence of stellar spots would deteriorate the signal and hence only inactive stars could be observed. Let us then consider the case of a star with one stellar spot located randomly on its surface. The resulting stellar spectrum has 2 components: one describing the homogeneous stellar disk, and one describing the stellar spot. Since the temperature of the spot and the temperature of the stellar disk are not identical, the spot is usually cooler than the chromosphere, they do not have identical chemical compositions, which results in an absorption at different wavelength. At an absorbing wavelength of the stellar spot, the photocenter of the spectrum

is slightly shifted in a direction opposite to that of the spot. For instance, if the spot is located along the slit axis at the upper edge of the star, then at the absorbing wavelength of the spot, less light arrives from the spot, and the photocenter of the spectrum at this wavelength is shifted toward the lower edge of the star. An exact description of the signal of a stellar spot was made by Voigt & Wiedemann (2009). If the star has N spots, then it would be described by $(N + 1)$ spectral components, each generating a deviation of the photocenter from the continuum. However, this does not affect our reasoning, since these deviations would only occur for a finite number of lines, while the stellar rotation affects all the lines equivalently. Thus, the detection of the stellar spin orientation is not limited by the stellar activity. These considerations shed light on the type of stars which optimize the signal detection. Giants and super giant stars of spectral type G to M combine the large number of absorption lines required, the apparent diameter and the slow rotation, or close nearby stars like Procyon. In case of giants, a special attention has to be made during the target selection as to choose stars without important line broadening caused by micro- and macro-turbulences.

I described before how the signature of the stellar rotation appears with a spectro-astrometric reduction in an ideal case without atmospheric perturbations. However, seeing affects the two dimensional profile of the spectrum. Firstly it extends the profile in the spatial direction. The intensity distribution is smeared over the seeing disk, causing a reduction of the signal's amplitude when passing from a diffraction limited configuration to a seeing limited one. If the star already fills the slit of the spectrograph — meaning an increase of the seeing disk caused by a degradation of the weather conditions — then seeing enlarges the star on the slit, causing a geometrical shift unrelated with the rotational broadening and a consequent line broadening. In order to keep the high resolution of the spectrograph, it is necessary to adjust the slit width. Therefore, an non-negligible amount of light is lost at the entrance of the slit, because the projected stellar image is usually larger than the slit width.

To illustrate the effects of seeing on a stellar spectrum, I simulated a synthetic two-dimensional spectrum as one would obtain from an observation. The intrinsic one-dimensional stellar template is obtained with the PHOENIX code from Hauschildt & Baron (2005) under the assumption of thermal equilibrium in the outer layers of the star for an effective temperature of 4000 K, a surface gravity $\log(g) = 1.8$ and solar-like metallicity. The spectrum is then extended homogeneously in spatial direction, since we saw that the presence of spots does not limit the detection of the line tilt, to a two-dimensional profile. The synthetic star has a diameter of 15 mas, which is sampled on 5 imaginary pixels, and a rotational velocity of 5 km/s. Of course, this is only for computational purpose, since there is no instrument available capable of resolving any star outside our solar system. The two-dimensional stellar spectrum is then convolved with the corresponding rotational broadening profile, and finally with a seeing function defined in the (λ, y) space, corresponding to a seeing disk and a slit width of $1''$. At last, the resulting profile is rebined to a typical field of view of $0.2''$/pixel, i.e. the order is spread over around 10 pixels.

Figure 3.7 illustrates the evolution of the spectro-astrometric signal with the addition of a seeing contribution and at last of photon noise. The seeing is evaluated here with a width of one arcsec. According to this model, a typical signal amplitude for the stellar rotation is around 1% of a pixel. This value is dependent on the spectrograph characteristics and the seeing during the observation. Finally, the presence of noise degrades drastically the signal quality. Up to now, the signal could be identified directly on the position spectrum. However, with the addition of noise, using methods to detect faint signals are appropriate.

The stellar position angle is retrieved by monitoring the amplitude variations of the signal with ψ. As pointed in Equation 3.10, the tilt is directly correlated with

$$\boxed{\sin \psi = \sin(\mathrm{PA}_{slit} + \mathrm{SPA})} \tag{3.15}$$

where PA_{slit} is the projected position angle of the slit defined in the North-East plane, which should be known by the observer, and SPA is the stellar absolute position angle. Thus, I need to extract the amplitude variations of the signal with PA_{slit}, and fit them with a sine curve to obtain SPA.
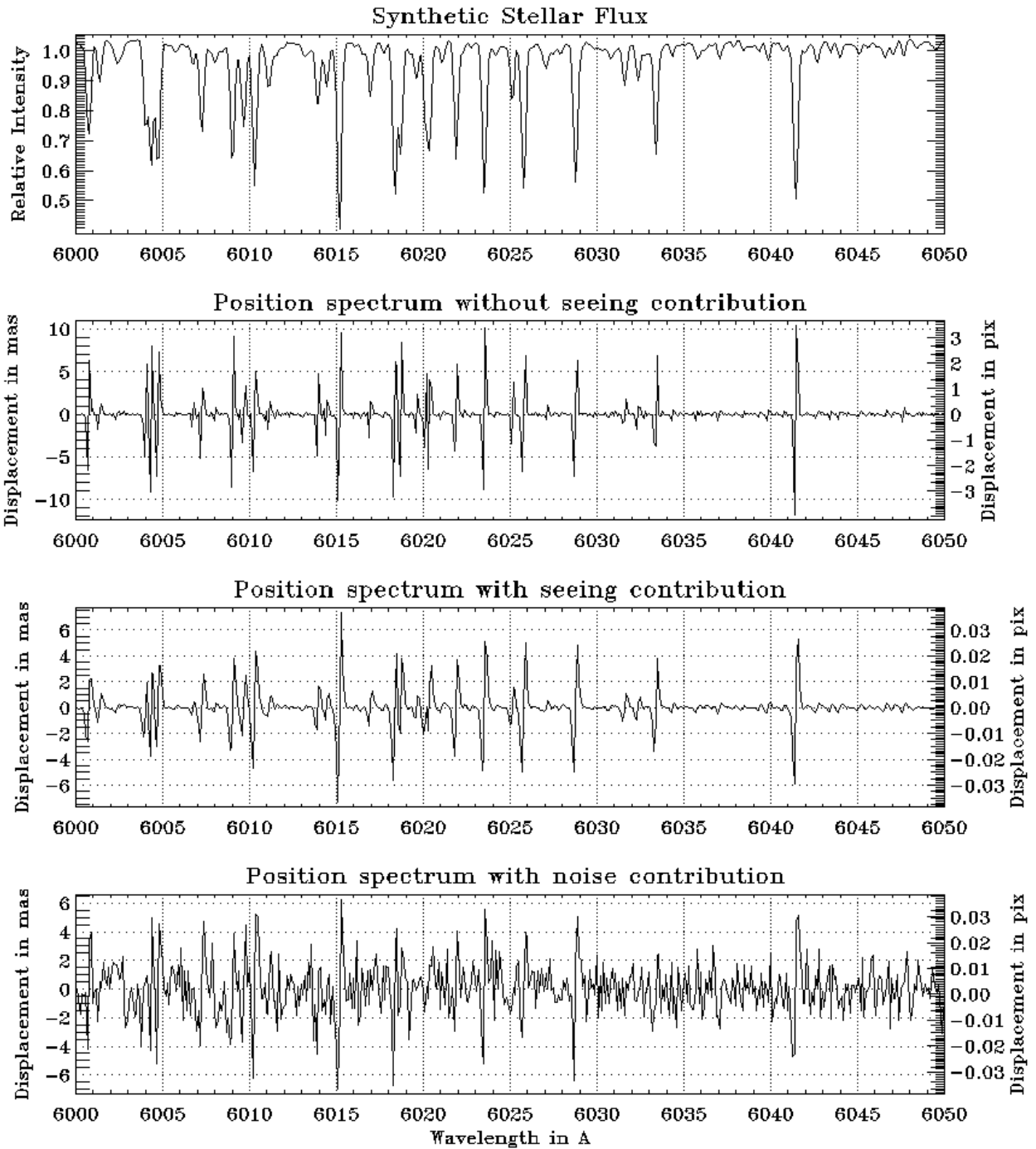
Figure 3.7: Influence of seeing in the shape and amplitude of the spectro-astrometric signal. *On top*: the simulated spectrum calculated with PHOENIX at an average resolution of 61 000 at this wavelength range. *Second from top*: the position spectrum of the star if it could be resolved on 5 pixels with a plate scale of 3 mas/pix. *Third from top*: the correspondingly position spectrum with a seeing of 1. arcsec. The amplitude of the signal is smaller than the size of the star. *On the bottom*: The same position spectrum but accounting for photon noise. The small lines are now barely identified. The amplitude of the signal is dependent of $\sin\psi = \sin(\mathrm{PA}_{slit} + \mathrm{SPA})$, where PA_{slit} is the projected position angle of the slit and SPA is the stellar absolute position angle.

3.2.3 Extraction of the Signal

The stellar position angle is determined by monitoring the amplitude variations of the signal in the position spectrum. When the spectro-astrometric signal is almost hidden by the noise of the position spectrum , it is necessary to consider a maximum of lines together to retrieve the signal. Cross-correlation is a analysis method which compares the correlation between the two available samples, here the position spectrum and the intensity spectrum. Cross-correlation analyses have regularly been used by planet hunters to track the positional shift between two intensity spectra which would reveal the presence of a planet.

The position spectrum is closely correlated to the intensity spectrum: a signal only occurs at the position of absorption lines. Furthermore, the shape of the rotation signature in the position spectrum, see Figure 3.7, is very similar to the derivative of the intensity spectrum at this position. Hence the cross-correlation analysis is done between the derivative of the intensity spectrum and the position spectrum [10].

For these two populations, called here X and Y, composed of N independent elements x_i and y_i, the cross-correlation function between X and Y is:

$$C_{XY} = \frac{c_{xy}}{\sqrt{\sigma_x{}^2 \times \sigma_y{}^2}} \tag{3.16}$$

where σ_x^2 and σ_y^2 are the variances of X and Y obtained respectively with $\sigma_x^2 = \sum_{j=0}^{j=N-1}(x_j - \bar{x})^2/N$, and

$$c_{XY} = \frac{1}{N} \sum_{j=0}^{N-1}(x_j - \bar{x})(y_j - \bar{y}) \tag{3.17}$$

If each population has a set of measured errors δ_x and δ_y associated to each sample, then according to Edelson & Krolik (1988) the expression is reformulated as:

$$C_{XY} = \frac{c_{xy}}{\sqrt{(\sigma_x{}^2 - \sigma_{\delta x}^2) \times (\sigma_y - \sigma_{\delta y}^2)^2}} \tag{3.18}$$

The errors in the cross-correlation function are evaluated using the maximum likelihood approach described by Zucker (2003) which relies on the height of the correlation peak:

$$\sigma_{C_{XY}} = -\left\{ N\frac{C_{XY}''}{C_{XY}} \times \frac{C_{XY}^2}{1 - C_{XY}^2} \right\}^{-1} \tag{3.19}$$

This expression is valid in particular for lags maximizing the cross-correlation functions. Elsewhere, the errors become extremely high, which also translates a very poor correlation. Another approach to evaluate the errors in the cross-correlation function is to take the standard deviation of a set of functions for identical or nearly identical slit angles. This method permits a good estimate of the errors, even when the maximum of the cross-correlation function is moderate. However, it requires that several spectra are taken for each slit orientation .

Since both spectra have same wavelength calibration, the peak in the cross-correlation function should occur around the zero lag position. In practice, due to the definition of the DERIV.PRO procedure of IDL used here, the maximum position can be shifted by one pixel. The points are fitted using a least square reduction with a sine curve of the form $A\sin(\text{PA}_{\text{slit}} + B)$ where the stellar position angle is the negative of the phase, -B, as depicted in Figure 3.9.
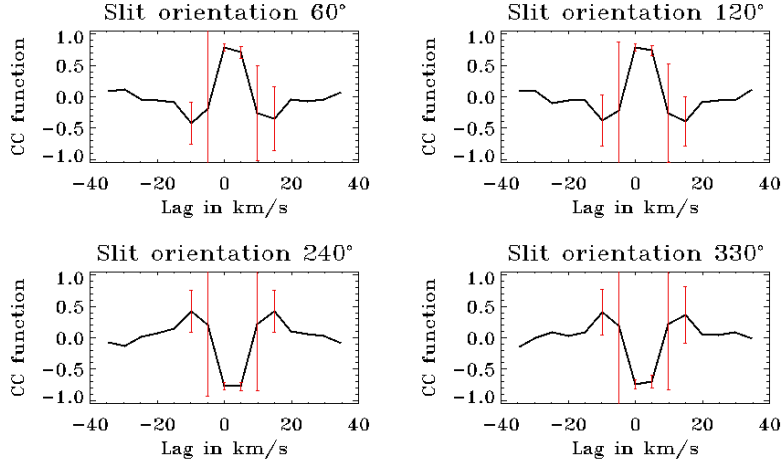
---

10. G. Wiedemann, private communication

Figure 3.8: Cross-correlation functions for 4 slit angles. The errors are correctly evaluated on the peak position but are highly dependent of the value of the cross-correlation function. After the inversion of line tilt, the signal is negatively correlated with the intensity spectrum.
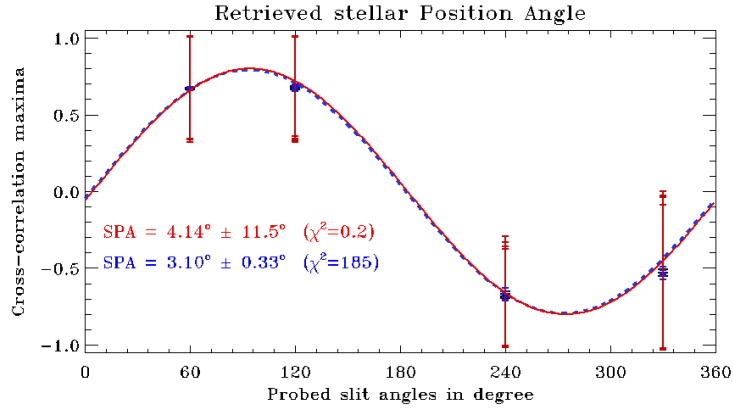

Figure 3.9: Extraction of the stellar position angle using the maxima of the cross-correlation functions. The simulation's inputs are a template spectrum, a field of view for the spectrograph of 0.2 ″/pix and a resolution of 61 000. The error bars are calculated once from the equation 3.19, red error bars, and once from the points dispersion, blue error bars. The points are fitted using a least square reduction with a sine curve of the form: $A \sin(\psi + B)$ where A and B are unknown. Both cases yield identical Stellar Position Angle (SPA) within the errors.

The extraction method was tested on hand of the simulated data described previously which are recalculated four times per orientation in order to compare the two methods for the estimation of the cross-correlation errors mentioned earlier. The cross-correlation function is calculated from the position spectrum and the derivative of the intensity spectrum for a lag of ± 40 km/s. The maxima are plotted versus the slit orientation angle ψ. The input SPA is $0°$. The errors in the maxima are calculated once from the equation 3.19, and once from the dispersion of the points per orientation. Figure 3.9 shows that the retrieved position angle is overestimated by around $4°$ for both error cases. The errors in the determination of the stellar position angle are important judging from the values displayed in the Figure 3.9. The simulation was run a hundred times to check the consistency of these values, and the retrieved stellar position angle presented an average offset from the input value of around $+4.80° \pm 0.56°$. I verified if this value was reproduced when the quality of the position spectrum was reduced. The simulation was run again, but with a field of view of $0.5''$/pixel, which caused a degradation of the position spectrum. Noise and seeing level remained constant. The offset

in the determination of the stellar position angle remains in the same orders of magnitude $4.9° \pm 4.04°$. This effect, should it appear again in the observation data, would produce a systematic error in the retrieved position angle. A larger discussion about the error calculation in the cross-correlation function and of this simulation is proposed in the Appendix A.1.

3.3 Identification of Perturbation Sources

Since the signal amplitude is so low, any external source of perturbation creates potential stronger signals in the position spectrum and can be mistaken as false-positive. I have listed two main contributors, whose signature is confoundingly similar to the signal of the stellar rotation.

3.3.1 Instrumental Astigmatism

Astigmatism in the spectrograph may be caused by a wrong alignment of the collimator or camera optics toward each other. It inclines the image of the slit on the detector. Since every wavelength element is an image of the slit, this inclination is present in all the lines of the spectrum, stellar lines as well as atmospheric lines. With the spectro-astrometric extraction, this causes a signal in the position spectrum of identical shape as the stellar rotation. Furthermore, the amplitude of this signal is correlated with the degree of astigmatism present in the spectrograph, and may not even have been detected previously [11]

However, effects caused by the instrument remains constant during an observing run. Consequently, two observations at anti-parallel orientation record the same instrumental signal, and inverted stellar signal. Then the contribution of the instrument can be cancelled out by subtracting the position spectra taken at anti-parallel orientations.

3.3.2 Seeing Variation

The shape of the seeing function is variable is space and in time. The spatial variation generates signals in the position spectrum which are similar in profile to the stellar rotation signal. Their amplitude is often more important than the researched signal itself, but are intrinsically fluctuating. An example is given in the Figure 3.10, which compares the position spectrum of a B type star without stellar lines, with a K type stars, taken with the UVES instrument at the VLT [12]. The lines seen in the spectrum of α Pavonis are telluric absorption lines. There are also present in the spectrum of Aldebaran, along with stellar lines. However, its position spectrum is overwhelmed with the signal of the telluric lines. Despite the very good seeing at the observation site (that night the seeing was evaluated around 0.8 arcsec), I notice that the seeing signal dominates drastically the position spectrum.

The temporal variation prevents a precise anti-parallel subtraction. Indeed, as long as the spectra are taken consecutively, they record different seeing, causing for instance variations in the signal amplitude or positional shifts. The subtraction becomes then less efficient, and does not remove the seeing component from the position spectrum. Extracting the true signal would require an accurate correction for the seeing component for each observation.

3.3.3 Toward Simultaneous Observations

Consequently, due to the small scale of the spectro-astrometric signal, and the important influence of the seeing in the position spectrum, it becomes necessary to compare position spectra of anti-parallel orientation recorded simultaneously. Then they would have seen the same seeing, whose contribution should be cancelled out during the anti-parallel subtraction, leaving only the stellar contribution. In addition, proceeding to this subtraction enhance the signal and reduces the errors, an

---

11. For instance the ISAAC spectrograph of ESO had strong astigmatism effects, which weren't identified until the spectrograph was used for spectro-astrometry on the star HD75289 during the program 65.L-0133(A).
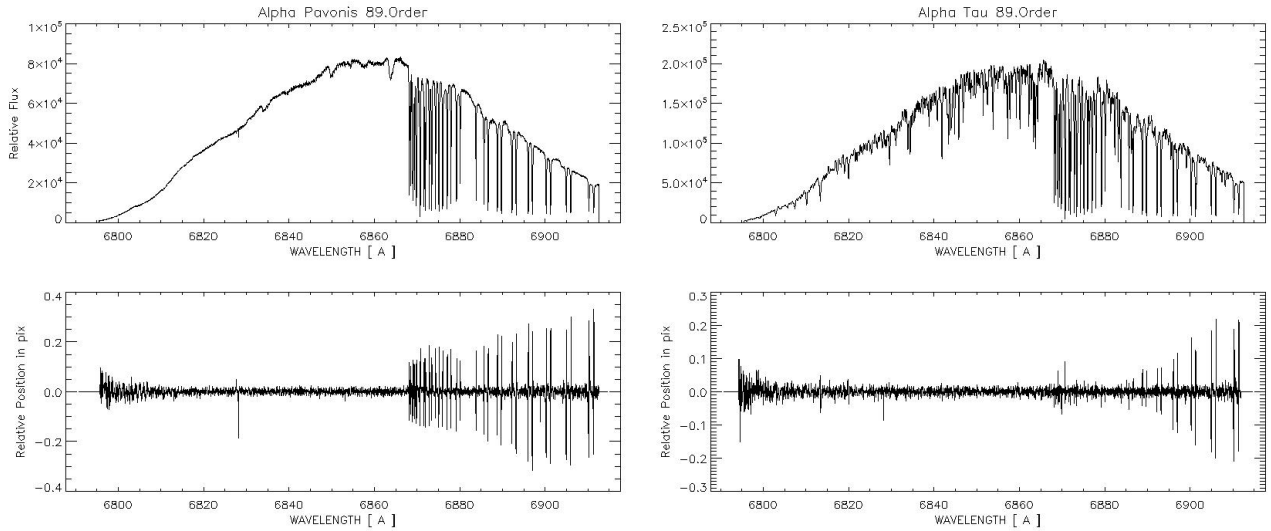
12. ESO program number 073.D-0424(A), taken in 2004

Figure 3.10: *Left*: the intensity and position spectra of the B star α Pavonis. *Right*: the corresponding spectra for the K star Aldebaran. The absorption lines present in the intensity spectrum of the B star are atmospheric lines. They generate a strong signal in the position spectrum.

approach all the more valid when both orientation have identical seeing contribution. Finally, a simultaneous recording of two different orientation would reduce tremedious the amout of observing time required to constrain the stellar position angle.

There are currently no existing instrument capable of doubling and rotating the target before reaching the slit. However, there is a large number of high resolution spectrographs available on middle to large sized telescopes, thus removing the need of the design and construction of another spectrograph. As a result, only the instrumentation required for imaging the two orientations of the star on the slit needs to be developed and tested before an implementation on an existing high resolution spectrograph. The instrument shall be called DeSSpOt for **D**ifferential imag**e** rotator for **S**tellar **S**pin **O**rien**t**ation.

Chapter 4

DeSSpOt

DeSSpOt , the **D**ifferential imag**e** rotator for **S**tellar **Sp**in **O**rien**t**ation, is an instrument to be used together with a high resolution spectrograph and a telescope. It shall enable the acquisition of spectra of two different — ideally anti-parallel — orientations of the star on the detector simultaneously in order to determine the orientation of the stellar spin axis. DeSSpOt was originally thought to be used on one of the high resolution spectrographs of the Very Large Telescopes (VLT). Yet the instrument has to be tested for validity and functionality before being given any chance to be mounted on this facility.

This chapter deals with the conception, construction and tests of DeSSpOt before an use on the telescope. The numerical applications and examples are mostly done for the Coudé spectrograph of the 2m telescope of the Thüringer Landessternwarte Tautenburg, hereafter the TLS-Spectrograph, where DeSSpOt was tested.

4.1   Instrumental Requirements

DeSSpOt is designed to be inserted on existing high resolution long slit spectrographs between the telescope output and the slit entrance. This results in a set of constraints on the instrument for a smooth use of both DeSSpOt and spectrograph. These requirements and constraints are identified in three types: they are respectively of geometrical, optical and mechanical nature.

4.1.1   Geometrical Constraints

Existing spectrographs are either directly connected to the telescope via the Nasmyth or Coudé outputs, or fibre fed. However a single fibre does not preserve the spatial information and those spectrographs are discarded for our method. Many high resolution spectrographs are currently used for radial velocity surveys. Hence an important number of optics is already placed before the slit: an iodine cell for the reference, and sometimes in addition, for instance: an atmospheric diffraction corrector (ADC) which compensates for the dispersion of the star due to the atmosphere, a derotator, which corrects the field rotation of the telescope, various filters, a depolariser and at last images slicers [1]. The available place in front of the slit is therefore limited by the already existing optics. Consequently the instrument has to be small for being inserted.

The TLS-spectrograph is constructed at the Coudé output of the telescope. The light is redirected toward the slit with an elliptical fold mirror. An iodine cell is already implemented between the mirror and the slit. It is possible to remove this cell and to replace it with the instrument. Consequently DeSSpOt has to squeeze in an opening of 120 mm along the optical axis of the telescope, 200 mm large and at a height of approximatively 100 mm. The size of the optical elements being dictated by

---

1. This is the configuration of the pre-slit optic of the UVES spectrograph at Paranal. The insertion of any additional optic is therefore critical. However the iodine cell can be easily removed. This sets free a place of 15 x 15 x 7 mm for an alternative instrument (Dekker, H. private communication).

the diameter of the beam at this position, the overall set-up of the instrument has to be very compact in order to be inserted instead of the iodine cell.

4.1.2 Optical Requirements

The instrument has to satisfy a large list of optical requirements to be operational.

– The first is to rotate one of the beam because it is the function of the instrument.
– The second and most obvious, but not necessary the easiest to achieve, is to preserve the optical axis of the telescope. Indeed it ensures that the incoming light reaches both the slit and the collimator of the spectrograph. Hitting the latter guarantees that the exiting beams of DeSSpOt shall go through all the optics of the spectrograph to the detector. Ideally both beam should be equally centred on the collimator.
– The instrument has to conserve the aperture ratio of the incoming beam. The telescope delivers a beam with an aperture given by $F_\# = F_T/D_T$ where F_T is the focal length of the telescope and D_T its primary mirror diameter. The aperture ratio gives the angle of the beam by $\tan a = 1/F_\#$, as defined in Figure 4.1. The beam is focused on the slit and is passed with the same aperture ratio to the spectrograph which is set-up in such a way that all the incoming light is captured by the collimator. If the instrument reduces the aperture ratio, then the angle of the beam becomes greater, and some light is lost around the collimator. If the instrument increases the aperture ratio, then all the light is collected, but a smaller part of the grating is illuminated, resulting in a loss in resolution. As a result the two beams from DeSSpOt should be in the same pupil field to hit equally the grating.
– The optics of DeSSpOt shall not affect the image quality of the spectrum. Since any additional optic introduces some aberration in the wavefront, these should be verify and kept at minimum. Specifically, astigmatism and defocus aberrations should be avoided because they generate false positive signal.
– The optics and the design of the instrument should be chosen in a way that minimized the overall light loses and the sources of stray light inside the instrument.
– The optical path length between the two channels should be of equal length for the star to focus on the slit. In addition, the image of the pupil, i.e. the primary mirror, should still remain on the grating, or close to the grating surface, to ensure low light losses.
– Finally, this is a requirement mainly for the spectrograph, the spectral orders shall not overlap when using DeSSpOt. Indeed, many spectrographs are designed to record a high number of orders on the detector. Hence the gap between two consecutive orders was reduced to a minimum. Those spectrographs would not be suited for our application. However, the separation of the orders is given by the dispersion power of the cross-disperser. Consequently, either the spectrograph has already an order separation sufficiently high to image two spectra next to each other — like the UVES spectrograph — , or the cross-disperser has to be changed for a higher dispersing one. On the other hand, DeSSpOt shall also provide a beam separation big enough, that the beams do not overlap neither on the slit, nor on the detector.

If the spectrograph is not equipped with a built-in beam rotation unit, or natural field rotation, then DeSSpOt should include a rotation unit to probe different slit orientations. In this case, which shall be referred later as the extended DeSSpOt , the optical requirement of this unit are:

– Keep the optical axis under every rotation angle, for the same reasons as before.
– Limit light losses and aberrations.

This version of DeSSpOt was studied for an implementation on the OLT telescope of Hamburg. The rotation unit would be put at the entrance of the instrument, and make use of a Dove prism for the beam rotation.
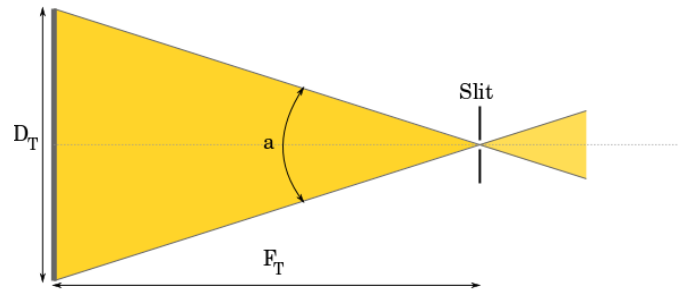
Figure 4.1: Definition of the aperture ratio. D_T is the diameter of the primary mirror, F_T the total focal length of the telescope.

4.1.3   Mechanical Requirements

The optical elements of the instrument are held by mechanical mounts. These are part of the instrument and should therefore be chosen according to the following specifications.

– They are to be small for the instrument to satisfy the geometrical constraint.
– Due to the purpose of DeSSpOt , the instrument should be easily modular for any kind of spectrograph. Consequently the mounts shall be adjustable in order to correct the path of the light beams.
– The mechanical parts should have low thermal dilatation coefficients. Indeed for spectrographs connected to the telescope via the Nasmyth output, the temperature variations should also be considered. The optical and mechanical parts should not dilate to much during an observation night, so the optical properties of the instrument remains near to constant during this time lapse.
– In addition to being adjustable, the mounts should also be stable enough so the vibrations of the telescope, and possible up-side-down positions, are not reflected back on the image quality.

For spectrographs connected via the Coudé output, the spectrograph may lie in a separate room or below the telescope. The light is transmitted to the instrument via several fold mirrors which means that the light losses are already important before even reaching the instrument. However, in this case, the temperature and vibrational constraints are less critical on the mounts and on the optics.

The extended DeSSpOt has additional requirements related to the entrance rotation unit. The rotation unit shall enable a change in the stellar orientation, while the basic DeSSpOt layout enable the anti-parallel projection of the star on the slit.

– The rotation should be done mechanically and remotely. Turning the prism manually is not acceptable since the prism may not even be reachable once mounted. Hence a rotation motor would be needed.
– The rotation should be precise and reproducible. The errors in the beam orientation induce additional errors during the analysis of the images.

Since DeSSpOt was mounted on a Coudé spectrograph, the image rotation was supplied by the telescope. Thus, the extended DeSSpOt was not designed any further.

4.2   Concept

The basic concept [2] of DeSSpOt is to image one star at two different orientations simultaneously on the slit. In order to do so, the incoming beam of the telescope shall be divided and directed toward two channels. The beams are rotated by $180°$ to each other in order to produce the anti-parallel orientations, and finally both beams are focused on the slit. Both channels shall follow similar optical path lengths through the instrument, and be in the same pupil field on the slit.

---

2. Proposed by G. Wiedemann, private communication

4.2.1 Separation - Recombination

The separation of the beams can be done either by intensity or by polarisation. Both are performed with beamsplitters. In the former case, 50 % of the light is reflected by the optic while the rest of the light is transmitted through the optic. Consequently, at the recombination, part of the light is lost through the beamsplitter. Hence, additional optics are needed to re-converge this beam toward the slit. This is highly incompatible with the geometrical constraint of the instrument, and consequently this solution was discarded for the design of the instrument.

The polarisation separation splits the beam according to its polarity into two beams linear polarised, with s- and p- polarisation. This separation method has the advantage that no light is lost during the recombination. In addition, since the stellar light is mostly unpolarised[3], the only source of polarisation comes from the many reflections in the telescope mirrors. It could result in slight intensity variations between both orientation on the detector, which as long as they remains small do not affect the detection of the spectro-astrometric signal, but merely the error estimation.

4.2.2 Beam Rotation

Usually the beam rotation unit is realised with 3 to 5 mirrors. This optical assembly has been described by Denisov & Koroleva (1997). It has the advantage that due to the mirrors, the rotation unit is not wavelength dependent, and does not induce any deformation of the wavefront, as long as the mirrors are sufficiently polished. On the other hand, this solution requires a fine adjustment of the mirrors in order to keep the optical axis. Consequently this method requires at least three mirrors and as many adjustable mounts for the beam rotation. This solution compromised dramatically the geometrical requirement and an alternative solution was searched.

Dove prisms, which have an increased use in astronomy, are natural beam rotators. They rotate the image by twice their own rotation angle. They are optimized for collimated beams, but beams with high aperture ratio are also acceptable[4]. Since they are bulk optical elements, the diffraction caused by the material of the prism shall be investigated. In order to keep similar path lengths between both channels, each beam shall pass through a Dove prism. They are rotated respectively by $90°$ and $180°$. The image of an object through the Dove prism is mirrored. This effect does not influence the spin axis determination, because both channels will present this effect.

4.2.3 Optical Layout

The function of DeSSpOt is to image two anti-parallel orientations of the star on the slit. The instrument is built after the optical layout depicted in Figure 4.2. The incoming light from the telescope is separated according to linear polarisation thanks to a polarised beamsplitter cube. Two small right corner prisms are cemented on the output faces of the first beamsplitter. They redirect the light perpendicularly to the output direction. This solution was adopted so the output beam direction is collinear to the input beam direction. Else the output beam direction would have been perpendicular to the input direction. One beam is deviated by $90°$ with an adjustable mirror. Each beam is then sent towards one of the Dove prism, which are rotated respectively by $180°$ and $90°$, in order to keep the identical optical path lengths for both channels. The size of the Dove prisms is kept as small as allowed by the beam diameter. Finally the beams are directed towards the second polarisation beamsplitter for recombination. They focused at last on the slit, one above the other along the spatial direction of the slit.

---

3. The highest polarisation rates are found in pulsars and maser. Yet for supergiant stars of spectral type K and cooler, the polarisation rates seldom exceeds 5%. M-type stars are more prone to show some polarisation that K- and G-type stars. In addition the polarisation is also dependent of the observing wavelength and the distance of the object, since interstellar medium can also show slight polarisation.

4. The design for the OLT, $F_{\#} = 13$, includes two small lenses at the entrance and output of the instrument to collimate and focus the light from the telescope.
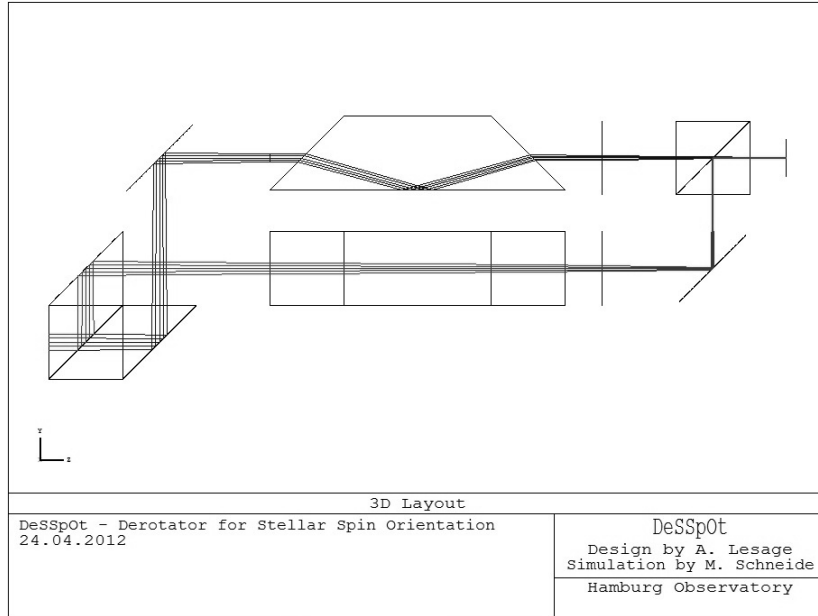
Figure 4.2: Optical layout of DeSSpOt, the light from the telescope is coming from the left with a F/46 aperture ratio, after passing the instrument the beams are focused on the spectrograph's slit. The first beamsplitter separates the light into a s- and a p- polarised beam. The s-polarisation is reflected while the p-polarisation is transmitted. The beam of each channel passes through a Dove prism in order to keep similar optical path lengths. The Dove prisms are rotated by $90°$ and $180°$ respectively.

Material Choise for the Dove Prism

In order to limit the dispersion of the beam by the Dove prism, the material of the prism is chosen accordingly to its Abbe-number [5], or V-number. A high value of V characterises a material which produces low dispersion of the light. Therefore, the ideal material for the Dove prism for our application should have the highest Abbe-number as possible. Fortunately, materials with high V-number also have low divergences in the reflectance of s- and p-polarised ray for incoming angles below $50°$ which will limit the sources of stray light inside the instrument.

Three material candidates were investigated for the Dove prisms: N-BK7, calcium fluorite CaF_2 and Lithium fluorite LiF. The first is popular crown glass, fabricated by SCHOTT, used for manufacturing many prisms including Dove prisms. The other two are crystals which are mostly used for observations the infra-red because of their large bandpass. Their main optical properties are resumed in the Table 4.1.

The length of the Dove prism is dictated by the material refractive index n, the base angle α and the height D of the prism. The relation was demonstrated by Sar-El (1991) and is reproduced here:

$$L = \frac{D}{2\sin(2\alpha)}\left\{1 + \frac{\sqrt{n^2 - \cos^2\alpha} + \sin\alpha}{\sqrt{n^2 - \cos^2\alpha} - \sin\alpha}\right\} \tag{4.1}$$

The relation states that the length of the prism increases linearly with its height D. Moreover, the proportionality factor is bigger for small refractive index as indicated in Figure 4.3. The influence of the base angle is also shown on the Figure 4.3. The shortest length is reached for a base angle of approximatively $30°$ to $35°$ depending on the material of the prism. Yet, small base angles also

---

5. The Abbe-number is an indicator of material dispersion in relation to its refractive index. This number approximates the inverse of the slope of the refractive index vs wavelength. Therefore a high number means that the slope is small, and the refractive index does not vary much with increasing wavelength. On the contrary, a low number implies that the slope is important, and the refractive index of the material changes drastically with the wavelength. By its definition, the Abbe-number is relevant only for applications in the visible.

induce important errors in the beam when taking into account possible manufacturing errors.
The optical path length, i.e. the distance travelled by the light inside the prisms, is calculated from
the relation of Sar-El (1991):

$$T = \frac{nD}{\cos\alpha\{\sqrt{n^2 - \cos^2\alpha} - \sin\alpha\}} \tag{4.2}$$

It is actually shorter than the prism's length, see Table 4.1.

At last, the geometrical requirement prevailed on the material choice. I choose CaF_2 as material
for the Dove prism, seeing as it is a good compromise between length and low internal dispersion.
Furthermore, thanks to its large bandpass, the prisms could also be used for observations in the Infra-
Red. Thus, the Dove prisms were manufactured in CaF_2, with a base height of 10 mm and a base
angle of $45°$. They have no anti-reflection coating, since these coating are not neutral toward polari-
sation.
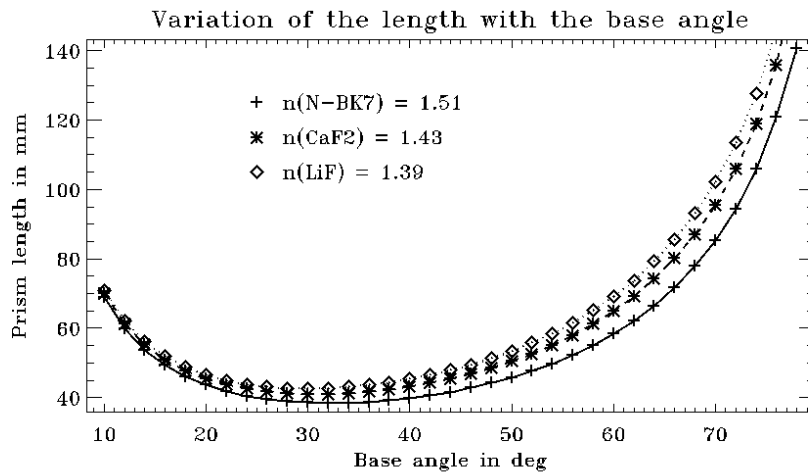
Figure 4.3: Dove prism length variation with the base angle for a base height of 10 mm. The length is
slightly shorter for small refraction index, like those of LiF than for the those of N-BK7. The shortest
length is reached approximatively for a base angle of $35°$. Yet the associated errors rises for lower
base angles see Section 4.3.1

		Materials		
Properties		N-BK7	CaF_2	LiF
Refractive index at $\lambda = 550$ nm		1.5185	1.4348	1.3930
Abbe number V_d		64.17	95.9	97.29
Length (D=10 mm, $\alpha = 45°$)		42.21 mm	46.12 mm	48.68 mm
Optical path length		33.75 mm	37.50 mm	39.97 mm
Transmission (s-polarization)	$0°$	80.03 %	80.86%	80.99%
	$90°$	79.31 %	83.54 %	85.47%

Table 4.1: Properties of Dove prisms in the above materials. The transmission rates are similar for
p-polarised light. They are calculated with the optical analysis programme ZEMAX©.

Choice of the Wavelength Range

The beamsplitters are functional only over a small wavelength range. This is due to the coating
applied on their surface which guarantees the separations of the light into the s- and p-polarisations.

Since the prototype of DeSSpOt is to be tested on a spectrograph designed for the optical, e.g from 350 to 900 nm, I choose to optimize this set-up for a wavelength range of 400 to 750 nm. Indeed, in this range the telluric lines are not too important, and with a shorter total wavelength coverage, I ensure that the polarisation separation is homogeneous on all the orders.

Mirror Mounts

The mirrors themselves shall be with a silver coating, which ensures a optimal reflectance over a large wavelength range. They shall be implemented on mounts which have to remain small despite being adjustable. I choose a compact mirror mount from Thorlabs, whose dimensions are kept small and which provides a correction of the beam in vertical and horizontal directions. The mount is large enough that a hole can be milled in it to hold the mirror if the space requirements become too critical. More over the surface of the mount is anodized. This means that the aluminium at the surface was oxidised to form the Al_2O_3 crystal, which forms a black coating. This reduces the amount of reflections inside the instrument.

Dove Prism Mounts

The Dove prisms should not lie on their internal reflecting surface. A natural contact with the air is needed for the proper reflection of the rays inside the prism. This reflection takes place when the following relation at the surface is true:

$$\frac{n_{inside}}{n_{outside}} \sin i_1 \geq 1. \tag{4.3}$$

where n_{inside} and $n_{outside}$ are the refractive index of the prism and the outside medium respectively, and i_1 the incident angle from the normal of the surface. Further notations are defined in the Figure 4.4. Since the mounts are mostly anodized, let us have a look at the numerical application: $n_{Al_2O_3} = 1.774$ at 500 nm. Hence, if the reflecting surface of the prism lies directly on the mount, the internal reflection is compromised because $n_{CaF_2}/n_{Al_2O_3} \approx 0.8$ at 500 nm. For that reason, the prism resting at $90°$ shall be hold from the top, and the second prism shall rest at $180°$, and been held from the sides.
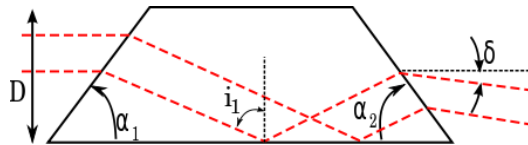
Figure 4.4: Notation adopted on the Dove prism: α is the designed base angle, α_1 and α_2 are the base angles with the possible manufacturing errors, diverging only by a small amount of α: $\alpha_1 = \alpha + \Delta\alpha_1$. i_1 is the internal reflection angle. D is the base height of the prism. δ is a beam deviation caused by the manufacturing errors.

4.3 Tests on the Dove Prisms

The Dove prisms are the key elements of the DeSSpOt instrument. They are investigated numerically and tested separately before insertion in the instrument.

4.3.1 Numerical Analysis of the Dove Prism

The effects of manufacturing errors are investigated here. I analyse the characteristics of the prisms for the three potential materials: N-BK7, CaF_2 and LiF. The angular tolerances given by the manufacturers of the CaF_2 and N-BK7 prisms are of ±3 arcmin for the base angle. They are added

to the base angle under the form: $\alpha_{1-2} = \alpha + \Delta\alpha_{1-2}$. Small divergences in the nominal value of the base angle lead to a vertical beam deviation as illustrated on the Figure 4.4. The corresponding deviation angle δ_V is calculated from the following equation:

$$\delta_V = \alpha + \Delta\alpha_2 - \arccos\left(n \times \sin\left[\Delta\alpha_1 - \Delta\alpha_2 + \arcsin\left(\frac{1}{n}\cos(\alpha + \Delta\alpha_1)\right)\right]\right) \qquad (4.4)$$

The deviation angle varies quasi linearly on the small scale considered. If the angular tolerances are equal for both angles of the prism, then the error is cancelled out, as seen in the Figure 4.5a. On the contrary, if both angles diverge from each other by 6 arcmin the beam deviation is maximized around 5 arcmin. This corresponds to 1 cm shift of the beam on the collimator at the TLS-spectrograph. The value of the angle δ is more important for high Abbe-number material , e.g. LiF, than for low Abbe-number material like N-BK7.

To confirm the choice of the base angle, I also verified how this angular deviation varies with the base angle leading to the shortest prism. The result is given in the Figure 4.5b, where it can be clearly seen, that the smallest base angle also causes the biggest deviation.
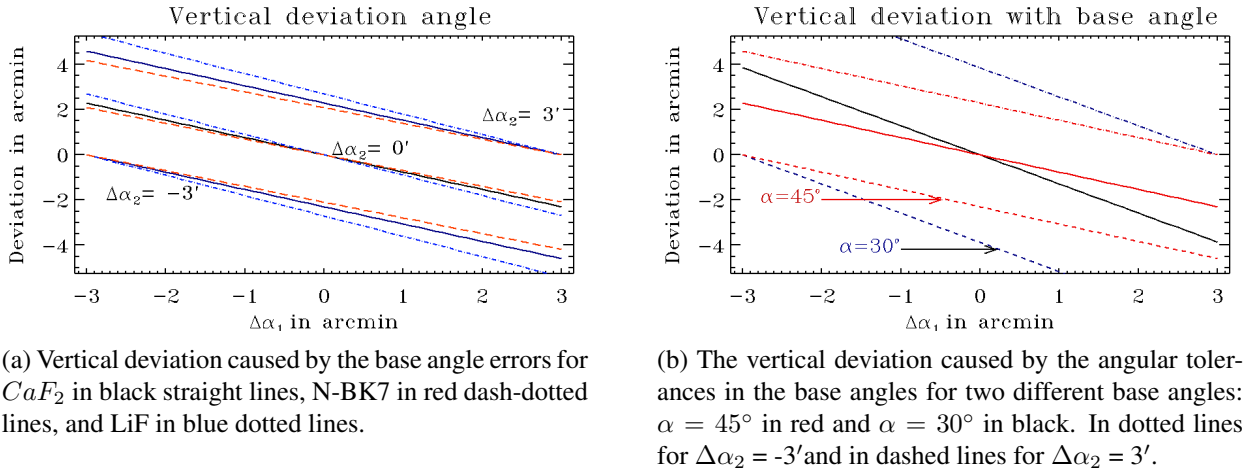
(a) Vertical deviation caused by the base angle errors for CaF_2 in black straight lines, N-BK7 in red dash-dotted lines, and LiF in blue dotted lines.

(b) The vertical deviation caused by the angular tolerances in the base angles for two different base angles: $\alpha = 45°$ in red and $\alpha = 30°$ in black. In dotted lines for $\Delta\alpha_2 = -3'$ and in dashed lines for $\Delta\alpha_2 = 3'$.

Figure 4.5: Deviations caused by errors on the base angles. *Left*: For various materials. *Right*: For various base angles.

Similarly, the reflecting and side plane of the prism are not perfectly orthogonal. This manufacturing error, called pyramidal error, causes a horizontal deviation of the beam. The relation linking the deviation angle δ_H to the pyramidal error angle θ_p was derived by Moreno et al. (2003):

$$\delta_H = 2\theta_p\left(\sqrt{n^2 - \cos^2\alpha} - \sin\alpha\right)\cos\alpha \qquad (4.5)$$

The relation is linear in θ_p and the slope is steeper for LiF than for N-BK7 as pictured in the Figure 4.6. This results confirms the material choise for the Dove prism. The global deviation is then defined by $\delta_{tot}^2 = \delta_V^2 + \delta_H^2$. These values remain small enough to be corrected with adjustable mirrors.

I also investigated the influence of the angular tolerances on the diffraction of the output beam. The diffraction happens along the same direction as the vertical deviation. Therefore, the dispersion angle is calculated from the equation 4.4 by taking into account the wavelength dependency of the refraction index of the material. Furthermore, the study includes the effects of non-collimated beam on the dispersion angle, in particular the following aperture ratios: $F_\# = 46$ as delivered by the telescope into the TLS-Spectrograph, and $F_\# = 13$ as delivered by the Oskar-Lühning Telescope in Hamburg. The investigation was made on the basis of base angle differences, since they induce the diffraction of the output beam. As seen in the Figure 4.7a, the bigger the difference in the base angle, the greater the dispersion angle.
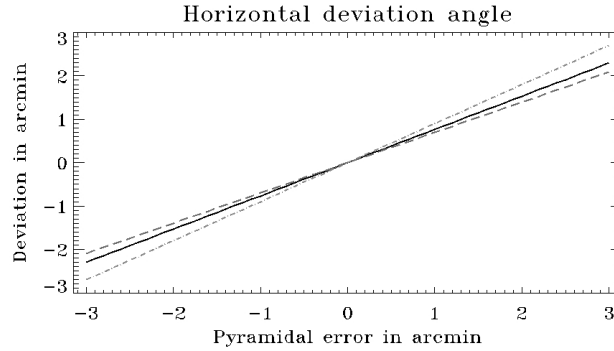
Figure 4.6: Lateral deviation from the pyramidal error for CaF_2 in black straight lines, N-BK7 in dash-dotted lines, and LiF in dotted lines.

I compared these values with the atmospheric diffraction, which occurs for any stars not observed exactly at zenith. This phenomenon is linked to the amount of atmosphere, called airmass, the light has to cross before reaching the telescope. The airmass relation is usually given as : $AM \sim 1/\sin Z_t$ where Z_t is the Zenith angle defined as equal to $0°$ in Zenith and $90°$ at the horizon. The atmospheric refraction angle is calculated for each wavelength from the relation given by Roe (2002):

$$R \approx 206265 \left(\frac{n_{air}^2 - 1}{2\, n_{air}^2} \right) \tan Z_t \quad \text{in arcsec} \qquad (4.6)$$

The computation of the atmospheric refraction index as a function of the wavelength was performed with the Ciddor model developped by Ciddor (1996). This model is up to now still considered as state-in-the-art for applications in astronomy because of its validity over a very large wavelength rage. The model's inputs are the considered wavelength, the temperature, the pressure, the fraction of humidity at the observing site and the concentration of carbon dioxyde. The refraction index is computed for a high humidity ratio (> 65 %), and a average temperature of $0°C$ as it represents reasonably the observation conditions in winter in Germany, and from 350 nm to 850 nm. The resulting dispersion angles are depicted in the Figure 4.7b for increasing zenith angles. These values are in the same order of magnitude than the prism dispersion angle. As a result the prism does not diffraction the light much more than the atmosphere itself.
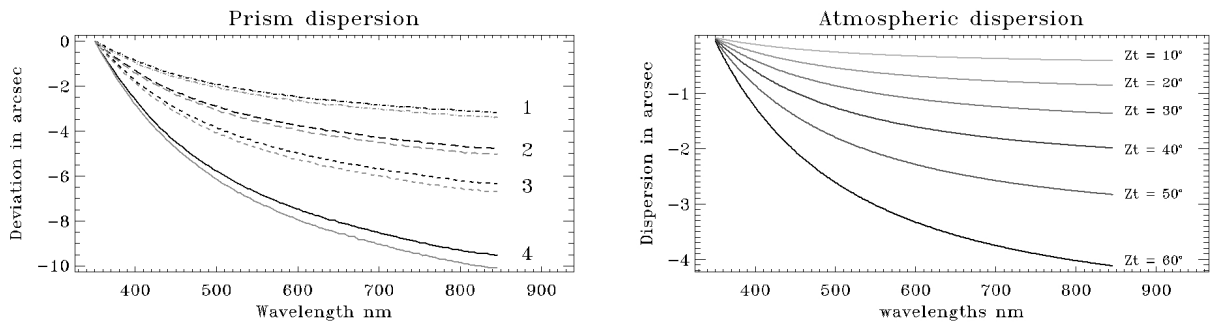
(a) Diffraction by the Dove prisms, for *(1)* a base angle error $\Delta\alpha_1 - \Delta\alpha_2 = 2'$, *(2)* $\Delta\alpha_1 - \Delta\alpha_2 = 3'$, *(3)* $\Delta\alpha_1 - \Delta\alpha_2 = 4'$ and *(4)* $\Delta\alpha_1 - \Delta\alpha_2 = 6'$. In black for $F_\#$ = 46, in grey for $F_\#$ = 13. The diffraction effects are slightly more pronounced in the latter.

(b) Atmospheric diffraction for several Zenith angles Zt. The refraction index is calculated from the Ciddor Model for high humidity fraction (> 65 %).

Figure 4.7: Comparison of the prism dispersion and the atmospheric dispersion. The order of magnitude of both effects are similar.

A beam dispersion along the spatial direction of the slit results in a shift of the position of the continuum in the position spectrum, which is easily identified and corrected, and does not influence

the detection of the signal. On the contrary, a dispersion along the spectral direction leads to small wavelength dependent variations in the incoming angle of the grating, which in turn causes small changes in the wavelength solution of the spectrum. The second effect remains however minimal over one order. The change in the wavelength solution over one order is estimated around 0.07Å and thus, does not influence the resolution in the position spectrum.

4.3.2 Optical Quality

I verified the optical quality of the three ordered Dove prisms manufactured in CaF_2. The goodness of the prisms is quantified by the determination of the Strehl ratio [6] for each part. This is calculated from the measurements of the root-mean-square (rms) of the wavefront with the relation from Mahajan (1991):

$$SR = exp\left\{-(rms_{astig}^2 + rms_{coma}^2)\right\} \tag{4.7}$$

with both rms expressed in wave units. In order to determine the rms of the wavefront after passing the prisms, the test set-up was done in the following configuration:
  – A beam of collimated light is created;
  – The wavefront of the beam is measured with a wavefront sensor in order to set a reference for the wavefront, and remove the possible abberations occuring in the collimation process. This reference wavefront is afterward subtracted from the wavefront measured after the prisms. Each prism is tested in the two orientations $90°$ and $180°$.
  – the reconstructed wavefront is given as a set polynomes with Zernike coefficients, which are used to calculated the rms for astigmatism and coma separately.
  – Finally, these measurements are used to determined the Strehl ratio for each prism.

The results of these measurements are displayed in the Table 4.2. The third prism presented an important discrepancy in the Strehl ratio between the two orientations. An error in the measurement is not excluded. Nonetheless, the prism was marked and set aside not to be used under the $90°$ orientation. In addition, the prisms verified all the Marechal criterion, independently of their orientations. Therefore, they are all of good optical quality for our application.

	Prism 1	Prism 2	Prism 3
rms astigmatism at $90°$ (μm)	0.1675 ± 0.0027	0.1816 ± 0.0024	0.3293 ± 0.0687
rms astigmatism at $180°$ (μm)	0.1984 ± 0.0027	0.2031 ± 0.0024	0.2073 ± 0.0025
Strehl Ratio at $90°$	91.32 %	95.40 %	76.26%
Strehl Ratio at $180°$	91.24 %	89.28 %	93.27%

Table 4.2: Optical quality of the CaF2 prism

These results were confirmed by investigations of the image distortion. I used a small grid-target, centered it in the middle of the beam and imaged it on a CCD detector, of pixel size 5.4μm, for two orientations and the two best prisms. The images were rotated and compared to a reference image. I looked in particular for distortions in the smallest grid section. Figure 4.8 is the close up of the superposition of four images taken with the prisms and the reference image. The resolution is pixel limited, yet the grid is perfectly identified, and there are no visible distortion in the image.

---

6. The Strehl ratio is a measure of the optical quality of an imaging instrument. It ranges from 0 to 1, but can be expressed in percents. A Strehl ratio of 1 represents a perfect, non existing, optical system, while a value of close to 0 represents a high distortive system. It derives from the Marechal criterion which stipulates that the optical properties of a system are good if its rms satisfies the relation $rms \leq \lambda/14$.
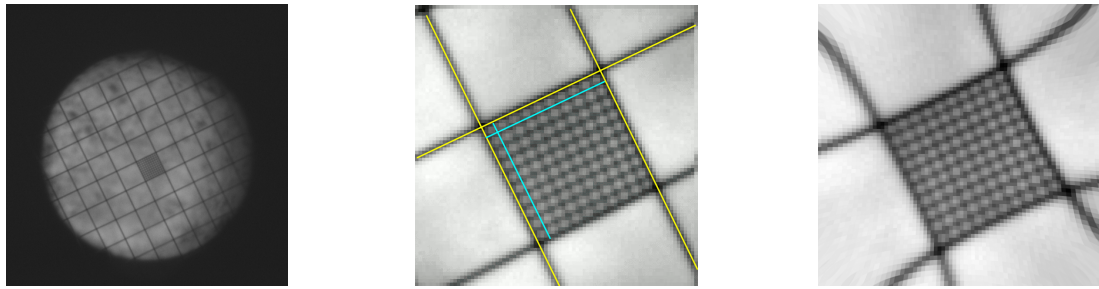
(a) Grid target for the identification of visual distortions.

(b) Close up on the central grid.

(c) Simulated lens distortions on the central grid

Figure 4.8: Verification of the absence of visual distortions. *Left*:The edges of the grid are slightly blurred due to the edges of the prism. The zone of interest is the beam passing at the center of the prism. *Middle*: Close up on the central grid. Some straight lines were added to prove the absence of distortion in the grid. *Right*: Simulated distortions from a lens to the grid, to illustrate a case with presence of distortions.

4.4 Prototype Set-Up Testing

4.4.1 Imaging

A first prototype of DeSSpOt was built in the lab to perform the next tests. It served to verify the imaging ability of the instrument and verify that the design fulfilled the instrument purpose: imaging simultaneously the same object under two anti-parallel orientations. As illustrated in the Figure 4.9b, the target is seen under two orientations, but both are slightly tilted. This effect, which is identified in both orientations, is not caused by the Dove prisms themselves, but by a small tilt of the base plate holding the prism and which has been amplified by the Dove prisms.
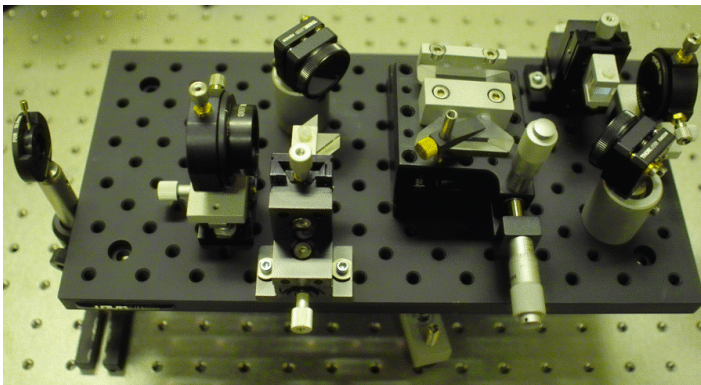
(a) Prototype of DeSSpOt for the imaging test. The light is collimated by the lens at the left, and focused on the detector by the lens at the right.

(b) First image through the DeSSpOt prototype

Figure 4.9: DeSSpOt prototype for the verification of the imaging properties.

I investigated the shape and intensity repartition of the point spread function (PSF) of the instrument. The purpose of this test was to control the effects of possible misalignment of the optical elements on the PSF of each channel. The object source was a 200 μm pinhole imaged through DeSSpOt on 27 pixels of the CCD detector. The spots showed effectively a shape and intensity dependent behaviour with the alignment and rotation of the beamsplitters. For instance, as seen in the Figure 4.10 on the right, the spot's peak intensity deviates from the centre. A large misalignment is charaterised by the apparition of a "plume" at one side of the spot, while the intensity peak is deviated in opposite direction. This effect was found to be related to the rotation of the first beamsplitter around

the vertical axis. With the current set-up of the instrument, this misalignment is hardly avoidable and can only be partially corrected by the adjustable mirrors. However, this effect was kept in mind during the design and construction of the new prototype, to ensure that the beamsplitter's surfaces are effectively orthogonal to the optical axis of the channel.
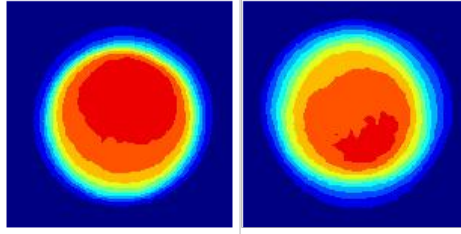

Figure 4.10: The spot shape through the instrument. A wrong alignment of the beamsplitter, causing the beam to reach the surface of the cube not orthogonally causes an off-centre peak intensity in the spots with an additional blurring around the edges of the spot. However, as long as the offset of the peak is controlled and constant, this does not degrade the spectroscopy of the stars.

4.4.2 Optical Quality

The whole prototype was also tested for optical quality. Each channel was tested separately. The test set-up is similar to the imaging test, except the CCD detector was replaced by a wavefront sensor. The protocol was the following:

- The incoming light is collimated with an achromatic lens. The radius of curvature of the wavefront, measured with the wavefront sensor, was above the 80 m, which guarantees a good collimated beam. The aberrations generated during the collimation are referenced with the wavefront sensor, for a later subtraction.
- The wavefront sensor is placed behind the set-up. The input of each channel is obscured alternatively in order to record the wavefront from only one orientation.
- The optical quality of each channel is calculated from the Zernike coefficients.

The results for each channel are in the Table 4.3. The optical quality of the overall set-up satisfy the requirements. Finally, this prototype fulfilled all the optical requirements, the optical quality of each channel is very good, with a Strehl ratio of at least 90%. The imaging quality of the instrument is also met. The imaging tests showed that the influence of the planarity of the Dove prism platform. The prism's deviations are well corrected by the selected mirrors.

	Channel $180°$	Channel $90°$
rms astigmatism (μm)	0.2205 ± 0.0022	0.1455 ± 0.0024
Strehl Ratio	91.23 %	97.48 %

Table 4.3: Optical Quality of DeSSpOt Channels. The channels are referred by the orientation angle of the Dove prism.

4.4.3 On a Moderate Resolution Spectrograph

Finally, the prototype was tested in this current configuration on a low resolution spectrograph. The purpose of this test was to verify that the spectra of each channel are comparable, e.g. similar line width, stability of the instrument on the spectra. The spectrograph used for this test was assembled from existing components:

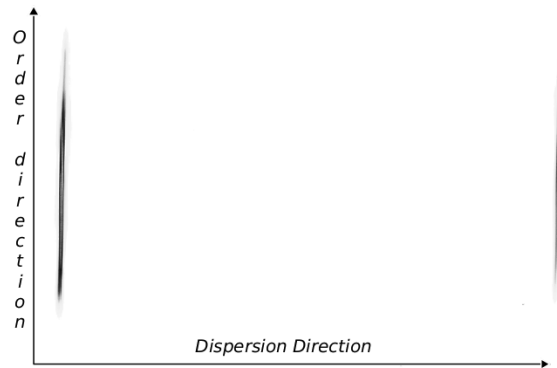- a large grating of 600 lines/mm with a blaze angle of $18°$,

Figure 4.11: Spectrum obtained with the lab-spectrograph for the orientation $180°$. Left the emission line at 633.44 nm, right the emission line at 630.48 nm. The lines are slightly tilted due to the small misalignment in the spherical mirrors.

- two identical spherical mirrors used as collimator and camera optic,
- a 640 x 480 pixels CCD detector,
- a neon emission lamp source with sharp lines.

The whole spectrograph is constructed after the Czerny-Turner design depicted in Figure 2.1, where the light is collimated by the first shperical mirror, refleted by the grating, and focused by the second spherical mirror on the detector. The observed spectrum corresponds to the first order of the grating. The linear dispersion obtained with this spetrograph set-up, was of 1.11 nm/mm, which converted into pixels meant that the detector saw a spectral band of 3.98 nm, correspond to a pixel plate scale of 0.0058 nm/pix.

Due to the large magnification factor of the spectrograph, both in spatial as in spectral direction, the spectra are spatialy very extended, and the emission lines are very separated. I chose the wavelength range 630 nm to 634 nm which covered two emission lines of different intensity. Furthermore, the spectrum of each channel was imaged separately, by blocking the light of the other channel.

The reduction of the images into an intensity spectrum was done along the 200 pixels of the order. The errors were estimated from the photon noise and the detector parameteres: $\sigma = \sqrt{RON^2 + Flux}$ in ADU. Each line was then fitted with a Gaussian. The width of the Gauss was compared for each orientation and each line. Since the source varied in intensity on a 50 Hz frequency, it affected the line profiles. Therefore, the exposure time was chosen much larger than the lamp cycle.

Since the source is homogeneous over its emitting surface, the spatial profile of each channel should in an ideal case be identical. Hence, comparing the shape of the emission lines is a possible means for studying each channel. I compared here the widths of each lines, extracted from the spectrum obtained for each channel. The closest the line widths, the more similar the overall shape of the lines. The widths were calculated once for a large slit, and once for a narrow slit. the results are displayed on the Table 4.4. This measurements were repeated over 51 images, and showed that the width difference (ΔW) is smaller than 0.05% of the line width in two cases, and $\Delta W \leq 0.1\%$ of the line width in 6 cases which proved the noise dependency of the measure.

This last test demonstrated the ability of the instrument to create nearly identical images of the source under two anti-parallel orientation in the lab with a very basic set-up. The next step is to validate the whole observing strategy by proceeding to observations on a telescope with a high resolution spectrograph.

4.5 Final Prototype for the TLS-Spectrograph

A special mount was constructed for the optical elements in preparation of an observation run with the TLS-Spectrograph. The mount was designed conjointly with the local workshop, and took

	Large slit				Narrow slit			
Channel orientation	90°	180°	90°	180°	90°	180°	90°	180°
Line position	633.44 nm		630.48 nm		633.44 nm		630.48 nm	
Width in pixels	2.538	2.653	2.527	2.680	1.805	1.811	1.828	1.845
Δ W	4.5%		6.0%		0.35%		0.96%	

Table 4.4: Comparison of the line widths of two emission lines for each channel. In the narrow slit case, the line width only differentiate by less than a percent despite the presence of noise. Meaning that the spectra of the channels are very similar.

into account the laboratory test results:

– The beamsplitters are in a two-surface contact with the mount. This shall ensure the orthogonality between the incoming beam and the cube's surface.
– The mirror mounts were milled, and the mirrors glued inside the hole so the instrument could be made more compact.
– The Dove prisms are both hold with two screws on top.
– Two additional fold mirrors were inserted in order to translate the output of the instrument toward the slit.
– The second fold mirror, M4, is adjustable, so the global beam direction can be rectified, while the first fold mirror is fixed to guarantee the 90° reflection.
– The whole mount was anodized and mounted on a breadboard of adjustable height.

The optical layout is presented in the Figure 4.12, while the final instrument is imaged in the Figure 4.13. In practice, in order to respect the channel separation on the slit, the two output beams had to follow parallel paths toward the slit, separated by around three millimeters. This value resulted from the slit height and the spot size on the slit. However, with this mount the image separation between the two channels was not sufficient. Indeed, either the spots were separated enough on the slit, but diverged completely on the collimator, or they reached together the collimator but overlapped on the slit. As a consequence, the first beamsplitter was rotated along the Y axis, in the plane of the instrument by a very small angle which helped to reach the required beam separation on the slit.
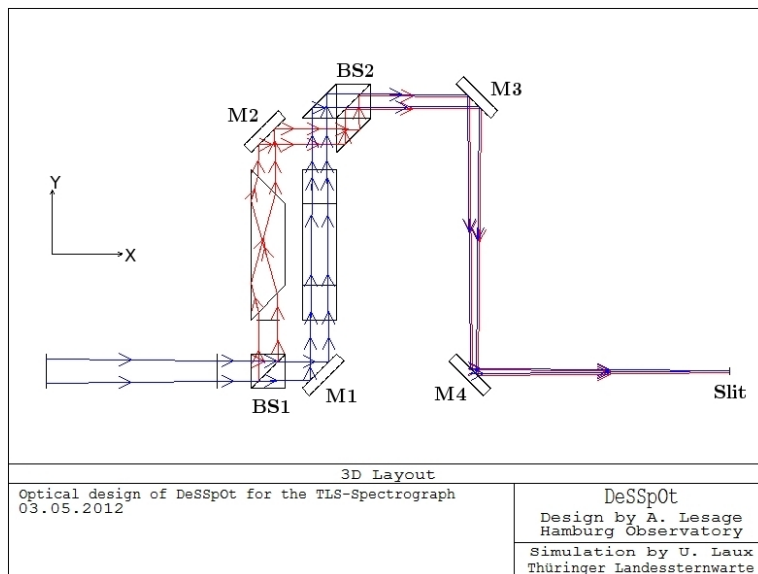
Figure 4.12: Optical layout of DeSSpOt for the TLS-spectrograph. The whole instrument was rotated by 90° to meet the space requirements given at the observing site. It includes now an additional fixed mirror M3 and an adjustable mirror M4.
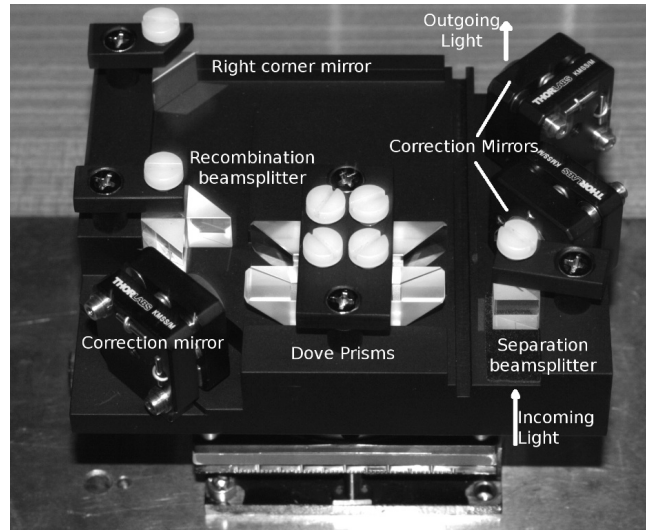
Figure 4.13: Final configuration of DeSSpOt before insertion on the TLS-spectrograph. The dimensions of the instrument are inside the requirements: 97 x 117 in length and width. The optical axis is respected thank to the two fold mirrors.

The TLS-Spectrograph is located in a room under the telescope. The light from the Coudé output is directed to the spectrograph thanks to five fold mirrors. The ensemble is configured with high precision so the stellar light reached the centre of the slit and the centre of the first collimator. The final step in the implementation of DeSSpOt to the TLS-Spectrograph is to adjust the instrument so the output beam follows the optical axis of the light. In order to do so, a laser was installed in the spectrograph room (see Figure 4.14). The laser was set on the optical path, such that the laser beam after reflecting on the middle of the collimator, pointed on a reference cross on the fourth fold mirror inside the telescope's branch. DeSSpOt was then inserted in the light path (see Figure 4.15) and adjusted until the laser beam pointed again on the reference cross on the fourth mirror.
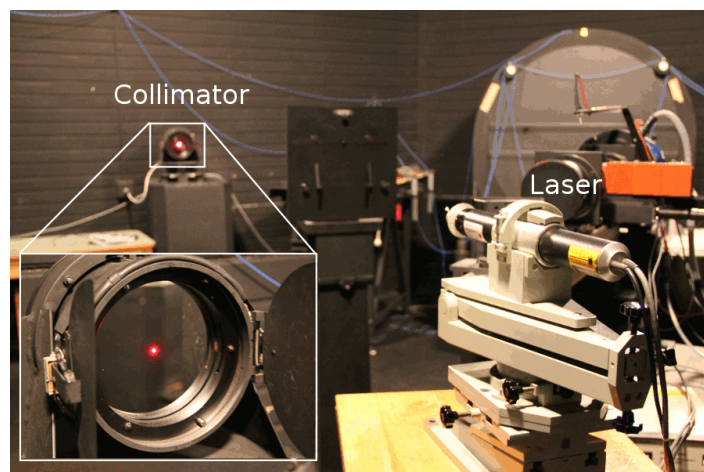
Figure 4.14: Set-up for the alignment inside the spectrograph room. The laser was place before the grating and pointed on a reference cross in the centre of the collimator.

The last adjustments, which consisted in moving the beams of each channel to an almost perfect overlap on the collimator, were made using a bright star like Vega as light source, so the beams were still seen inside the spectrograph room.
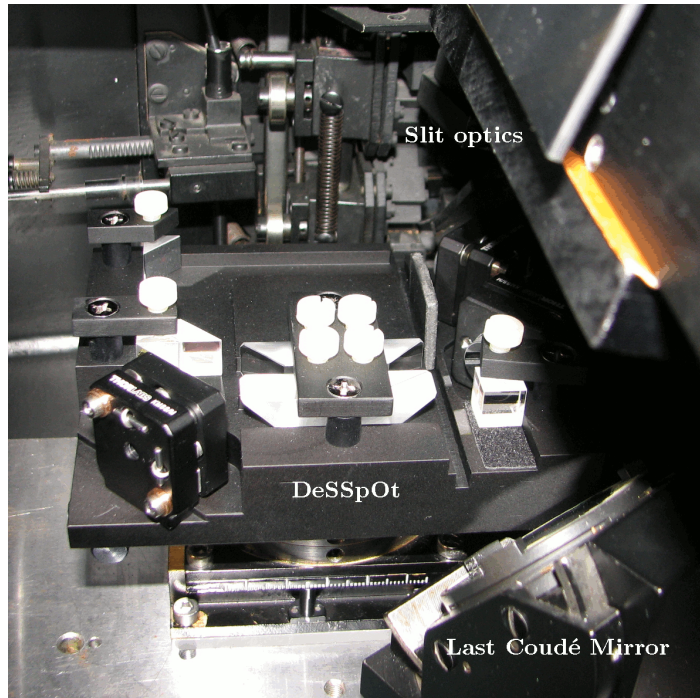
Figure 4.15: Implemented DeSSpOt during the alignment test. The 7th fold mirror is in the right bottom corner, and illuminated with the laser beam which has passed the whole DeSSpOt instrument to the slit optics. The slit itself is hidden by the optics.

4.5.1 Precision of the Beam Rotation

Finally, I verified on the finished prototype the accuracy of the rotation for each channel. The set-up was tested after the implementation, yet the previous adjustments for prisms and mirrors were kept untouched. The test was realised as follows:

- The source is a thin slit of 20 μm width and 2 mm length.
- The light is sent with an aperture ratio close to $F_{\#} = 46$ into the instrument.
- The slit is imaged on a CCD detector for each channel separately.

The images are then compared to each other and, if necessary, rotated till they overlap perfectly. As a result, the two channels differ from a perfect anti-parallel configuration by around $1.7° \pm 0.2°$. This difference is counted as a source for systematic errors in the determination of the stellar position angle.

Chapter 5

Observational results

5.1 Observations

I was granted one week observation time on the TLS-spectrograph in November 2011 for a final test phase with DeSSpOt. The goals of this campaign are twofold. First is to verify the functionality of DeSSpOt under real observing conditions. Second is to validate the method itself as a means to determine stellar position angles. From the seven nights granted, only three could be used for observation due to the bad weather conditions on site. During these good nights, the seeing was estimated around $2.5''$ to $3.5''$.

5.1.1 Installation on the TLS-Spectrograph

The Coudé spectrograph of the Thüringer Landessternwarte Tautenburg is a high resolution échelle spectrograph with peak resolution of 67 000 in the visible. It is located in a temperature stabilized room below the telescope, and is fed by a Coudé train of five mirrors. It is built after a white pupil design, which limits stray light in the spectrograph. The incoming light from the telescope arrives with an aperture ratio of $F_\# = 46$, and is collimated to a 150 mm diameter beam by the first collimator. It is diffracted by an échelle grating, with grating constant $d = 31.6$ lines/mm, and a blaze angle $\theta_B = 65°$. Due to the white pupil design, the diffracted light is focused slightly ahead of a fold mirror, which catches only the diffracted light before being redirected toward another collimator. The cross dispersion is carried out by a grism. There are three grisms available which provide respectively a coverage in the blue, in the visible and in the near infrared. Finally the spectrum is formed on a 2k x2k CCD detector.

The two pixel resolution of 67 000 is reached with a slit width of $0.52''$. In the visible channel the distance between two consecutive orders is at least 34 pixels with a limited slit height. In order to image properly the two images delivered by DeSSpOt on the slit, the slit height was increased, and another grism was implemented to avoid the resulting order overlap. The new grism, made of homosil, had an angle of $45.82°$, a coating of 600 lines/mm and a blaze angle of $33.57°$. Its maximal efficiency is reached at the blaze wavelength of 560 nm. The resulting inter-order separation was increased to 53 pixels with full prism height, at the cost of a lower transmission through the grism [1]. The new wavelength coverage extended from 420 nm to 650 nm.

DeSSpOt was inserted instead of the iodine cell, as it proved to be the only acceptable solution. The instrument fulfilled the space requirement, with a final size of 97 x 117 mm in length and width. The insertion of DeSSpOt in the light path resulted in a shift of the focus of 4 mm, which was easily compensated by the telescope, and a shift of the pupil over the grating of less than 20 mm, meaning that the pupil is still located on the grating. The first light images showed two clearly separated orders for each orientation, as well as closely identical number of counts between both orientations, as seen

---

1. A rough estimate gave that around 40 to 50% of the light is absorbed by the grism (H. Lehmann, private communication).
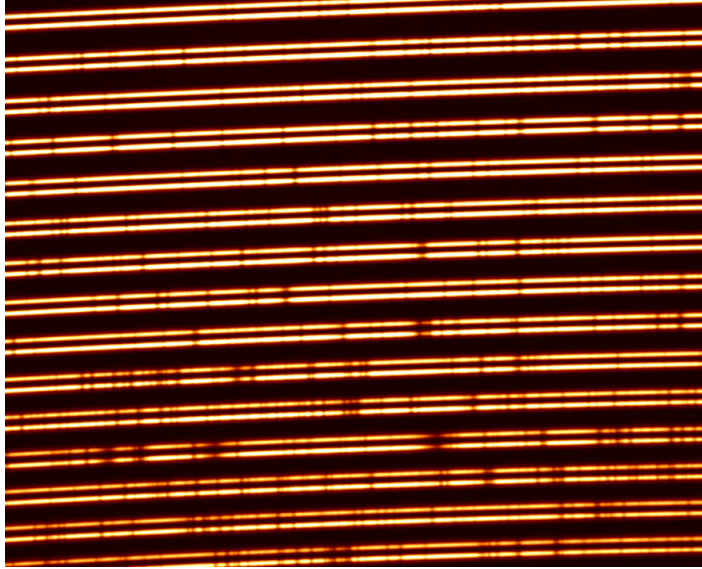
Figure 5.1: First light of DeSSpOt on the TLS-spectrograph with Capella. The two orientations are distinct and not overlapping. Moreover they are of similar magnitude.

in Figure 5.1. Absorption lines are easily identified in both channel spectra and located at the same position. The orientation at $90°$ is on every image brighter in the blue than the one at $180°$ which enables an easy identification of each orientation in the spectra afterwards .

5.1.2 Targets

The observational targets were selected by their apparent diameter and rotational velocities. Stars of spectral type F and hotter were discarded due to their lack of spectral features. Using the JMMC catalogue for stellar diameters from Lafrasse et al. (2010) and the catalogue of stellar rotational velocity of Glebocki & Gnacinski (2005), I compiled a list of optimal targets, large apparent diameter and rotational velocity below 10 km/s, for the observation campaign. This list includes also Aldebaran.

Furthermore, a set of spectroscopic binaries whose orbits are well defined were included to the target list. The spectro-astrometric signal generated by a binary system is very close to that of a single rotating star. Indeed on a single star, I concentrate on the velocity difference between two points located on the equator of the star, and are limited in detection by the diameter of the star, its rotational velocity and the consequent line broadening. On the contrary, in a binary system, the radial contribution of each star, caused by their orbit, is not related to a line broadening. Hence the amplitude of the signal, linked to the separation of the stars and their radial velocity, is higher than for a single star and easier to detect. The observed targets are listed in Table 5.1. They included two binary systems: Capella and η Andromeda. The former, whose components are of similar magnitude and are separated by around 50 mas, is the best possible target to verify the method[2]. The latter, whose components are closer, is to set a lower limit for binary stars.

In order to retrieve the true stellar position angle, three measurements at different slit orientations of the targets are needed. Using the natural field rotation of the Coudé modus, the targets were probed at different times during the night. The projected slit position angle on the sky is calculated from:

$$PA_{slit} = 151° + \delta - \tau \tag{5.1}$$

where τ is the hour angle of the target, determined from the right ascension and the observing point[3]. All targets were observed if possible at an altitude above $40°$ in order to minimize the effects of

---

2. The fact that both components are equally bright, and of similar spectral type, is of advantage. In addition, Capella has been observed so often in the last century, that its orbital parameters are known with high precision.

3. This also implies that the image of the star rotates during the exposure time. With the addition of DeSSpOt the

airmass and atmospheric refraction on the spectra. On average each observational run captured 10 images of the target which corresponded to an hour per run. Unfortunately Kochab and η Andromeda could not be observed a second night due to bad weather conditions.

Targets	Run	Nights	Date JD (+ 245e4)	Slit Angle in °	Airmass
Capella *	run 1	04 - 05 Nov 2011	5870.451020 ⋯ 5870.50235	238.1 ⋯ 219.6	1.138 ⋯ 1.045
	run 2		5870.677959 ⋯ 5870.697650	156.3 ⋯ 149.1	1.112 ⋯ 1.159
	run 3	05 - 06 Nov 2011	5871.453430 ⋯ 5871.485239	236.2 ⋯ 224.8	1.126 ⋯ 1.065
	run 4		5871.636306 ⋯ 5871.668078	170.30 ⋯ 158.85	1.046 ⋯ 1.096
Aldebaran	run 1	04 - 05 Nov 2011	5870.418054 ⋯ 5870.444760	210.5 ⋯ 200.8	1.544 ⋯ 1.402
	run 2		5870.620958 ⋯ 5870.671690	137.2 ⋯ 118.85	1.328 ⋯ 1.571
	run 3	05 - 06 Nov 2011	5871.394189 ⋯ 5871.432316	218.2 ⋯ 204.4	1.703 ⋯ 1.447
	run 4		5871.599073 ⋯ 5871.630649	144.1 ⋯ 132.7	1.762 ⋯ 1.371
Kochab	run 1	08 - 09 Nov 2011	5874.216755 ⋯ 5874.254781	130.5 ⋯ 116.8	1.363 ⋯ 1.443
	run 2		5874.581678 ⋯ 5874.611903	358.9 ⋯ 347.9	1.593 ⋯ 1.530
η Andromeda *	run 1	08 - 09 Nov 2011	5874.282093 ⋯ 5874.320116	-152.2 ⋯ -165.1	1.283 ⋯ 1.182
	run 2		5874.535948 ⋯ 5874.555624	116.1 ⋯ 109.1	1.583 ⋯ 1.754
Vega	calibrator	04 - 05 Nov 2011 05 - 06 Nov 2011	5870.288193 55871.276641	⋯ ⋯	1.368 1.326

Table 5.1: List of the observed targets, with the corresponding slit angle and airmass during observation. The targets marked with an asterisk are binaries. The observation of Vega permitted the identification of the telluric lines, necessary for the analysis.

---

standard tracking and guiding of the telescope was no longer effective. Therefore, the telescope was guided by hand in order to keep the two stellar images on the slit.

5.2 Reduction

5.2.1 Pre-Reduction

The pre-reduction of the spectra, which includes bias correction, flatfielding, descattering and wavelength calibration, was done with IRAF[4]. Flatfields were realised with the whole slit illuminated. Therefore both orientations yield the same flatfield normalisation. I also used the flatfields images to check the presence of bad pixels. Some bad lines could be identified and be marked for the upcoming extraction. Similarly, the correction of scattered light was done using the whole slit aperture, and neglecting the inter-orientation space.

Further reduction could not be achieve with this software. Therefore, I wrote an extraction program for IDL dedicated to the spectro-astrometric reduction of spectra.

5.2.2 Extraction

The extraction package was written on IDL. It comprises several steps: finding and fitting the orders of the spectrum, extracting the intensity spectrum, extracting the position spectrum and finally correction of pixellation effects in the position spectrum.

The spectral orders are curved on the detector. Each order, for each channel, is fitted by a polynomial of degree 3. The extraction of the intensity spectrum is then done by collapsing the orders along the slit direction. Due to the important curvature of the blue orders, I used the extraction algorithm proposed by Marsh (1989) and adapted on IDL by Pfeiffer et al. (1998). This method allows a good evaluation of the errors for each wavelength, and an identification and correction of deviant pixel. The extracted spectra are then normalised to unity.

The position spectrum is calculated along the orders with the centroid method. Special attention has to be given on the integration interval considered. Indeed the interval should be small enough so the centroid is not influence by the next spectral order, but also big enough to increase the precision and accuracy of the measurement. The resulting position spectra are then corrected of the order's trace. The trace is basically the function describing the order on the detector. During this step, pixellation effects can appear and completely destroy the signal, if not corrected, see Figure 5.2. They occur when the photocenter of the order jumps to a new pixel in spatial direction. Due to the finite size of the pixels, the transition of the photocenter from one pixel to another is not smooth, but in a step by step function.

The correction of the pixellation effects is performed by reproducing this effect numerically. This process is achieved with a simplex approach comparing the extracted position spectrum with a simulated position spectrum following the same trace. Further details are in the Appendix A.2. The completion of this process is time consuming due to the simplex approach. Therefore, the program includes the possibility to be paralellised on several CPUs, reducing the calculation time by a factor proportional to the number of CPU used.. The corrected position spectra are free of any visible pixellation effect, and are ready for the analysis. The noise level is around 2% of a pixel.

5.3 Results - Capella

5.3.1 Target Properties

Capella is a system whose components are both giants stars, spectral type G8III and G0III, with similar magnitude, $m_v = 0.71$ and $m_v = 0.96$, and with moderate rotational velocities, 4.5 km/s and 35 km/s for the A and B components respectively (Weber & Strassmeier (2011)). The orbit has been calculated several times using both spectroscopic and interferometric measurements. The latest

---

4. IRAF is the Image Reduction and Analysis Facility, a general purpose software system for the reduction and analysis of astronomical data. For the generation of the flatfield reference image, I used the procedure *apflatte* which conserve the 2D information in the spectra.
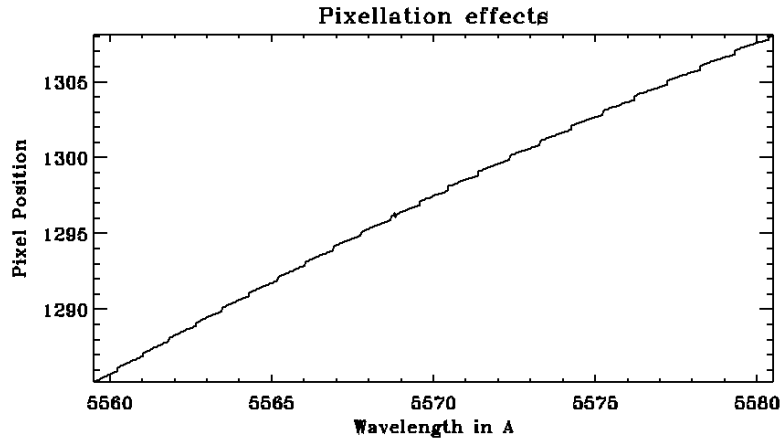
Figure 5.2: Pixellation effects on the position spectrum. The spectrum presents some "steps" in its shape which characterise the pixellation effects. The more curved the order, the more "steps" are present.

results, given by Torres et al. (2009), gave as position angle for the orbit, i.e. the position angle of the ascending node Ω, $PA_{Capella} = 40.421° \pm 0.064°$. The peak in the spectro-astrometric signal is expected when the slit is orthogonal to the system's position angle. This configuration was almost achieved in the runs 2 and 4. Due to the inclination of the orbit, the projected separation of the binaries at the observation dates was of 34 mas maximum. In addition, the system's radial velocity is estimated around 16 km/s and 13km/s for the first two and last two runs respectively.

5.3.2 Determination of the Orbital Position Angle

A direct identification of the signal in the position spectrum is not possible. Therefore, the signal is recovered using the cross-correlation analysis described in Section 3.2.3. The cross-correlation functions (CCF) of the anti-parallel orientations are subtracted to enhance the signal and remove the remaining artefacts from the reduction. The seeing contribution in the CCF difference (ΔCCF = $CCF_{0°}$ - $CCF_{180°}$) is compared to that of the stellar lines. The ΔCCFs for seeing are calculated using telluric lines identified from the Vega spectrum, while the stellar ΔCCFs are calculated from stellar lines only. Thus the latter enclose both the stellar and the seeing signal. The lines are selected according to the following criteria: deep and narrow lines, not blended to another line in a neighbourhood of 7 pixel, and for the stellar lines not blended with a telluric line.

As seen in Figure 5.3, the seeing component is still very strong in the difference of the cross-correlation functions. However the four runs present distinct ΔCCFs: in the runs 1 and 3 the stellar ΔCCFs follow the shape of the telluric ΔCCFs. On the contrary, during the run 2 and 4, the stellar ΔCCFs diverge visibly from the seeing ΔCCFs. These trends are confirmed when correcting the stellar ΔCCFs from the seeing ΔCCFs. Consequently, a signal is detected at the expected orientations in the Capella data. If I hadn't done this verification by separating the stellar from the telluric lines, the signal would not have being detected. Therefore it is a necessary step in the analysis process to compare the seeing contribution in the CCF to the stellar one.

I used the corrected ΔCCFs to determine the system's position angle. The maxima of the functions are extracted and plotted versus the projected slit angle during the observations. The values of the maxima do not diverge during one run and reflect the accuracy reached during this run. Thus the errors for each point are evaluated from the dispersion of the cross-correlation maxima during the respective observation run. The data is fitted with a sine curve of amplitude 0.9 and period 2π using a χ^2 reduction. The least square solution for the phase yields an orbital position angle of $50.31° \pm 1.75°$. The Figure 5.4 shows the measured data points with their error bars, and the corresponding best fit
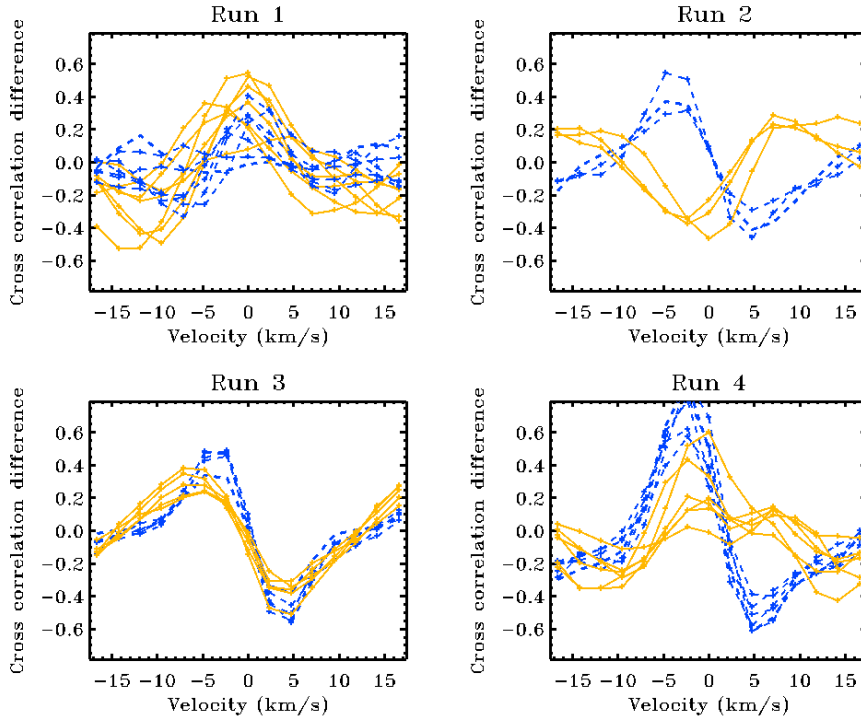
Figure 5.3: Cross-correlation function differences for Capella. In blue the seeing contribution, and in red the stellar contribution. On the run 2 and 4, the stellar ΔCCFs do not follow the shape of the telluric ΔCCFs. In the run 4, the seeing contribution dominates partly the stellar contribution.

sine curve. In order to evaluate the accuracy of the analysis method, a curve using the true orbital position angle in the phase is also plotted. Three of the four sets of data points match with good consistency with this curve. Only the set of data points obtained during the third run lies outside the errors. Using only the three good sets of data points, the resulting position angle is $37.69° \pm 2.13°$ which is consistent within the errors with the value of Torres et al. (2009). In the next Section, I shall discuss the quality of the analysis method and the deviations of the Run 3.

Estimation of the Systematic Errors

The errors in the phase delivered by the fitting method are directly related to the errors of the points. Yet the phase errors remain too small to explain the large discrepancy found between our calculated value for the position angle, and the value from the literature. During the previous chapters, I identified three sources of systematic errors, which are either instrumental or computational.

– The image rotation precision of DeSSpOt was verified, and an error of $1.7° \pm 0.2°$ were found for one orientation. Due to the analysis method, this error is passed on the probed slit angles. In addition, the formula giving the projected slit angle on the sky is determined with an precision of around $1.5°$. As a result, I have an error in the slit angle of $\delta_{slit} = 2.26°$

– During the simulations made to ascertain the analysis method, I noticed a regular offset of the determined position angle of $\delta_{off} = 4.8° \pm 0.5°$. Due to the regularity with which this offset appeared, I can affirm that the method produces an overestimate of the position angle.

As a result, the retrieved phase is overestimated by an angle $\delta_{sys} = -4.8° \pm 2.32°$. By implementing this result in the position angle determined previously, the position angle of Capella is:

$$\boxed{\mathrm{PA}^{obs}_{Capella} = 50.31° \pm 1.75° + \delta_{sys} = 45.51° \pm 2.90°} \tag{5.2}$$
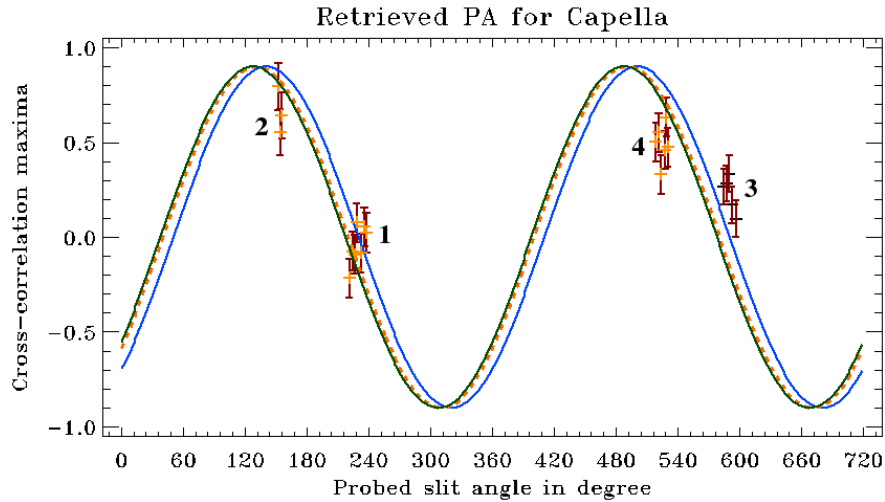
Figure 5.4: Retrieved position angle for Capella. The measurements are marked with the error bars. In blue the best fit taking into account all the measurements with an orbital PA of $50.31° \pm 1.75°$. In dotted, the sine curve with the true orbital position angle. In green, the best fit obtained by neglecting the set of data points of the Run 3, which yields the angle $37.69° \pm 2.13°$. The dotted and green curve almost perfectly overlap.

5.3.3 Discussion

Since the corrected value for the observational position angle of the Capella system is still outside the reference value, I tested four implementations to the method in order to improve the results.

Wrong Parameters of the Fit

The sine fit was constrained to an amplitude of 0.9. This value seemed reasonable since the values of the cross-correlation functions are comprised between -1 and 1. However, the amplitude of the ΔCCF could theoretically vary from -4 to 4. Thus, the fit was run again, once by setting the amplitude to 3.9, and once by leaving the amplitude free to vary. In the first case, the calculated phase increased by a few degrees, but the fit was very poor. In the second case, the χ^2 minimum is reached for an amplitude of around 0.6, yet the phase stayed mostly constant. Only the χ^2 goodness of fit was lowered compared to a fixed amplitude. As a result, setting the amplitude of the sine curve in the fitting algorithm did not influence the results enough to explain the discrepancy in our determined position angle.

Another variation in the fit was performed by weighting the data points to the errors in the position spectrum. Indeed if the errors are very low, it means that the Signal to Noise ratio for this observation is good. With the weighting coefficients, data points extracted from a good position spectrum has more weight during the fitting process than the other data points. The weights then replace the errors of the cross-correlation maxima. Yet the calculated phase increased, and the goodness of fit remained in the same order of magnitude.

To conclude, the discrepancy between our calculated value of the orbital position angle and the reference value can not be explained alone by a bad choice in the parameters of the fitting algorithm. Hence, the errors lies inside the data and the extraction of the cross-correlation maxima.

Variations in the Signal to Noise Ratio

The quality of the position spectrum should reflect in the calculation of the ΔCCF. For instance, one could expect that the data points extracted from the Run 3 are outsiders because of the seeing or of the signal to noise in the position spectrum. Figure 5.5 shows cuts made in cross-dispersion direction for every images of each run. The exposure time was kept constant, the variations in amplitude are
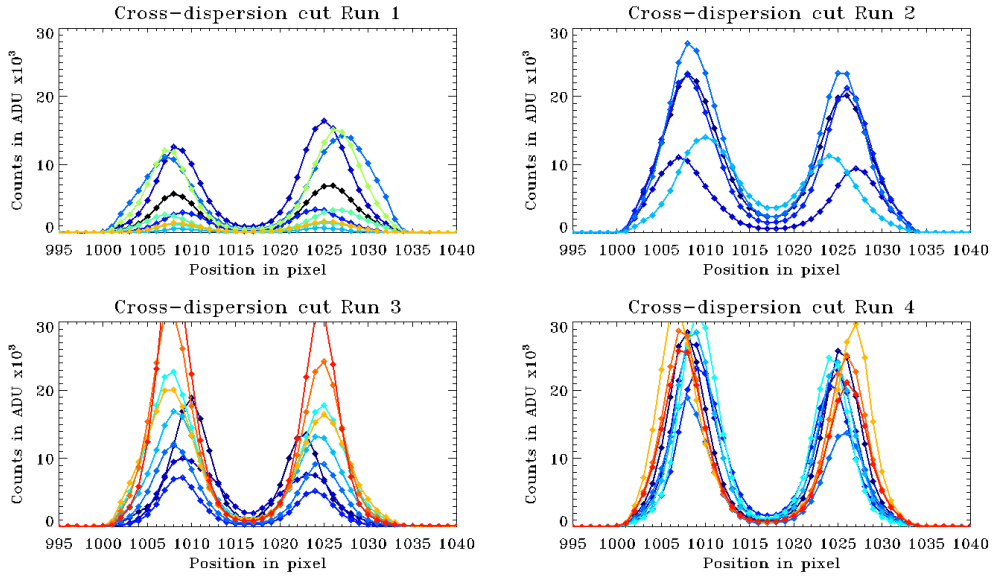
Figure 5.5: Cross-dispersion cut of the spectral images for the four observation runs. Each images is given another colour. The cut shows the variations in the intensity and in the position of the two orientations. These parameters have the most important variations during the Run 1 and 3, while they remain close to constant on Run 4.

caused by the wobbling of the stars on the slit, causing a loss of light to the spectrograph. The Run 3 is characterised by having the largest variations in amplitude, while the Run 4 should yield the results with the greatest consistency if the SNR is the source of the discrepancy. Yet, the standard deviation of the cross-correlation maxima in this run is similar to that of the other runs. In addition, while the seeing ΔCCFs followed all the same shape, the stellar ΔCCFs were diverging from another. On the contrary, only in the run 3 did the ΔCCFs remain so constant, see Figure 5.3. This is contradictory with the assumption that the variations in the signal to noise would be reflected back in the cross-correlation functions and consequently in the cross-correlation maxima.

Variations in the Wavelength Solution

The cross-correlation functions used previously are obtained by considering the complete 96th spectral order for each orientation in order to use a maximum number of absorption lines. Yet, on such large wavelength interval as covered in one order, e.g. 100 Å for the order 96, the resolution decreases toward the longer wavelengths. In addition, the diffraction effect caused by the Dove prism oriented at 90° also influences the wavelength solution along the order. Taking the whole order for the cross-correlation analysis could therefore degrade the signal instead of improving it.

Hence the order was separated into four pieces of identical size covering each approximatively 25 Å. The same analysis as before was performed for each piece: selecting the telluric and the stellar lines, calculating the cross-correlation functions for each orientation, once for the stellar lines and once for the telluric lines, determining the ΔCCFs and finally correcting the stellar ΔCCFs from the seeing ΔCCFs. The corrected ΔCCFs vary from piece to piece for each run, as pictured in Figure 5.6. The first and the fourth chunk present the largest dispersion for the corrected ΔCCF. I counted the number of telluric and stellar lines used respectively in each piece to calculate the cross-correlation functions, refer to Table 5.2, in case the divergences are caused by a low number or worse an absence of lines in this chunk. The chunk 2 and 3 combine both the largest number of lines which is consistent with their lower dispersion for each run.

At last, the orbital position angle of Capella is determined again for each chunk separately. Figure 5.7 illustrates the results for each piece of the spectral order. Despite having the largest number of stellar and telluric lines used for the cross-correlation functions, chunk 3 presents the worst fit. The
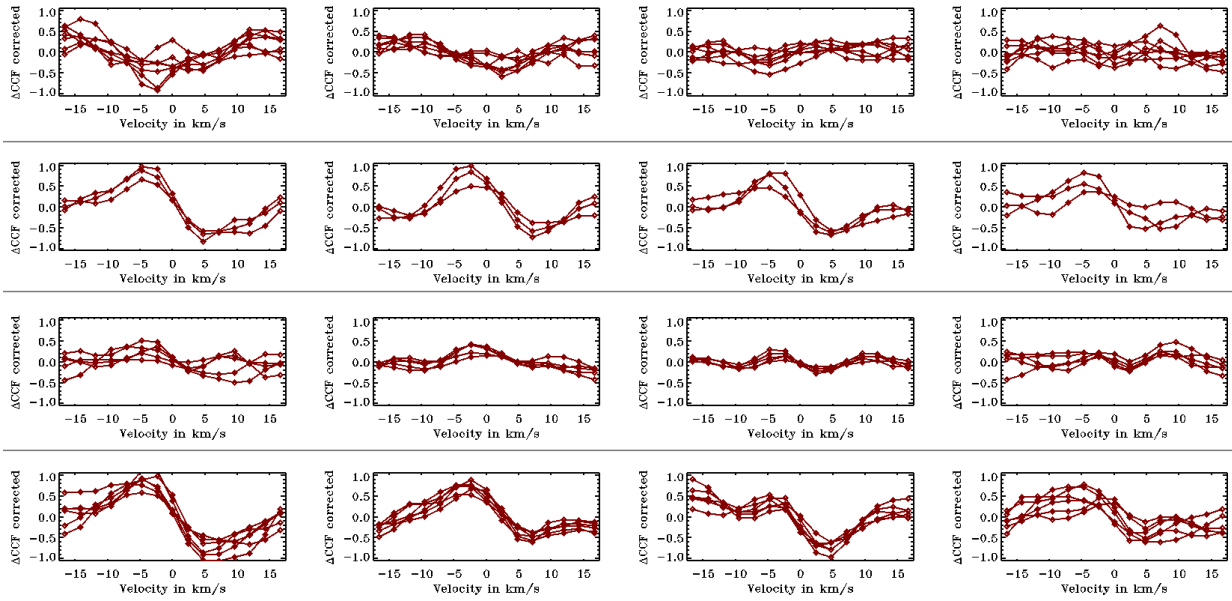
Figure 5.6: Corrected ΔCCFs obtained by dividing the order in equal parts. The results are represented for increasing run number from top to bottom. The variations from chunk to chunk are particularly visible in the Run 4 on the bottom.

Number of lines per piece			Determined position angle
Chunk number	Telluric	Stellar	
C1	9	3	$56.49° \pm 3.25°$
C2	8	5	$50.43° \pm 1.30°$
C3	9	6	$57.70° \pm 1.69°$
C4	7	4	$63.68° \pm 1.34°$

Table 5.2: Number of lines used per chunk for calculating the cross-correlation function. The number of telluric lines is in average 7 while the number of stellar lines varies more from chunk to chunk.

fit is completely outside the error bars of the data points of Run 4. The phase solution delivered for each chunk can be found in Table 5.2. The final position angle, obtained by averaging the previous values, is $57.07° \pm 4.11°$. Consequently, the use of chunks by itself did neither improve the value of the corrected ΔCCF maxima used for the fit, nor the fit itself. On the contrary, the data points are more dispersed than when using the whole order, and vary notably from one piece of order to the other.

Constraining the CCFs

At last, I verified if the results could be improved by using more stellar lines in the calculation of the cross-correlation functions. Since the number of used stellar lines is low compared to the number of used telluric lines, both cross-correlation functions should not yield the same precision. Hence, by using more stellar lines, extracted from an adjacent order, the stellar CCFs should improve in precision. The analysis was done over the orders 95 and 96. Only the second half of the order 95 is covered with telluric lines, hence raising the number of good stellar lines to select. The seeing ΔCCFs present similar trends in both orders. Finally the corrected ΔCCFs are calculated for each order. As seen in the Figure 5.8, there is a good correspondance between their shapes over the runs, in particular Run 1 and Run 4. The corrected ΔCCFs of the order 95 present a lower peak in the Run 2 than those from the order 96. Contrary to that, the shape of the corrected ΔCCFs from the order 95 during Run 3 are improved. Finally, using the average of the corrected ΔCCF from both orders
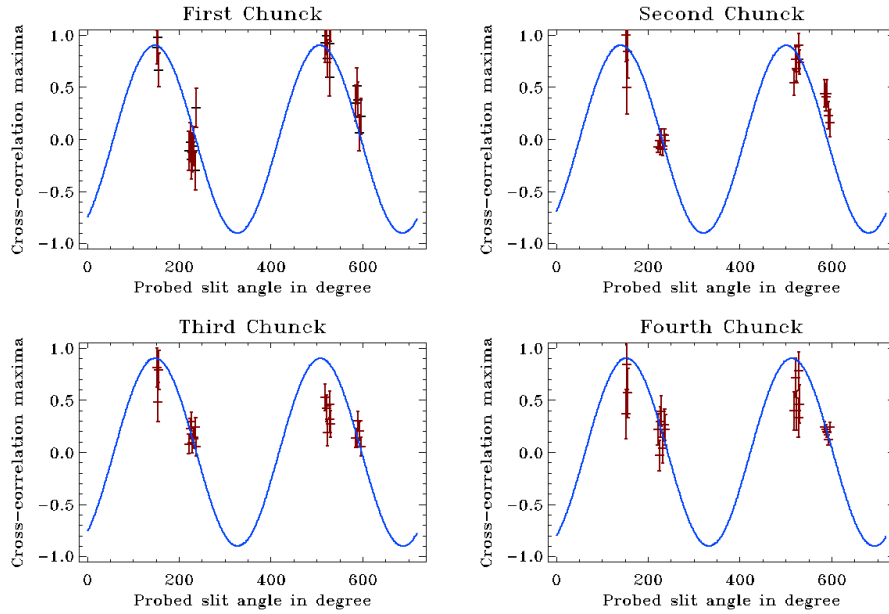
Figure 5.7: Retrieved position angle for each chunk respectively. Compared to the curve obtained using hte whole order, these are characterised by enhance dispersion in the data points of each run, large variations of the value of the corrected ΔCCF maxima for the Run 1 and 4, and a degradation of the fit.

to determine the orbital position angle, the χ^2 reduction produces a phase solution of $52.05° \pm 0.5°$. The goodness of fit is moderate, with two sets of data points outside the fit. The low value of the extracted maxima used for the fit for the Run 2 and 4 causes the degradation of the retrieved value for the position angle.

To conclude, several methods were tested to improve the analysis of the images in order to reduce the discrepancy between the determined orbital position angle of Capella and the reference value. The possible sources of errors proposed were: a bad choice in the fit parameters, variations in the Signal to Noise ratio during the observation, dispersion caused by the Dove prism and a lack of lines. Each issue was treated separately. Yet, their solutions did not improve the accuracy of the position angle. Using chunks of the orders showed that the cross-correlation functions are varying with wavelength. In addition the number of lines per chunk had only a minimal influence on the CCFs. Using more orders could improve the signal, but since the seeing CCF are wavelength dependent, it also requires an important overlap of the region of atmospherical absorption and the region of stellar absorption.

5.4 Results - Aldebaran

Aldebaran is one of the largest stars in the sky, with an apparent diameter of around 20 mas in the visible. It is also one of the brightest in our hemisphere ($V_{mag} = 0.89$), making it an ideal target to test the method on single stars. Aldebaran is a typical red giant of spectral type K5III, it possesses a large number absorption features in its spectrum, which guarantees good available lines for the analysis. Furthermore its rotational velocity was determined by Massarotti et al. (2008) around 4.3 km/s, the spectral lines are barely broadened, and remain deep and narrow.

Aldebaran, like Capella, was observed during four observation runs, probing four slit orientations. The reduction of the spectra was performed using the same procedures as for Capella. Pixellation effects were corrected and position and intensity spectrum are extracted for analysis. The position angle of Aldebaran was already determined to be $110° \pm 5°$ by Lagarde et al. (1995) using Differential
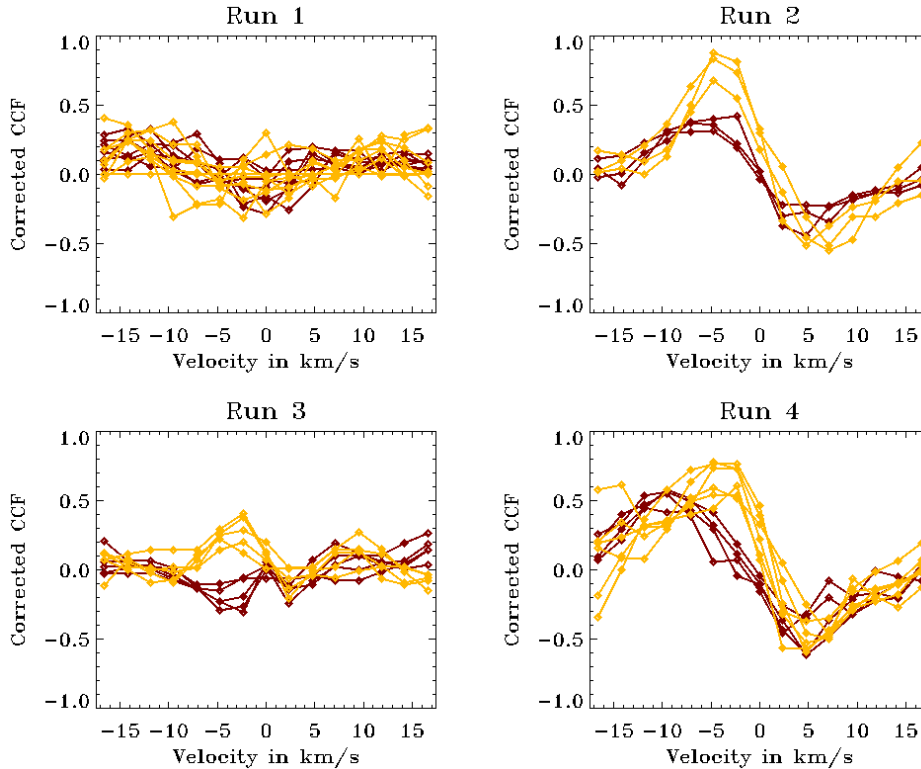
Figure 5.8: Corrected ΔCCFs for the orders 96 and 95. In dark red, the functions issued from the order 95 and in orange the functions from the order 96. The trends are similar for both orders: low correlation coefficients for the Run 1 and 3, and moderate higher values for the runs 2 and 4.

Speckle Interferometry. The purpose of this analysis is to verify whether this value can be retrieved from our measurements, or at least evaluate the limits of the method for single stars.

5.4.1 Defining Spatial Seeing Trends

Due to the large number of absorption lines in the Aldebaran spectrum, it is not possible to identify good telluric lines. They are either blended to the stellar lines, or too small to be qualified as good. Hence I used the seeing contribution from exposures made right before and right after the observations of Aldebaran for the correction of the differential cross-correlation profiles. Indeed, the analysis of Capella has shown that the seeing ΔCCFs, meaning the difference between the cross-correlation functions of the anti-parallel orientations calculated only from the telluric lines, display a trend which remains constant during the one hour observations. This statement is verified using the seeing observations made during the observation of Capella, Vega and Algol. Figure 5.9 shows the seeing ΔCCFs obtained during one observation run for Vega and Capella. The time elapsed during a run is roughly one hour. Due to its highly changeable nature, it is expected that the seeing functions vary notably from one image to the other. However, the ΔCCF profiles are significantly similar during a run. This trend was observed in the four observing runs for Capella, and in the Vega data. It clearly proves that the main contributor of the seeing ΔCCF is a large scale component varying on a long time scale compared to the exposure time used here. The spatial seeing signature is therefore composed of a large scale component which varies slowly and dominates the signal, and of a small scale component varying on very short time scales.

Thus, I assumed that the seeing ΔCCFs for Aldebaran would remain close to those observed for the star observed right before, Algol, and the star observed right after, Capella. A further assumption is that only small pixel shifts could occur from one star to the other. These shifts, of one to maximum two pixels, are accepted here since the ΔCCFs are issued from different images. To verify this
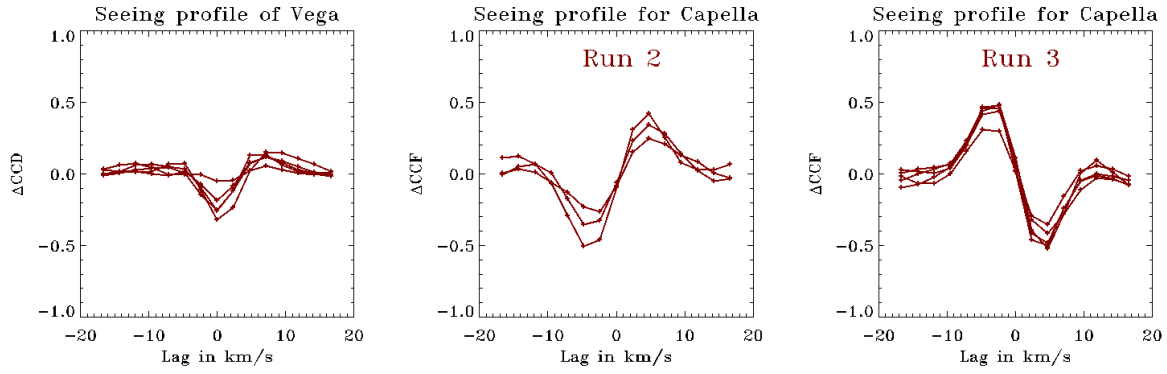
Figure 5.9: Trends in the seeing ΔCCF during one observation run. The ΔCCF functions follow nearly similar profiles during a run. This illustrates that the seeing contribution is dominate by a slow varying component, which is visible here. The low-scale component causes the fluctuations in the profiles.
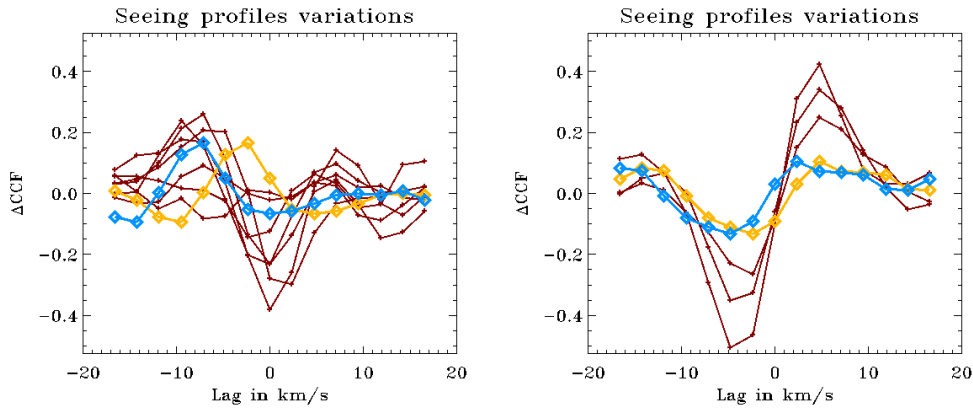
Figure 5.10: Seeing variations from Algol to Capella. *Left*: For the Run 1 of Aldebaran, *Right*: For the Run2 of Aldebaran. In straight dark red lines, the ΔCCFs calculated during the observation of Capella. In orange, the ΔCCF from the last image of Algol. In blue is plotted the best overlap of bothΔCCF, issued from a small shift. In the first run, the shifted profile matches reasonably the trends describes by the ΔCCFs during the Capella observation. On the Run 2, the shift causes a degradation. Yet on the Run 2, time dependent changes seem to be observed in the profile. The features are increasing with time.

hypothesis, I compared the ΔCCFs from Algol and Capella. As illustrated on Figure 5.10, the ΔCCFs of both images follow close trends. This result sheds light on the fact that the seeing contribution in the position spectrum is latitude independant. Despite, the fact that the telescope was pointed at two different targets located at different coordinates, the main component of the spatial seeing contribution is apparently constant.

5.4.2 Determination of the Position Angle

One of the previous assumption was that the seeing ΔCCFs are allowed to move from one to two pixels between the observations. Figure 5.11 present the comparison between the seeing ΔCCFs of Capella and the stellar ΔCCF of Aldebaran. All the functions per run of Aldebaran follow the same profile. The dispersion between the functions is reduced compared to Capella due to the large amount of stellar lines available in the Aldebaran spectrum. Furthermore, the run 2 and 4 present important trend, which are almost perfectly reproduced in the seeing ΔCCFs of Capella, assuming a shift of 1 to 2 pixels. Whereas the necessity of this shift is not clear in the Run 1 and 3, since the maxima are
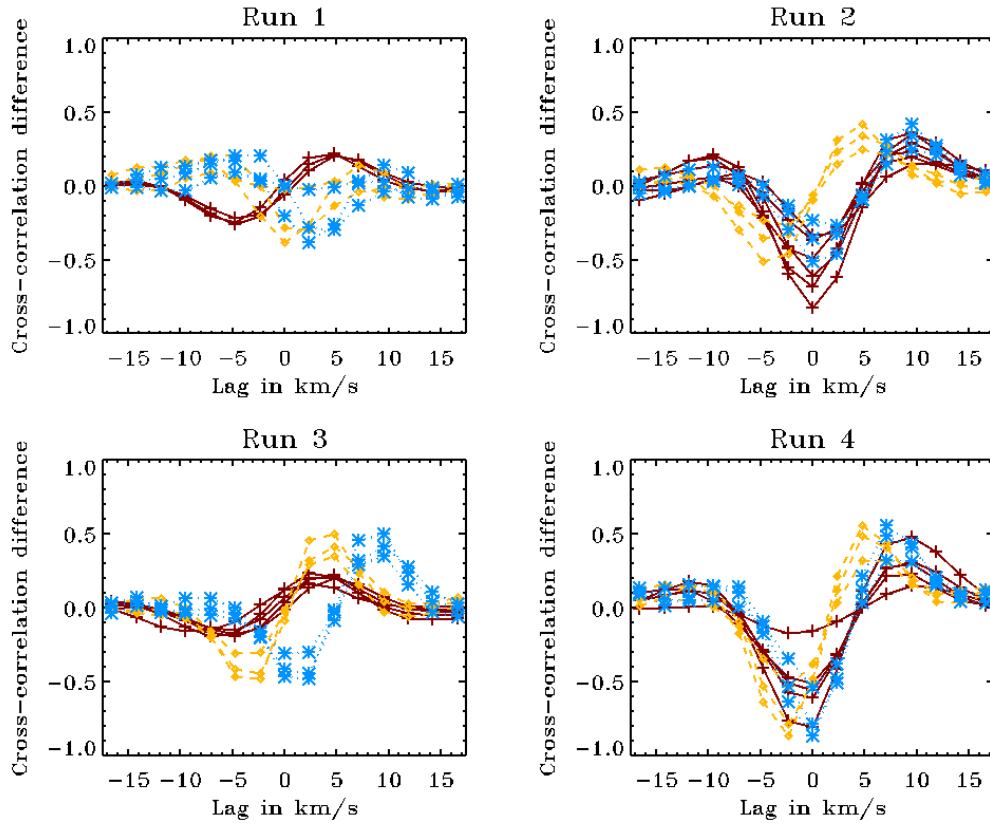
Figure 5.11: Cross-correlation differences for Aldebaran. In red, the ΔCCFs calculated for Aldebaran, in orange the original seeing ΔCCFs calculated for Capella, and in blue, the latter shifted by one to two pixels, until the maxima/minima are located at the same pixel positions. For instance, in Run 3, the data shifts are displacing the maxima, are would degrade the signal. While for the Run 2 and 4, the shift provides an almost perfect overlap with the ΔCCFs of Aldebaran.

already located at the same lag value.

Finally, using the seeing ΔCCFs for the correction of seeing effects, the maxima of the corrected functions are extracted and plotted versus the probed position angles. The determination of the error bars and the fitting procedure are done identically as for Capella. The retrieved position angle is then:

$$\boxed{\text{PA}_{\text{Aldebaran}} = 119.62° \pm 2.45° + \delta_{sys} = 114.82° \pm 3.4°} \tag{5.3}$$

which is in agreement with the value determined by Lagarde et al. (1995), knowing that I did not account here for the angle overestimation generated by the analysis method..
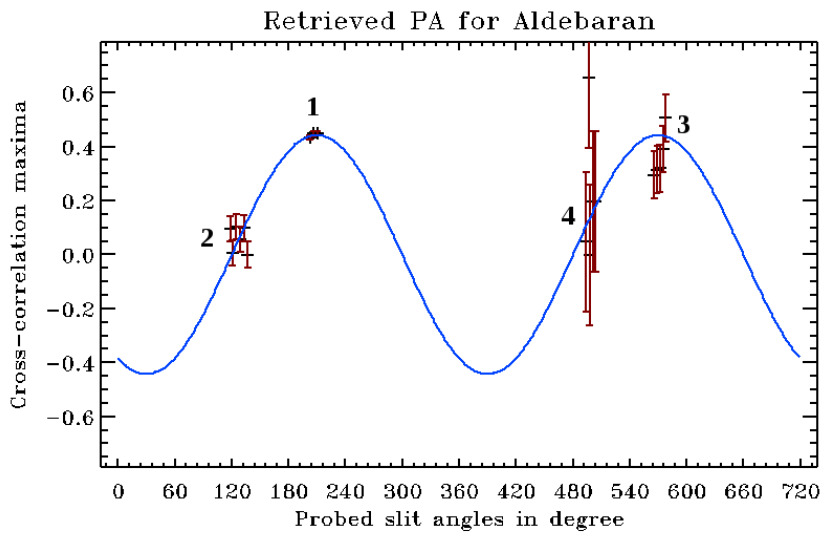
Figure 5.12: Retreived position angle for Aldebaran. The large error bars for the run 4 are caused by a single deviant measurement. which shows also the limits of this error evaluation method. The goodness of fit χ^2 is very low, thanks to the moderate amplitude for the sine curve.

Chapter 6

Conclusion and Outlook

6.1 Discussion

From the theory developed in the Chapter 3, it was expected with DeSSpOt that the correction of the seeing would be very simple. Both orientations have seen the same seeing, hence the anti-parallel subtraction should eliminate the seeing contribution in the cross-correlation profiles. However, real observations have shown that this statement was not verified. The seeing contribution is still present in the data, even after the anti-parallel subtraction. Indeed the statement relies on the hypothesis that the seeing profile is symmetric and invariant under $180°$ rotation. The causes for the asymmetry are various: the seeing profile is probably asymmetric from the start, and is affected by the instrumental effects. Due to the prism rotation, the two channels do not have the same instrumental profile. Consequently the subtraction does not remove completely the seeing in the cross-correlation profiles. Yet reducing the difference between the instrumental profile, by choosing for instance Dove prisms with smaller base angle tolerance, would improve the analysis of the seeing profile.

Furthermore, I showed that the seeing profile has two different contributions, one of important amplitude which varies on long timescales — one to two hours —, and one varying on short timescales, comparable to the seeing time scale, but of low amplitude. It is not excluded that the first contribution reflects the instrumental profile during the observations, since it seemed independent of the star's location. However, the spectrograph and DeSSpOt were both in closed rooms, which were temperature controlled. No changes in temperature were recorded during the observation time. Pressure variations should have been seriously dimmed by the room's enclosure. Hence, I would expect the fluctuations in the instrumental profile to vary on a longer time scale than observed.

The performances of DeSSpOt satisfied the expectations, taking into consideration that the instrument is still in a prototype phase. The analysis of the individual position spectrum for each channel has shown that the dispersion effects from the instrument were underestimated, in particular the horizontal dispersion. Yet using DeSSpOt has permitted to determine the position angle of Aldebaran and Capella by comparing the spatial seeing profile to the spatial stellar profile. Both targets were determined with an offset up to $10°$. Whether this value is a systemic error caused by the instrument or an imprecision in the measurement can be verified by observing further binary systems with known orbital position angles, for instance η Andromeda. Should the error be constant, then this method would determine position angles with a higher precision than Differential Speckle Interferometry.

Finally, since the seeing contribution could not be cancelled out with the anti-parallel subtraction, the analysis method relied mainly on the comparison between the seeing and the stellar cross-correlation profiles. This analysis strategy was not yet applied on the data of Aldebaran obtained with UVES to determine from a single channel the position angle. Nonetheless should it be proved successful in this one-channel case, it would not mean an end to DeSSpOt. Indeed the gain in observational time with DeSSpOt is tremendous compared to a single channel instrument, see Figure 6.1. Single channel requires that the star image has to be rotated as least seven times to probe eight images
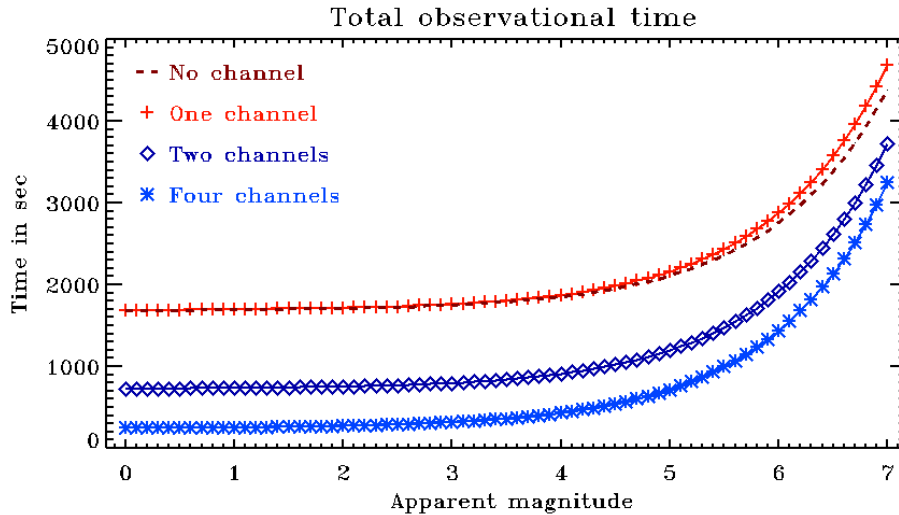
Figure 6.1: Evolution of the total observing time with the number of channels in DeSSpOt using a 1 m telescope. Each exposure per orientation should reach at least a Signal to Noise of 100. The overhead time is set at 4 min. The slight difference between the no-channel and the one-channel configurations are caused by the transmittance of the channel, taken here of 90%. Up to an apparent magnitude of 5, the two-channel DeSSpOt provides a reduction of the observation time by a factor 2.

for the anti-parallel subtraction — which is still necessary to remove instrumental artefacts. The time needed to proceed to this rotation is called overhead. On the UVES instrument, it takes four minutes to rotate the field of view by $60°$. By taking into account this value, as illustrated in Figure 6.1, the two-channel DeSSpOt provides a reduction of the total observational time of a factor 2 for stars up to magnitude 5 for the same level of signal to noise, under the assumption that the transmittance of a channel is around 90%. Moreover, it is advantageous to use DeSSpOt in the observation of stars up to magnitude 8. The residual time can then be used for other observations.

6.2 Conclusions

The results of the observations of Aldebaran with DeSSpOt and the TLS-Spectrograph show that it is possible to determine the position angle of single late type giants with a middle class telescope, an existing spectrograph and with moderate errors. Our measurement of $114.82° \pm 3.4°$ is in agreement with the value of $110° \pm 5°$ obtained from observations done with Differential Speckle Interferometry. Further observations of known binaries would finish to constrain and explain our error sources.

The observations also confirm the validity of the two-dimensional rotational model which takes into account the stellar spatial size. This allows now the simulation of two-dimensional synthetic spectra for any kind of rotational velocity. The addition of turbulence effects in the model would permit a better identification of the possible targets.

Furthermore, the observations show that the seeing contribution is made of two components, with different time scales and amplitudes. The origin of the long lasting component is uncertain, either seeing itself or instrumental effects. However, this effect would permit the observation of stars like Aldebaran whose lines are blended to the telluric lines, without information losses and with good precisions.

The test campaign with DeSSpOt proved that the instrument can be designed small, modular and remain functional once inserted on existing spectrograph without causing major troubles or resolution losses. It also permits to define the optimal realistic observing conditions to improve the signal detection: smaller seeing and smaller plate scale which are proposed as further improvement of the design.

6.3   Outlook

6.3.1   Design Improvements - Short Term Perspective

The current design of the instrument caused important light losses. In situations where already the exposure time has to be doubled due to the two channels, every additional loss is repercuted on the exposure time. Most of the light is currently lost in the Dove prism of the channel at 180°. This prism is hold by two plastic screws which rest on the reflecting surface. As a result, the light is partly transmitted to the screw and is lost for the spectrograph. In the new design, the prism is pressed laterally against the mount with a spring, removing the use of any screw.

Finally, the measures on the real data have shown that the instrumental profiles of the channels are not identical. This is only natural since the Dove prisms diffract the light in orthogonal direction, and this particularity would be reflected on the measured profiles. Hence, either one tries to minimise the diffraction effects of the prism, and in this case it would require prisms with much lower manufacturer tolerances. Or one tries to correct for the diffraction the same way as it is done for the atmosphere on some instruments: implementation of an Atmospheric Dispersion Corrector.

6.3.2   Adaptive Optic - Mid Term Perspective

Additional instrumentation would highly improve the capacity of the instrument. The detection of the spectro-astrometric signal is related to the stellar apparent diameter and also to the spectrograph's characteristics, in particular its field of view in the spatial direction. On the TLS-spectrograph, the field of view on the detector is of $0.5''$/pixel, which means that in order to detect the signal of Aldebaran (20mas diameter), a precision around 3 to 5% of a pixel is required. For any smaller star, the precision soon needs to be below 1% of a pixel.

To achieve such precisions, individual pixel properties such as the pixel response function have to be known. This can be determined in the laboratory using the Spot-o-Matic set up described by Barron et al. (2007). Each pixel is illuminated separately, response and sensitivity are recorded and analysed. However, determining the pixel response function on an already implemented detector is tremendously harder. Another idea would be to change the detector for one with smaller pixels. However, if the design of the spectrograph is not adapted along, the width of the orders increases also, causing a drop in the precision of the photocenter. Therefore, this is not an adapted solution.

Finally, I propose to reduce the size of the stellar PSF on the slit together with the change of detector, since the size of the star on the slit determines the width of the order. The implementation of a small adaptive optic unit before DeSSpOt was already suggested as part of this project but couldn't be achieved in this time range. However the advantages are numerous:

– Better field of view. With a working AO, the size of the stellar spot would be reduced to one or less arcseconds. If the spectrograph is adapted consequently, a field of view of less than $0.2''$/pixel could be achieved. The imaging capabilities in spatial direction would be increased to lower scales.

– Lower exposure times. Currently most of the light is lost at the slit. Indeed, the slit width is narrower than the star spot to achieve high resolution spectra. The AO concentrates the light back to one point in order to be close to the diffraction limit. Therefore, the light losses at the slit could be reduced, and consequently the exposure time decreased.

Even a simple tip-tilt solution would provide an amelioration of at least 30% in terms of light losses, and seeing disk size. This possiblity should not be excluded in the development process of an integral instrument comprising AO, DeSSpOt and high resolution spectrograph for observations on middle size telescopes.

Appendix A

Appendix

A.1 Study of the errors in the cross-correlation analysis

The Equation A.1, introduced in the Section 3.2.3, provides a way to include the errors in the measurements in the calculation of the cross-correlation function. The normalisation coefficient is balanced with the variances of the errors. The higher the variance, the lower the normalisation coefficient.

$$C_{XY} = \frac{c_{xy}}{\sqrt{(\sigma_x{}^2 - \sigma_{\delta x}^2) \times (\sigma_y - \sigma_{\delta y}^2)^2}} \tag{A.1}$$

As a result the cross-correlation function is magnified, when the measured errors are highly dispersed. When we include the simulated errors of the position spectrum in the determination of the cross-correlation function, a high signal is observed even for slit angle where it should be absent. Consequently the fit of the sine curve along the maxima is compromised. Indeed the maxima no longer follow a sine shape but a smoothed boxcar function. The extracted stellar position angle is in this case largely overestimated by over $12°$, see Figure A.1. Hence, the cross-correlation functions are calculated without the implementation of the measured errors. These can still be incorporated in the final analysis as weights for the data maxima.
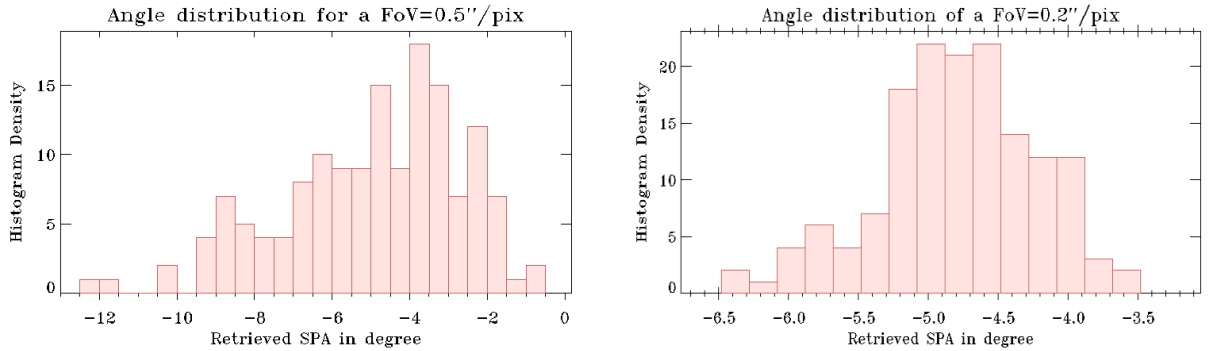
(a) Angle distribution for position spectra for a simulated field of view of $0.5''$/pix.The distribution presents a general offset of approximatively $4.9°$.

(b) Angle distribution for a simulated field of view of $0.2''$/pix. The offset is in the same order of magnitude.

Figure A.2: Angle distribution for fields of view of $0.5''$/pix and $0.2''$/pix. The errors of the position spectrum were not included in the determination of the cross-correlation functions.

I verified if the absence of measured errors in the CCF improves the extracted position angle. The simulation was run again a hundred times. Once for a field of view of $0.2''$/pix, which should represent a high quality data set, and once for a field of view of $0.5''$/pix, representing a degraded data set. The errors in the maxima are calculated from the cross-correlation error formula. The retrieved
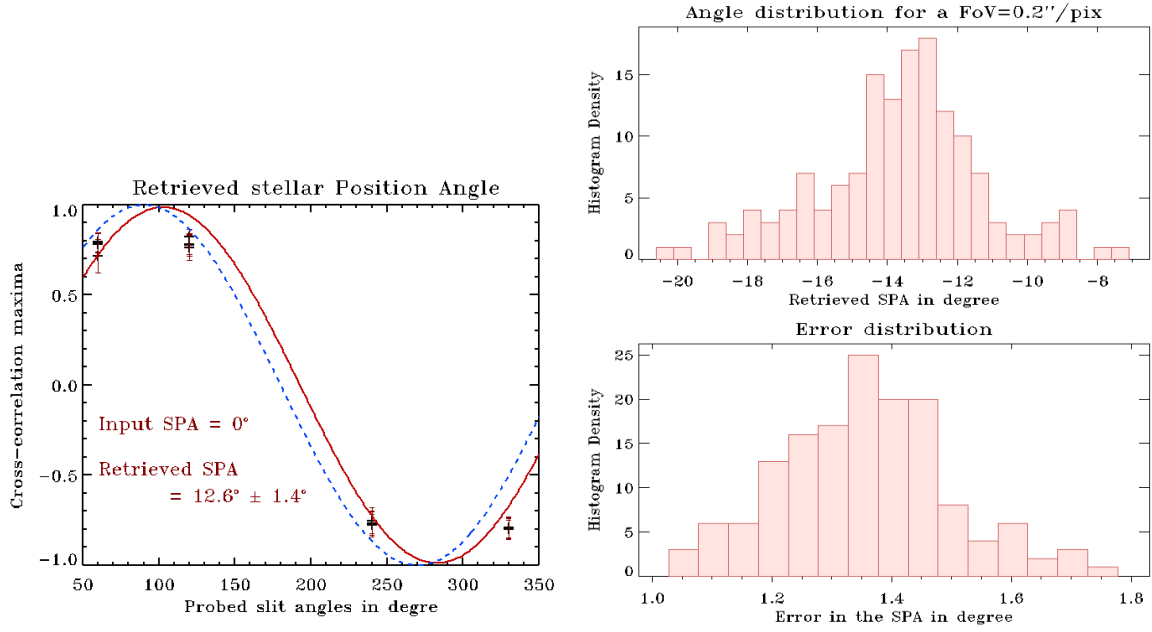
(a) Retrieved position angle with a cross-correlation function including the measured errors. The retrieved angle lies 12° appart from the input value.

(b) Distribution of the retrieved position angle and the errors

Figure A.1: Simulation results obtained with the error inclusion in the calculation of the CCF.The distribution of the retrieved angle over 100 run shows a clear offset of the position angle.

position angle is extracted from the phase of $\sin(\psi + \mathrm{PA})$. Due to the definition of the sine curve, the extracted PA is the negative of the true value. For instance, for an input PA of $40°$, the extracted PA would be $-40°$. Nevertheless, I noticed an recurrent offset of $4.80° \pm 0.5°$ in the extracted position angle independent of the data quality, as illustrated in Figure A.2. This implies that the extraction method tend to overestimate the absolution stellar position angle.

A.2 Description of the pixellation correction program

The pixellation effects are particularly visible when normalising the position spectrum with the trace as seen left on the Figure A.3. This step, which consist to set to set the median of the position spectrum at zero, is necessary for the identification of the spatial feature. As seen on the Figure A.3, the pixellation effect completely prevent any kind of analysis on the position spectrum. A direct correction on the position spectrum is not possible without affecting the signal. Hence I devised a method which reproduce the pixellation effect as accurately as possible in the trace.
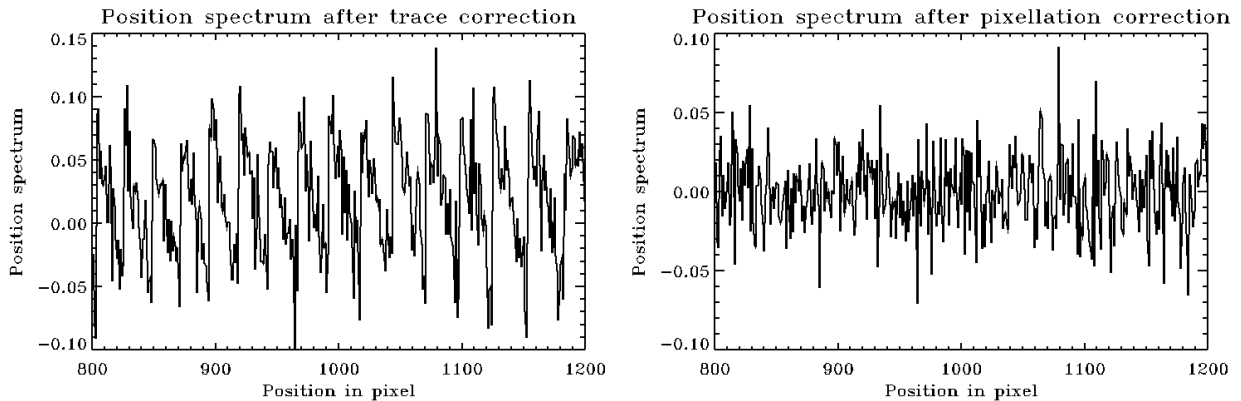
Figure A.3: Elimination of pixellation effects. *Left*: The position spectrum after a simple trace correction. The steps identified in the position spectrum are repeated here like some zigzags. Their amplitude is far higher than that of the signal. *Right*: The position spectrum after the pixellation correction. The zigzag effect is no longer visible, and the whole amplitude of the position spectrum is reduced.

The program is based on a simplex algorythm. The real position spectrum and the trace are given in input. The program then performs the following steps:

– A cross-dispersion profile is generated. This profile is based on the shape of the real data. Here, half of the profile is described by a gaussian, and the other half by a Lorenzian function. This profile is described by the function:

$$
y_{prof}(i) = \begin{cases} exp\left(-\dfrac{(i-x_o)^2}{2\,P_3^2}\right) & \text{for } i \leq x_o \\[4mm] \dfrac{P_0\,exp\left(-\dfrac{(i-x_o)^2}{2\,P_3^2}\right) + P_1\mathfrak{L}(i,x_o,P_4)}{P_0 + P_1} & \text{for } i > x_o \end{cases} \tag{A.2}
$$

where $\mathfrak{L}$ is the Lorentz function, centered in x_o, with a width P_4. The P_j are the only free parameters used in the constitution of the cross-dispersion profile. They determine the shape of the pixellation effect.

– The profile is expanded in dispersion direction. Along the dispersion, no features are added, this represents a perfect continuum.

– The simulated order is now shifted following the trace, to reproduce exactly the order as seen on the detector. The small shifts are performed using a Fourier shifting method.

– Finally the position spectrum is extracted. The program has generates an spectrum with pixellation effects. It is compared to the real spectrum. The parameters which lower the difference are kept.

– Using a simplex loop based on the AMOEBA.PRO procedure from IDL, this procedure is repeated until the difference between both spectra is lower than the convergence limit.

The program itself is writen in IDL, and is to be found under the name SIMBARY.PRO in the dedicated SPASTRO package for spectro-astrometric reduction programs.

Nomenclature

AO	Adaptive Optic
CCF	Cross-Correlation Function
ΔCCF	Differential Cross-Correlation Function from $\text{CCF}_{0°} - \text{CCF}_{180°}$
DeSSpOt	Differnetial imagE rotator for Stellar Spin OrienTation
IDL	Interactive Data Language
IR	Infra Red
IRAF	Image Reduction and Analysis Facility
PA	Position Angle
OLT	Oskar Lühing Telescope
SPA	Stellar Position Angle
TLS-Spectrograph	Thüringer Landessternwarte Spectrograph
UVES	Ultraviolet and Visual Echelle Spectrograph
VLT	Very Large Telescope

List of Figures

List of Tables

Bibliography

Albrecht, S., Reffert, S., Snellen, I. A. G. & Winn, J. N. (2009), 'Misaligned spin and orbital axes cause the anomalous precession of DIHerculis', *Nature* **461**, 373–376.

Ammler-von Eiff, M. & Reiners, A. (2012), 'New measurements of rotation and differential rotation in A-F stars: are there two populations of differentially rotating stars?', *AAP* **542**, A116.

Bailey, J. (1998*a*), 'Detection of pre-main sequence binaries using spectro-astrometry', *MNRAS* **301**, 161–167.

Bailey, J. (1998*b*), Spectroastrometry: a new approach to astronomy on small spatial scales, Vol. 3355 of *Society of Photo-Optical Instrumentation Engineers (SPIE) Conference Series*, pp. 932–939.

Barron, N., Borysow, M., Beyerlein, K., Brown, M., Lorenzon, W., Schubnell, M., Tarlé, G., Tomasch, A. & Weaverdyck, C. (2007), 'Subpixel Response Measurement of Near-Infrared Detectors', *PASP* **119**, 466–475.

Bate, M. R., Lodato, G. & Pringle, J. E. (2010), 'Chaotic star formation and the alignment of stellar rotation with disc and planetary orbital axes', *MNRAS* **401**, 1505–1513.

Beckers, J. M. (1982), 'Differential speckle interferometry.', *Optica Acta* **29**, 361–362.

Che, X., Monnier, J. D., Zhao, M., Pedretti, E., Thureau, N., Mérand, A., ten Brummelaar, T., McAlister, H., Ridgway, S. T., Turner, N., Sturmann, J. & Sturmann, L. (2011), 'Colder and Hotter: Interferometric Imaging of β Cassiopeiae and α Leonis', *ApJ* **732**, 68.

Ciddor, P. E. (1996), 'Refractive index of air: new equations for the visible and near infrared', *Applied Optics* **35**, 1566–1573.

Condon, J. J. (1997), 'Errors in Elliptical Gaussian FITS', *pasp* **109**, 166–172.

Denisov, N. A. & Koroleva, T. V. (1997), Design of mirror image rotator systems, Vol. 3055 of *Society of Photo-Optical Instrumentation Engineers (SPIE) Conference Series*, pp. 297–300.

Domiciano de Souza, A., Kervella, P., Jankov, S., Abe, L., Vakili, F., di Folco, E. & Paresce, F. (2003), 'The spinning-top Be star Achernar from VLTI-VINCI', *A&A* **407**, L47–L50.

Edelson, R. A. & Krolik, J. H. (1988), The discrete correlation function: A new method for analyzing unevenly sampled variability data, *in* 'ESA Special Publication', Vol. 281 of *ESA Special Publication*, pp. 387–390.

Endal, A. S., Massa, D. & Altner, B. (1989), Cross-Spectral Dispersion Imaging Techniques for Resolving Red + Blue Binaries: First Results, Vol. 21 of *Bulletin of the American Astronomical Society*, p. 1082.

Glebocki, R. & Gnacinski, P. (2005), 'Catalog of Stellar Rotational Velocities (Glebocki+ 2005)', *VizieR Online Data Catalog* **3244**, 0.

Gray, D. F. (2008), *The Observation and Analysis of Stellar Photospheres*, Cambridge University Press, Third edition.

Hauschildt, P. & Baron, E. (2005), 'Cool stellar atmospheres with PHOENIX .', *Memorie della Societa Astronomica Italiana Supplementi* **7**, 140.

Lafrasse, S., Mella, G., Bonneau, D., Duvert, G., Delfosse, X. & Chelli, A. (2010), 'JMMC Stellar Diameters Catalogue - JSDC (Lafrasse+, 2010)', *VizieR Online Data Catalog* **2300**, 0.

Lagarde, S., Sanchez, L. J. & Petrov, R. G. (1995), Sub-resolution Limit Spatio-Spectral Information Using Differential Speckle Interferometry, *in* G. Comte & M. Marcelin, ed., 'IAU Colloq. 149: Tridimensional Optical Spectroscopic Methods in Astrophysics', Vol. 71 of *Astronomical Society of the Pacific Conference Series*, p. 360.

Mahajan, V. (1991), *Aberration theory made simple*, SPIE optical engineering press.

Markwardt, C. B. (2009), Non-linear Least-squares Fitting in IDL with MPFIT, *in* D. A. Bohlender, D. Durand & P. Dowler, eds, 'Astronomical Data Analysis Software and Systems XVIII', Vol. 411 of *Astronomical Society of the Pacific Conference Series*, p. 251.

Marsh, T. R. (1989), 'The extraction of highly distorted spectra', *Astronomical Society of the Pacific* **101**, 1032–1037.

Massarotti, A., Latham, D. W., Stefanik, R. P. & Fogel, J. (2008), 'Rotational and Radial Velocities for a Sample of 761 HIPPARCOS Giants and the Role of Binarity', *Astrophysical Journal* **135**, 209–231.

McAlister, H. A., ten Brummelaar, T. A., Gies, D. R., Huang, W., Bagnuolo, Jr., W. G., Shure, M. A., Sturmann, J., Sturmann, L., Turner, N. H., Taylor, S. F., Berger, D. H., Baines, E. K., Grundstrom, E., Ogden, C., Ridgway, S. T. & van Belle, G. (2005), 'First Results from the CHARA Array. I. An Interferometric and Spectroscopic Study of the Fast Rotator α Leonis (Regulus)', *ApJ* **628**, 439–452.

Monnier, J. D. & Allen, R. J. (2012), 'Radio & optical Interferometry: Basics observing techniques and data analysis', *ArXiv e-prints*.

Monnier, J. D., Zhao, M., Pedretti, E., Thureau, N., Ireland, M., Muirhead, P., Berger, J.-P., Millan-Gabet, R., Van Belle, G., ten Brummelaar, T., McAlister, H., Ridgway, S., Turner, N., Sturmann, L., Sturmann, J. & Berger, D. (2007), 'Imaging the Surface of Altair', *Science* **317**, 342–.

Moreno, I., Paez, G. & Strojnik, M. (2003), 'Dove prism with increased throughput for implementation in a rotational-shearing interferometer', *Applied Optics* **42**, 4514–4521.

Peterson, D. M., Hummel, C. A., Pauls, T. A., Armstrong, J. T., Benson, J. A., Gilbreath, G. C., Hindsley, R. B., Hutter, D. J., Johnston, K. J., Mozurkewich, D. & Schmitt, H. (2006*a*), 'Resolving the Effects of Rotation in Altair with Long-Baseline Interferometry', *ApJ* **636**, 1087–1097.

Peterson, D. M., Hummel, C. A., Pauls, T. A., Armstrong, J. T., Benson, J. A., Gilbreath, G. C., Hindsley, R. B., Hutter, D. J., Johnston, K. J., Mozurkewich, D. & Schmitt, H. R. (2006*b*), 'Vega is a rapidly rotating star', *Nature* **440**, 896–899.

Pfeiffer, M. J., Frank, C., Baumueller, D., Fuhrmann, K. & Gehren, T. (1998), 'FOCES - a fibre optics Cassegrain Echelle spectrograph', *Astron. Astrophys. Suppl. Ser.* **130**, 381–393.

Roe, H. G. (2002), 'Implications of Atmospheric Differential Refraction for Adaptive Optics Observations', *Astronomical Society of the Pacific* **114**, 450–461.

Sar-El, H. Z. (1991), 'Revised Dove prism formulas', *Applied Optics* **30**, 375–376.

Torres, G., Claret, A. & Young, P. A. (2009), 'Binary Orbit, Physical Properties, and Evolutionary State of Capella (α Aurigae)', *apj* **700**, 1349–1381.

van Belle, G. T., Ciardi, D. R., ten Brummelaar, T., McAlister, H. A., Ridgway, S. T., Berger, D. H., Goldfinger, P. J., Sturmann, J., Sturmann, L., Turner, N., Boden, A. F., Thompson, R. R. & Coyne, J. (2006), 'First Results from the CHARA Array. III. Oblateness, Rotational Velocity, and Gravity Darkening of Alderamin', *ApJ* **637**, 494–505.

van Belle, G. T., Ciardi, D. R., Thompson, R. R., Akeson, R. L. & Lada, E. A. (2001), 'Altair's Oblateness and Rotation Velocity from Long-Baseline Interferometry', *ApJ* **559**, 1155–1164.

Voigt, B. & Wiedemann, G. (2009), Surface spots on cool giants probed by spectro-astrometry, *in* E. Stempels, ed., '15th Cambridge Workshop on Cool Stars, Stellar Systems, and the Sun', Vol. 1094 of *American Institute of Physics Conference Series*, pp. 896–899.

Weber, M. (2007), 'Differential rotation of giant stars', *Astronomische Nachrichten* **328**, 1075.

Weber, M. & Strassmeier, K. G. (2011), 'The spectroscopic orbit of Capella revisited', *A & A* **531**, A89.

Wheelwright, H. E., Oudmaijer, R. D. & Goodwin, S. P. (2010), 'The mass ratio and formation mechanisms of Herbig Ae/Be star binary systems', *MNRAS* **401**, 1199–1218.

Whelan, E. & Garcia, P. (2008), Spectro-astrometry: The Method, its Limitations, and Applications, *in* F. Bacciotti, L. Testi, & E. Whelan, ed., 'Jets from Young Stars II', Vol. 742 of *Lecture Notes in Physics, Berlin Springer Verlag*, p. 123.

Wiedemann, G. (2013), 'In preparation'.

Zhao, M., Monnier, J. D., Pedretti, E., Thureau, N., Mérand, A., ten Brummelaar, T., McAlister, H., Ridgway, S. T., Turner, N., Sturmann, J., Sturmann, L., Goldfinger, P. J. & Farrington, C. (2009), 'Imaging and Modeling Rapidly Rotating Stars: α Cephei and α Ophiuchi', *ApJ* **701**, 209–224.

Zucker, S. (2003), 'Cross-correlation and maximum-likelihood analysis: a new approach to combining cross-correlation functions', *MNRAS* **342**, 1291–1298.

Acknowledgements

When asked what I do for a living, the dialogue often follow this pattern:
– I do a PhD in Astronomy.
– And? Have you discovered a new star?
Too bad it's not longer that simple. Yet I'm proud that I could contribute a little to the expansion of knowledge, by putting a small candle in the up-to-now dark field of stellar spin orientation.

Therefore, I'm very thankful to Günter Wiedemann for giving me the opportunity to do this thesis. I appreciated his availability and patience for most questions. He suffered through chalk-throwing sessions. And at the end, even played cat and mouse when I was writing. Nonetheless I had a lot of fun during these three years, and I'm thankful for that too.

I also would like to thank the people of the Thüringer Landessternwarte for their help in installing DeSSpOt on their telescope. Eike who, with his everlasting pessimism ("If you are very lucky you may be able to see one star through your instrument at the end of the week") motivated me to prove him wrong!! I observed more than one star, and already in the second night, with his help in the Coudé room, the instrument was adjusted. Holger, Johannes and Tom also deserve a biiiig "Thanks", because I would never have been able to install DeSSpOt on the spectrograph without their help. Finally, I'm also grateful to Artie Hatzes who let me use his precious telescope for my tests.

Back to Hamburg, I would have a hard time in the lab if Magnus had not provided me with valuable advices and cookies.

I would not have been able to write a nice thesis without the help of Stefan, who did a lot of proof reading in English and German and so much more (how was the praktikum again?).

I do not forget my friends at the observatory: Carolina CaroooooolaaaaaAaaaaa who also went through the hardship of proof reading, Lalitha, and Matthias, and all the boys of our group. And the friends back in France, Astrid, Marc (who proof-read the French abstract version), Audrey, all three now Docteur... Wait for me, I'm joining the club sooooooon!!!

At last, my family, mum, dad and grand-mother were all there during these three years to encourage me. And of course, Antoine, mon bonhom, who had to support me for all this time.
– So how was your day?
– I don't know, I have a problem with the detected angle for Capella. The cross-correlation function are somehow offset. I don't know why but it's bothersome. I've tried a lot and...
– uhuuuuu.... If you say so.